Alma Mater Studiorum – Università di Bologna

DOTTORATO DI RICERCA IN

Meccanica e Scienze Avanzate dell'Ingegneria

Ciclo XXXII

Settore Concorsuale: 09/C1

Settore Scientifico Disciplinare: ING-IND/08

TITOLO TESI

Development and Validation of a Model-Based Combustion Controller for Water Injection Management

Presentata da: Francesco Ranuzzi

Coordinatore Dottorato **Supervisore**

Prof. Ing. Marco Carricato **Prof.Ing. Nicolò Cavina**

Esame finale anno 2020

Abstract

This manuscript reports the overall development of a Ph.D. research project which lasted 3 years, during the “Mechanics and advanced engineering sciences” course at the Department of Industrial Engineering of the University of Bologna. The project, with title of “Development and Validation of a Model-Based Combustion Controller for Water Injection Management”, is focused on the development of a combustion control system for an innovative Spark Ignited engine layout. In details, the controller is oriented to manage a prototypal engine equipped with a Port Water Injection system. The water injection technology allows an increment of combustion efficiency due to the knock mitigation effect that permits to keep the combustion phasing closer to the optimal position with respect to the traditional layout.

At the beginning of the project, the effects and the possible benefits achievable by water injection have been investigated by a focused experimental campaign. Then the data obtained by combustion analysis have been processed to design a control-oriented combustion model. The model identifies the correlation between Spark Advance, combustion phasing and injected water mass, and two different strategies are presented, both based on an analytic and semi-empirical approach and therefore compatible with a real-time application.

The model has been implemented in a combustion controller that manages water injection to reach the best achievable combustion efficiency while keeping knock levels under a pre-established threshold. Three different versions of the algorithm are described in detail. This controller has been designed and pre-calibrated in a software-in-the-loop environment and later an experimental validation has been performed with a rapid control prototyping approach to highlight the performance of the system on real set-up. To further make the strategy implementable on an onboard application, an estimation algorithm of combustion phasing, necessary for the controller, has been developed during the last phase of the PhD Course, based on accelerometric signals.

Index

Introduction

In recent years, the main research for automotive companies has been represented by the improvement of vehicle efficiency since all emission regulation plans are becoming more demanding in terms of reduction of CO_2. The efficiency of spark ignited engines can be relevantly increased adopting different technologies. The first solution adopted consists in the combination of turbocharging and downsizing. This strategy is limited by the phenomenon of knock due to higher pressure inside the chamber. Therefore, the combustion control system is forced to delay the combustion phasing to a less efficient position in case of high load. The delayed combustion presents a higher exhaust gas temperature causing thermal stress to the turbine and so a rich value of air-fuel ratio can be required to use the excess of fuel to cool the exhaust temperature. These necessary solutions affect the final efficiency of the engine, vanishing part of the benefit achievable by the turbocharging-downsizing layout. The introduction of inert chemical compounds such as water or recirculated exhaust gas used to dilute the combustion and as heat sink can be a relevant and feasible solution to this problem. These new technologies require a dedicated combustion control system able to manage the effect on the combustion dynamics. To face the complexity of the system an innovative approach to design the controller is required. In this work, a prototypal Gasoline Direct Injection engine has been equipped with a Port Water Injection system, for the study and the development of a Model-based Water Injection Combustion Control System.

A complete introduction of water injection concept is provided in Chapter 1 explaining the state of art of this technology. In Chapter 2, the experimental setups are described. In detail, information about the Port Water Injection system together with the related Rapid Control Prototyping system. The first experimental investigation campaign on the system is explained in Chapter 3 with a focus on the effect of injected water on combustion dynamics.

The core of this work is represented by the development of the controller. The first step is the definition of a combustion model able to estimate the Spark Advance angle required to obtain a target combustion phase taking in account the effect of the injected water mass, as shown in Chapter 4. Two different approaches are presented, and both rely on an analytical and semi-empirical approach. Due to the computational simplicity of the approach, the model can be involved in real time application such as combustion control system. Therefore, the model has been implemented in an open loop controller which adopts two target maps, one of water-fuel ratio and one of target combustion phase angle as inputs. During the following step of development, the controller has been improved adding a closed loop based on knock index that allows also the use of water injection for knock control. In the last step, also another branch of closed loop based on combustion phase index has been integrated in the system to compensate

the inevitable error that can affect the model. These two steps employ a calibrated strategy to manage correction to be applied both to water to inject and to spark advance to be applied, and the required combustion indexes are provided by indicating system. The complete description of the controller is presented in Chapter 5 and its performance evaluated in software-in-the-loop environment is shown in Chapter 6. To show the effectiveness of the system on a real setup employing a real time hardware several validation tests are reported in Chapter 7.

To demonstrate the feasibility to employ the controller in an on-board application the combustion indexes used as inputs and obtained by indicating system must be substituted with standard sensors. The knock index is already provided by the use of an accelerometer, and an estimation algorithm of combustion phase relying on the same sensor has been studied and calibrated and the main findings are presented in Chapter 8.

The internal combustion engine represents only a part of the efficiency of the powertrain. In fact, a further solution consists in the hybridization for SI engine, coupling the thermal engine with an electric motor and involving a battery as energy storage. The benefit of a hybrid system relies on the combination of the high efficiency of the electric motor available for a wide range of load and speed together with the advantage of long autonomy of the internal combustion engine. As the regulation plans on CO_2 become more tighter, the coupling of different kind of solution are more interesting for fuel saving on vehicle. A combustion controller able to manage the engine efficiency (through the combustion phasing) could be very important as a part of energy management system of a hybrid system. For this reason, during the last part of the Course, the modelling and control focus was enlarged to the whole powertrain, and developing possible strategies to optimize the overall energy efficiency for an electrified hybrid layout, as reported in Chapter 9.

1 State of art of Water Injection

The design of Spark Ignited engines is dealing with the challenge represented by the next stage of emission standards. Due to the combustion in presence of a homogenous mixture of air and fuel, these engines can reach better standard of emission in terms of low production of HC, CO, NOx and soot in comparison with diesel engine, but are affected by worse performance in terms of efficiency. Therefore, to fulfil the new standards that will require reduction of CO_2, new technologies, as described in [1] and displayed in Figure 1.1, are becoming more relevant in the SI engine field. The main strategy pursued to enhance efficiency in gasoline engine is the downsizing in combination with supercharging, in fact these two concepts applied together allow to reduce the use of the throttle in torque regulation only for the lower load. In this way, the reduction in overall efficiency caused by mechanical losses and throttle pressure drop is limited but the downsized engine is still able to provide all torque range of interest due to the turbocharger.

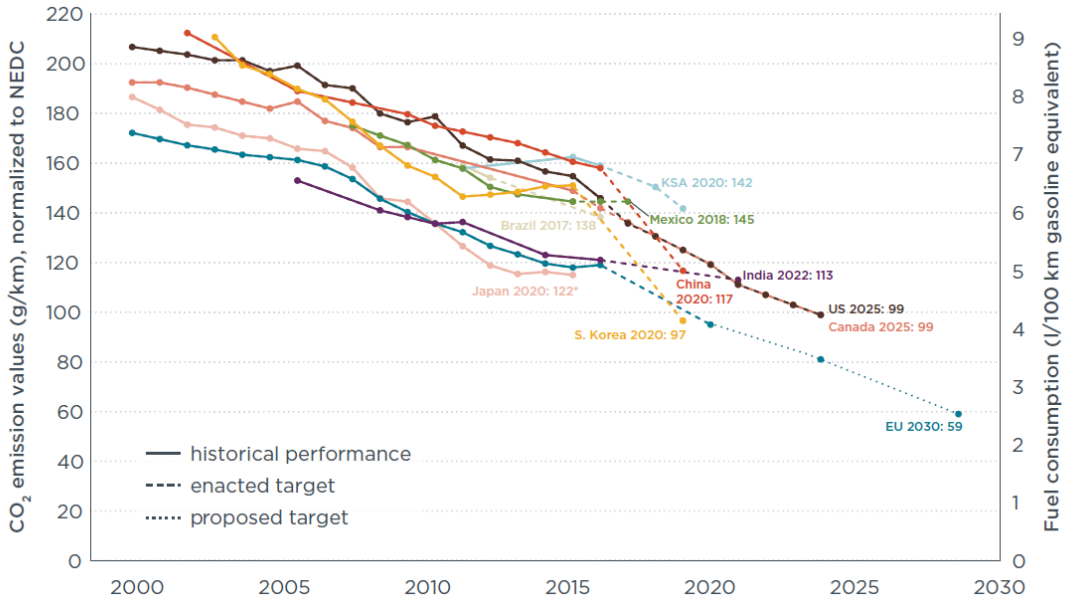

Figure 1.1 Comparison of global CO_2 regulations for new passengers cars.

One of the main limits of this technology is represented by the knock tendency of SI engines at high load. This specific feature of this engine type restricts the potential of supercharging. In fact, the probability of knock events increases as the in-cylinder pressure rises so that a delaying of Spark Advance angle is usually applied at high load. In this way, the overall efficiency is penalized in the upper area of the operative field. Furthermore, as a consequence, an excessive temperature at Turbine Inlet (TIT) or at catalytic converter may arise, which leads to an enrichment in the air/fuel mixture, and to a further penalization of the fuel consumption. In this case, technical solutions capable to reduce the knock tendency have to be adopted. Since downsizing and turbocharging remains a key strategy for the future, to overcome these aspects, the

traditional design of SI engines must evolve toward a new generation that can involve different kind of solutions to reduce the knock tendency. The most efficient ones are the water injection, external cooled EGR, VCR and Miller or Atkinson cycles as reported in [2]. The effects of the VCR, Miller and Atkinson cycles techniques on the SI engine performance have been thoroughly examined as emerged from literature, where various experimental and numerical studies are available [3,4,5,6,7].

The adoption of external cooled Exhaust Gas Recirculation (EGR), depending on the load level, allows decreasing the pumping losses, the knock tendency and the mixture enrichment [8]. The external cooled EGR at high load improves the fuel consumption ranging from 6% at high speed, up to 17% at low speed. The EGR allows for the knock mitigation according to the in-cylinder pressure-temperature state, which in turn varies with the Brake Mean Effective Pressure (BMEP). In particular, as demonstrated in [9], the EGR application to modern downsized turbocharged SI engines becomes less effective. The knock tendency reduction by the EGR is indeed expected to be more efficient for naturally aspirated engines, operated at a lower BMEP. As reported in [2] a further solution for knock suppression is the liquid water injection either within the cylinder or at the intake port [10 11 12 13 14]. Hoppe et al. [10] tested a single cylinder research engine, provided with Direct Water Injection (DWI), revealing notable efficiency improvements, around 16%, at low speed and high load.

The application of water injection in combustion engines is as old as the combustion engine itself. Prof. Hopkinson from the University of Cambridge proposed the water injection as an internal coolant of gas engines already in 1913 [15]. He emphasized the cooling effect by water due to higher heat of vaporization and increased heat capacity. Harrington [6] investigated the effect of liquid or vaporized water on the performance and engine out emissions. He performed measurements on a single-cylinder engine with water injection into the intake manifold. He found a stronger effect of liquid water compared to vaporized water. Due to the water addition the physical ignition delay increased, the combustion duration was prolonged, and the knocking tendency was reduced.

Different strategies for water injection into combustion engines are available [17, 19, 20]. For example, manifold and port water injection (PWI), emulsion direct injection and separate direct water injection (DWI). The strategies differ by increasing complexity of the injection system and decreasing water consumption. Since the manifold and port injection systems use lower injection pressures and longer injection durations, the water pump can be smaller and the injection controls are simplified. The injected water vaporizes during the gas exchange, as consequence the intake charge is cooled, and the gas density is increased [18, 19]. However, if too much liquid water is injected, it can impinge on the walls and water can slip through the exhaust ports during valve overlap, leading to increased water consumption. The emulsion direct injection

requires only one injector to inject the water/fuel emulsion into the cylinder [18]. The separate direct injection of water requires two injectors, which are mounted into the cylinder head. This method is constrained by the limited cylinder head space available in modern SI engines. The injection system consists of a high-pressure water pump and rail system to deliver an injection pressure up to 200 bar. This enables more sophisticated injection strategies and water-efficient operation. Since the high-pressure water injector is exposed to high thermal loads, it is necessary to inject a minimum amount of water to cool down the injector and reduce attrition [17]. Due to the complexity of design related to a DWI and for an emulsion direct injection, in this work an experimental setup equipped with a Port Water Injection system has been investigated.

2 Experimental Set-up.

In this chapter an overview of the experimental setups involved in the activity is presented considering also the Rapid Control Prototyping system designed to employ the algorithm developed along the project. Further details are described in [21, 24].

2.1 Experimental Set-up TSI

2.1.1 GDI Supercharged Engine

The activity has been performed on a 4-cylinder Gasoline Direct Injection turbocharged engine, in order to reproduce the most relevant condition for the WI technology. In details, the chosen engine is a VW 1.4 TSI (Turbo Stratified Injection) and its main features are summarized in Table 1. Valve timing was kept constant during all carried out tests.

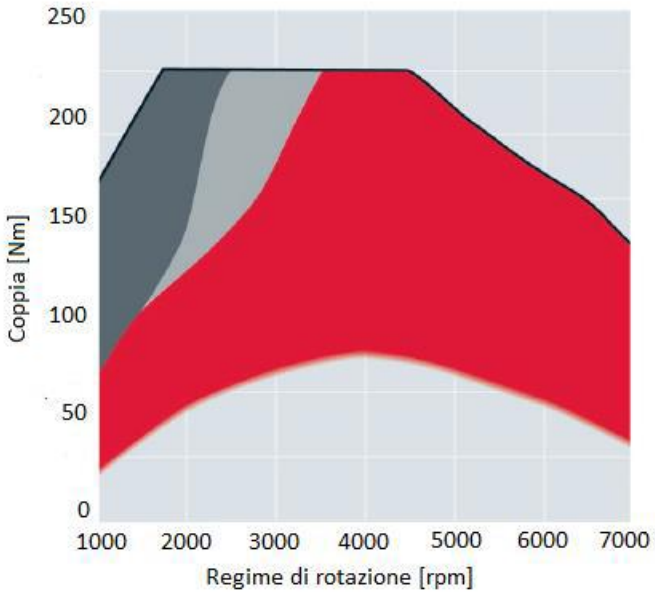

Figure 2.1 Operative field of VW 1.4 TSI. the red area represents the turbocharger operating zone

Table 2-1.1

Displaced volume	1389.9 cc (4 cylinder)
Stroke	75.6 mm
Bore	76.5 mm
Connecting Rod	144 mm
Compression ratio	10:1
Number of Valves	4
Exhaust Valve Open	580° BTDC @0.1 mm lift
Exhaust Valve Close	356° BTDC @0.1 mm lift

Inlet Valve Open	358° BTDC @0.1 mm lift
Inlet Valve Close	132° BTDC @0.1 mm lift

2.1.2 PWI System

To perform this research the engine has been modified in all intake air path to add a Port Water Injection (PWI) system. This PWI consists of an assembly of the following parts (Figure 1.2):

- Modified air intake manifold
- Injectors mounting block
- 4 water injectors
- Water Pressure Rail

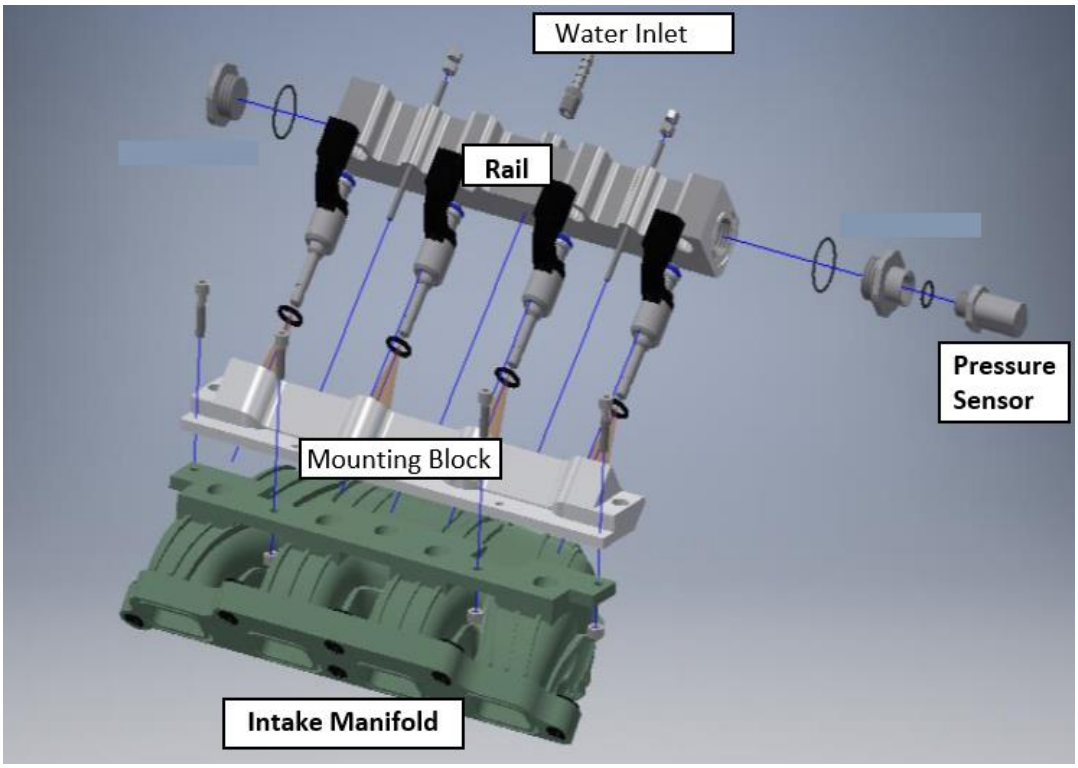

Figure 2.2 Port Water Injection system

The intake manifold has been designed to reproduce the same inner geometry of the original part with the aim to not change the features of fluid dynamic of the intake phase. The external geometry has been modified to provide a surface matching with the mounting block and a hole for each injector, and multiple ribs have been added to reinforce the structure. At the same time the geometry involved in matching with the other parts has been identically reproduced. This new manifold has then been produced with 3D printing in the University of Bologna labs using ABS Plus plastic.

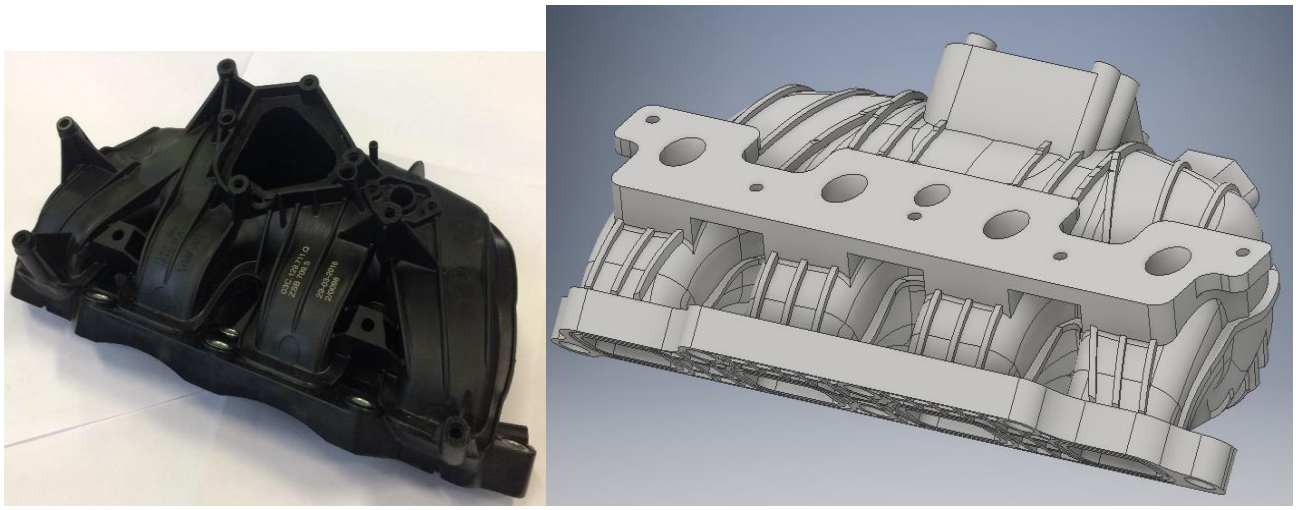

Figure 2.3 On left: original manifold. On right: the new WI manifold

The injectors are provided by Marelli Europe S.p.A. and they have been originally designed for urea injection in SCR technology. However, they have been chosen because of their compatibility with water.

The mounting block has been designed to be coupled with the intake manifold and to the give the injectors the proper direction. In fact, the axis of the injection cone must be aligned with the axis of the relative intake runner in order to enhance the chance of the water droplets to reach the cylinder without impacting the walls of the runner. The injectors control system is discussed in the next chapter.

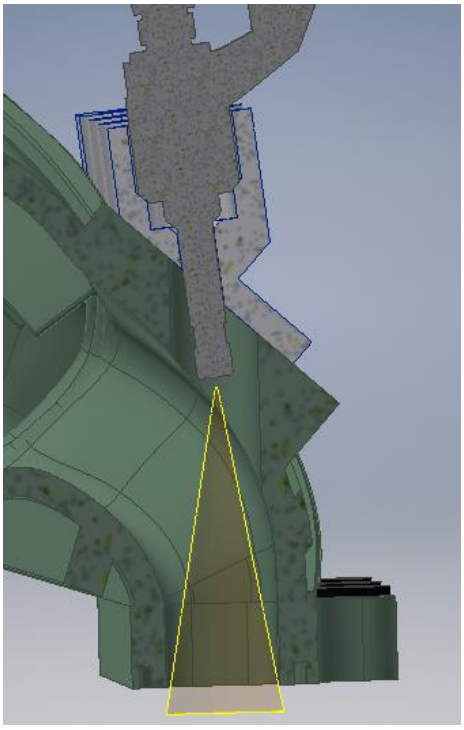

Figure 2.4. PWI system side view

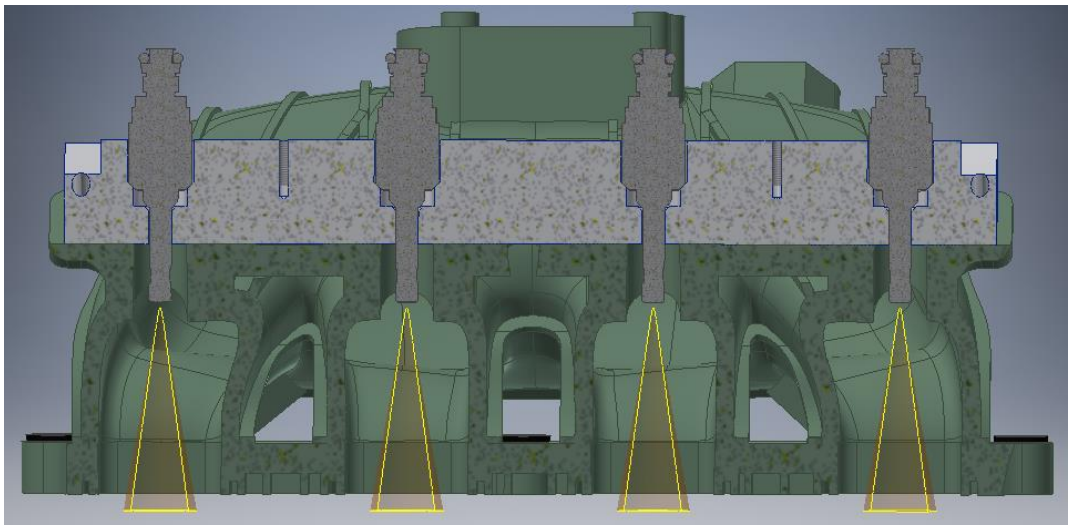

Figure 2.5 PWI system, inner view. In yellow the injection cone

The pressure water rail has been designed to split the pressurized water flow that is provided by the feeding line.

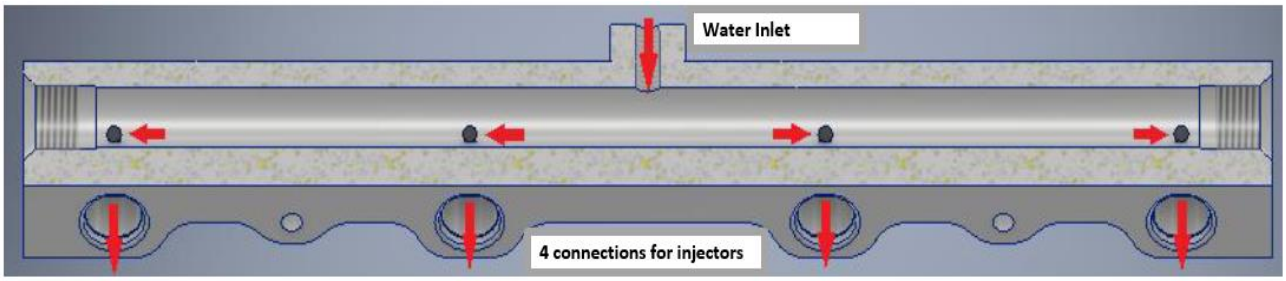

Figure 2.6 Water pressure rail, inner view

Both mounting block and rail are made in aluminium. As displayed in Figure 2.2, these two parts are linked together by 2 tie-rods. In this way, the injectors are pressed between these 2 parts obtaining the proper sealing of the system. To accomplish this goal both parts must precisely match the geometry of the injectors.

The water feeding line, in downstream way, consists in a filter and 2 pumps in series. The first pump works in fixed operative point and it is regulated by a manual pressure regulator. The second pump is driven by a dedicated control unit. There is also a feedback line that can close a loop in case of excessive pressure.

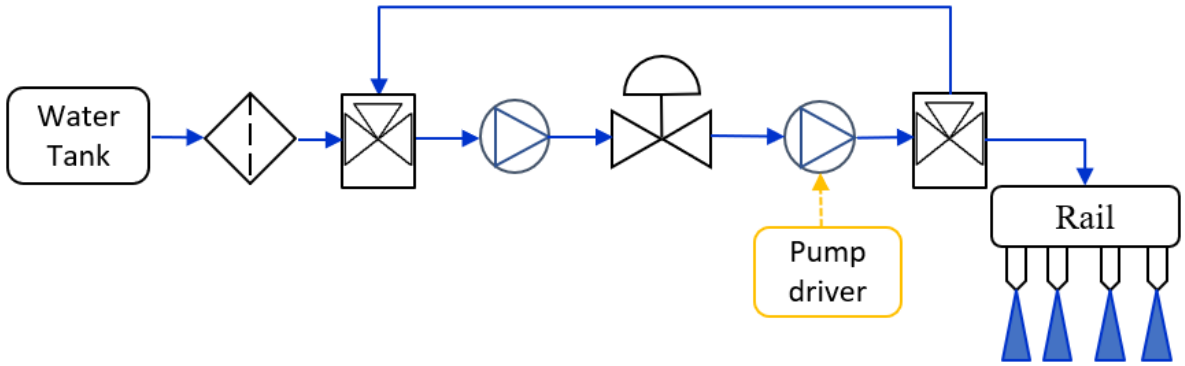

Figure 2.2 Water feeding line

To integrate the PWI system some modifications on the original lay-out have been necessary. All the intake air path has been changed with a more flexible line to create the space to insert the system. In Figure 2.3 there is the original TSI lay-out and all the eliminated parts have been signed with the red crosses. In Figure 2.4 it is displayed the present modified setup in which it is clearly visible the PWI system.

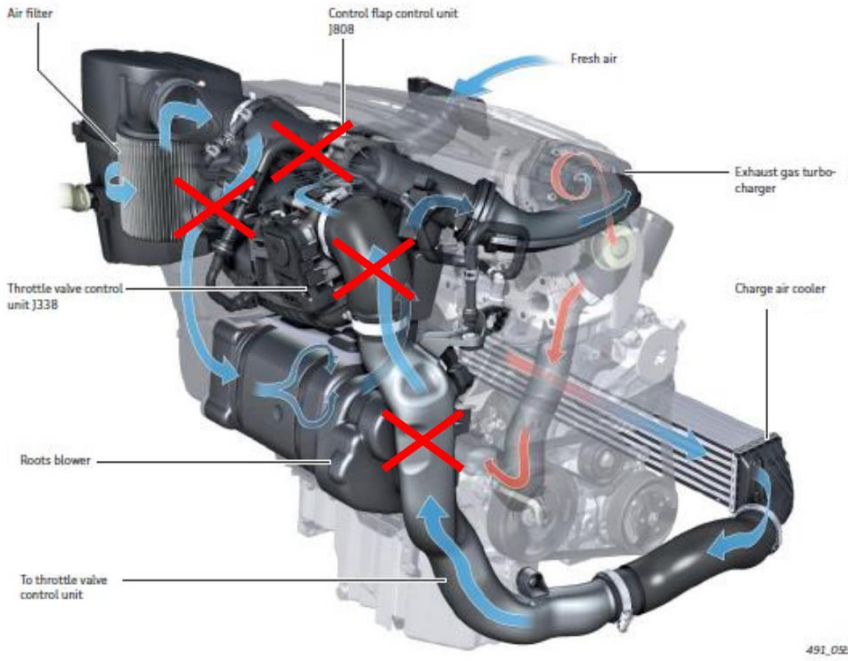

Figure 2.3 Air path modification on 1.4 VW TSI

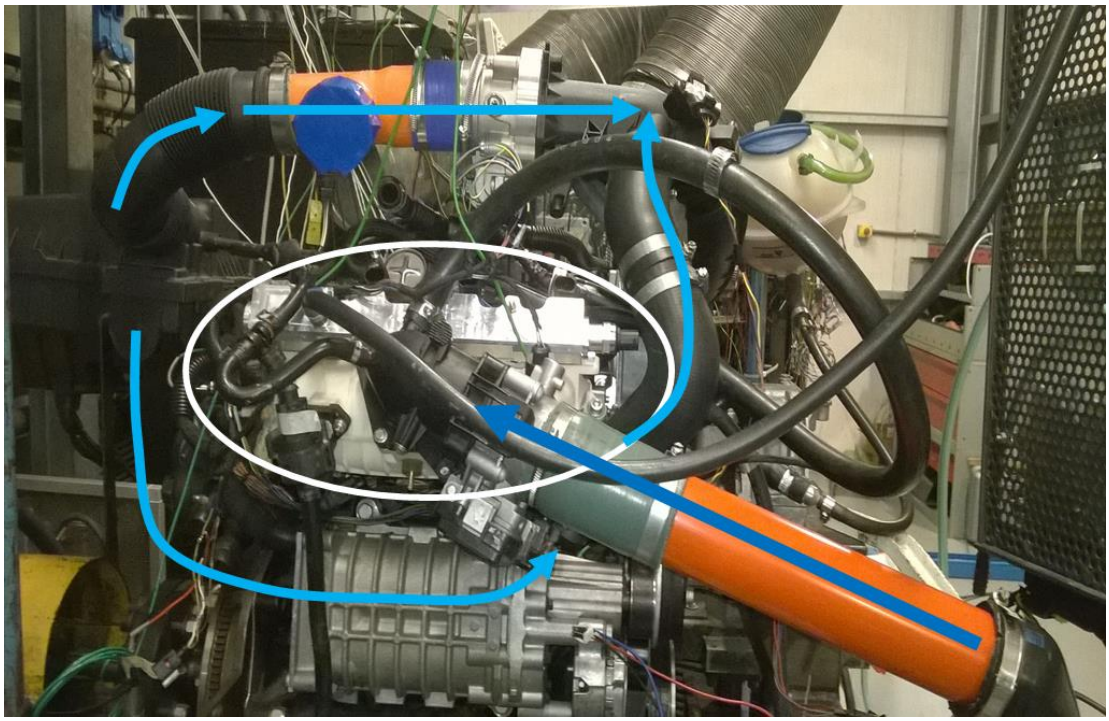

Figure 2.4 TSI setup. The white circle highlights the PWI system. The blue arrows show the new air path branches

2.1.3 Rapid Control Prototyping

A Rapid Control Prototyping System (RCP) has been developed to manage the WI system. In the first part of the activity, a first version of the system has been used to perform investigation campaigns or focused tests in which the injected water mass was externally imposed by the operator. During all the project the amount of injected water has been reported using the parameter *r*, defined as the ratio of injected water mass on the injected fuel mass (Eq.1):

$$r = \frac{m_{water}}{m_{fuel}} \qquad (1)$$

A synthetic scheme is displayed in Figure 2.5. During all tests, standard actuators of the engine have been managed by a development ECU. To manage the water injectors a dedicated WI Driver has been developed using a Real-Time hardware coupled with the ECU. The basic algorithm designed for the RT machine was initially able only to compute the necessary water injection time to obtain the externally set *r* value (Figure 3). To accomplish this goal, the hardware needs as inputs the values of RPM, fuel mass injected cycle by cycle and manifold pressure. In the first set-up, the signal from manifold pressure and the AFR sensor were split to be acquired by both the ECU and the RT machine. Furthermore, an air mass flow meter was added to the modified air path. Through both air mass flow and AFR measurements, the algorithm can compute the injected fuel mass.

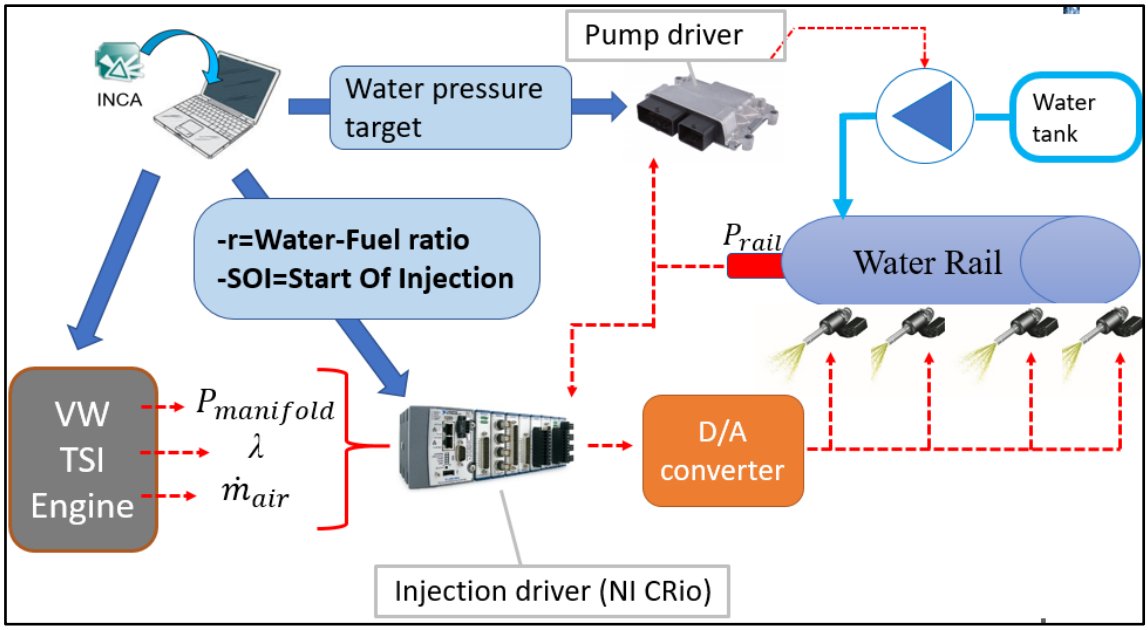

Figure 2.5 TSI setup control layout

The algorithm operates as a Real Time code (cycle by cycle) for each cylinder trough three steps. At first, the water mass to be injected is defined as a product of fuel mass injected and r. Then, water mass and pressure drop between water rail and manifold are used in the injector characteristic to define injection duration. At last, using the engine toothed wheel and the combustion phasing signal as a reference, through a fixed Start of Injection angle input (set by the test-bench management system) the injection timing is calculated. The determination of both injection timing and duration allows to define the ultimate profile of the injection pattern. This pattern is obtained sending a digital signal to the D/A Converter that finally transfers an analogic signal to each injector.

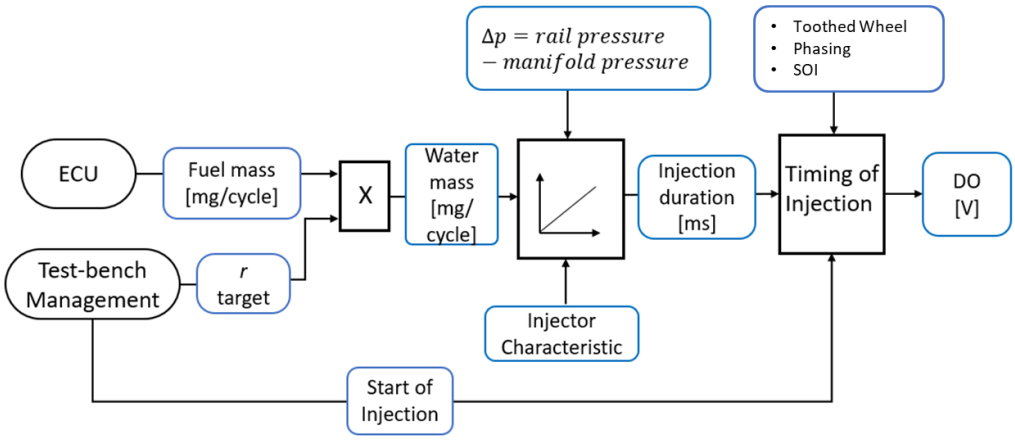

Figure 2.6 Water injectors control system

To test the WI controller, the algorithm developed in SiL has then been integrated in the RT code. After this upgrade, the controller provides (cycle by cycle) the r value to the Port WI system and a new SA value to the ECU, and at the same time it must receive several combustion indexes: the MFB50 and the knock index MAPO (Maximum Amplitude of Pressure Oscillation). A complete description of WI controller and its inputs and outputs is given in Chapter 5.

Two new CAN communication networks have been set-up to upgrade the RCP system and to integrate the control software.

1. cRIO-ECU line. The software can read directly from the ECU parameters like load, speed, fuel mass injected (cycle by cycle) and manifold pressure. In opposite direction the software can write the SA to be applied
2. Indicating system-cRIO. Reading of MFB50 angle and MAPO (cycle by cycle).

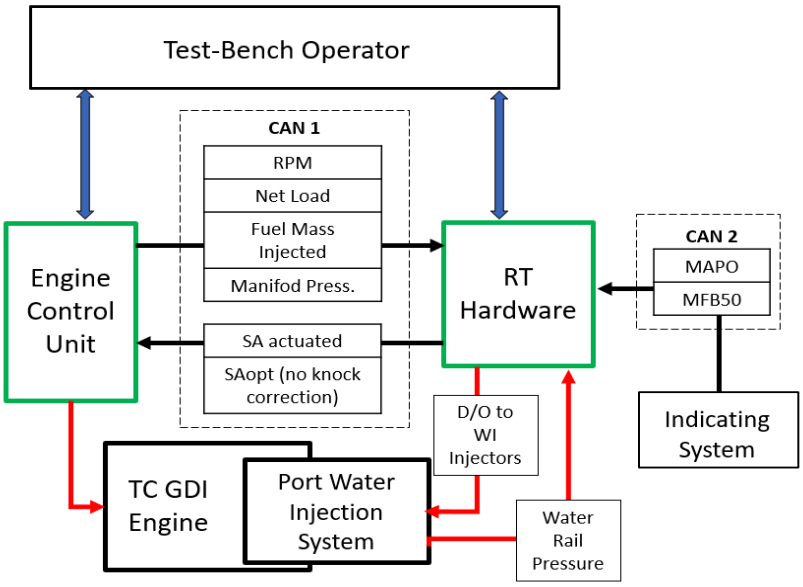

Figure 2.7 Overall Rapid Control prototyping system

2.2 New Experimental set-up

In the last part of the project, a different set-up has been involved, including a different GDI engine. This set-up, managed externally by Marelli Europe S.p.A., has been used to obtain more data for the study of WI technology and also for the MFB50 Estimation described in Chapter 8. The engine used for this activity is an in-line 4 cylinders SI TC engine, and its main features are summarized in Table 2-2. The engine is equipped with two accelerometers as standard production equipment, one located between cylinders 1 and 2 (Acc12)

and the other one located between cylinders 3 and 4 (Acc34). The accelerometric signal is acquired with a sampling frequency of 200 kHz.

Table 2-2 Engine Features

Displaced volume	1995
Stroke	90
Bore	84
Connecting Rod	163
Compression ratio	10
Number of Valves	16
Exhaust Valve Open	10 Before BDC
Exhaust Valve Close	15 After TDC
Inlet Valve Open	50 Before TDC
Inlet Valve Close	75 After BDC

3 First Investigation on WI effects

3.1 Variation of *r* and SA

The first investigation on the WI prototypal engine, described in 2.1, has been carried out to perform a preliminary analysis on the main effects on combustion. The test conditions are summarized in the next table.

Table 3-1 Test condition

RPM	3000
Manifold Pressure [barA]	1.5
AFR	1
VVT	disabled
Water Rail Pressure [barA]	10
Start of Injection [CA aTDCf]	360

The main controlling parameter in a SI combustion is the Spark Advance angle, and usually the optimization of combustion efficiency is evaluated through SA sweeps at fixed speed and load conditions. Therefore, to study the Water Injection effect, several SA sweeps have been performed at different values of *r*. At first, the effect of WI on MFB50 has been evaluated. In Figure 3.1 the correlation between MFB50 and SA has been reported at different r values. The effect of WI is clearly a delay on MFB50, in fact for each SA applied the resulting combustion phasing is proportionally retarded as long as *r* increases. At the same time, the relationship between SA and MFB50, at same *r*, displays a parabolic profile at every condition.

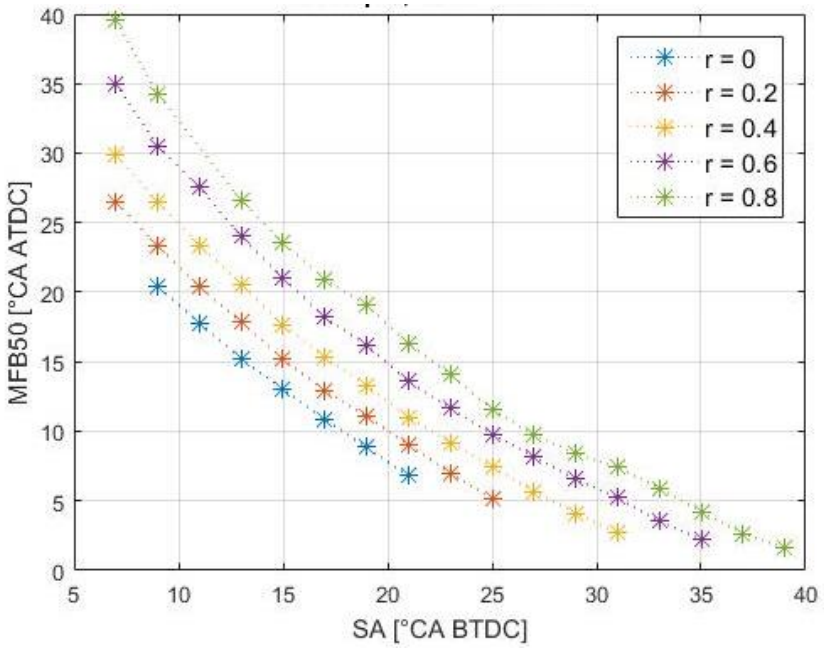

Figure 3.1 Correlation between SA and MFB50

Both these considerations are relevant findings that have led to the main core of the project.

The effect of water can be highlighted in Figure 3.2. At same SA, the injected water quantity proportionally slows down the combustion, delaying the phasing and reducing the peak. Due to MFB50 delay the Indicated Mean Effective Pressure (IMEP) covariance is actually increased as long as the water fuel ratio increases, as seen in Figure 3.3

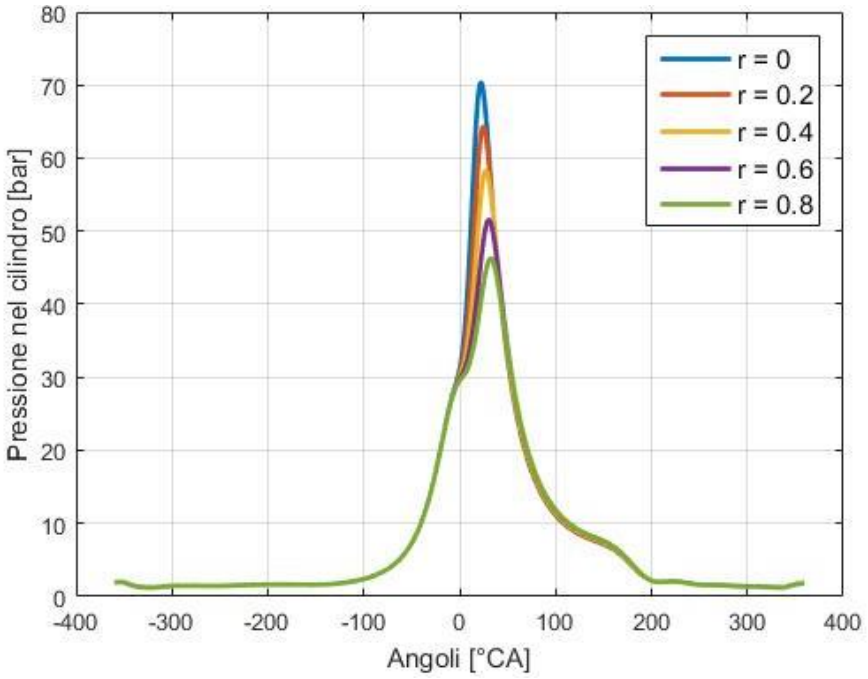

Figure 3.2 In-cylinder pressure profile for one cycle at different r values at SA=12° bTDCf

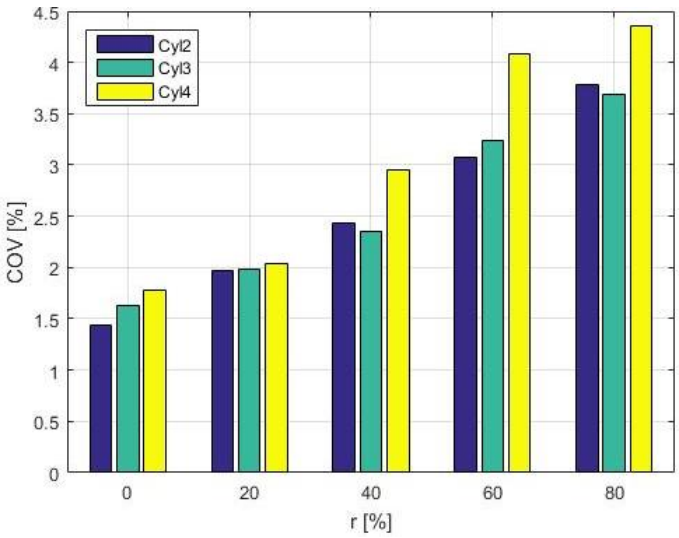

Figure 3.3 Cycle to cycle IMEP COV at SA=13 bTDCf

Another important consequence of water injection is the mitigation of knock. Figure 3.4 displays the trend of knock tendency, represented by MAPO98 index at different *r* values. The mitigation effect at same SA is

clear but since WI changes the combustion phasing a proper combustion analysis must consider the same MFB50 condition, focusing on the black dotted line which represents the MAPO98 values at same MFB50=9 CA. This representation highlights that in presence of knocking condition the injection of a water-fuel ratio of 0.2 can reduce effectively the MAPO98 [22]. There is not a linear relationship between *r* increasing and MAPO98 mitigation, therefore the more MAPO98 is lower, the more *r* increment is needed.

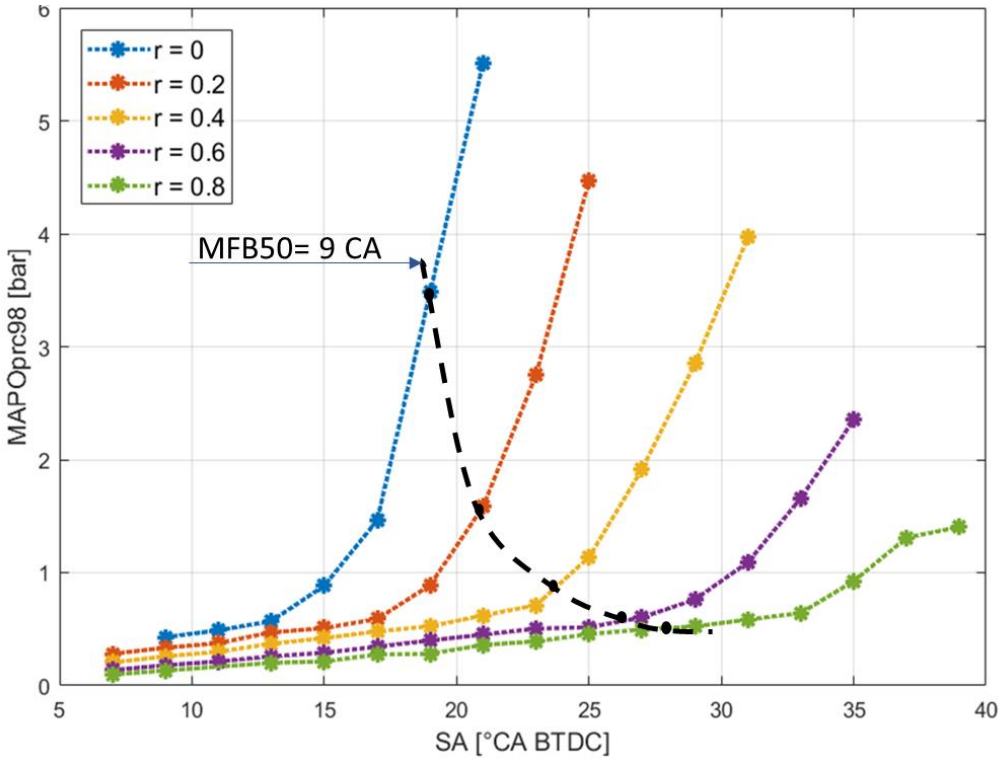

Figure 3.4 Trend of MAPO98 at different r value. The black dotted line represents the MFB50=9° aTDCf condition

A deeper analysis of combustion has been carried out to study the evolution of Cumulative Net Heat Release (CHR) curve at different *r* values applied. This curve provides a representation of the evolution of fuel mass burned fraction during the combustion phase on angular domain. To obtain this curve the net heat release rate $\frac{dQ_n}{d\theta}$ must be calculated using the equation below in Eq.2 and reported in [23].

$$\frac{dQ_n}{d\theta} = \frac{1}{n-1} * V * \frac{dp}{d\theta} + \frac{n}{n-1} * p * \frac{dV}{d\theta} \qquad (2)$$

Where:

- *n* is the polytropic coefficient for the real cycle
- *p* is the in-cylinder pressure obtained by indicating system
- *V* is chamber volume, function of crankshaft angle θ

$\frac{dQ_n}{d\theta}$ describes the derivative on crankshaft angle of the heat transferred to the gas by the fuel oxidation process. This "net" heat is not affected by the loss due to the thermal exchange with walls and for leakage. The integration of $\frac{dQ_n}{d\theta}$ in an angular window correlated to the combustion phase leads to the CHR curves displayed in Figure 3.5, for constant SA. In this picture the effect of *r* on the trend of MFB along the combustion phase is clear, all the process is elongated proportionally to the increment of *r*. Furthermore, on each CHR profile the positions of MFB1, MFB50, MFB90 (respectively the 10%, 50% and 90% of mass fuel burned) have been highlighted.

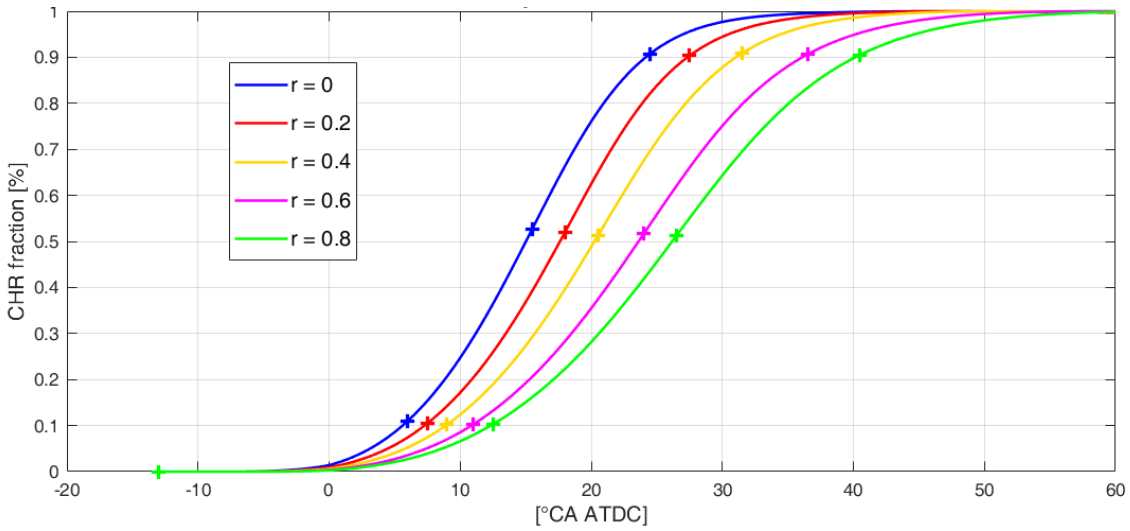

Figure 3.5 NET CHR fraction for average cycle at SA=13° bTDCf at different r values

For a wider analysis, the overall combustion time (evaluated as angular length between MFB0 and MFB90) of every tested point has been plotted on same graph, and this time the points are defined by MFB50 angle instead of SA to delete the bias (the inevitable delay effect) produced by WI effect. The final graph is represented by Figure 3.6.

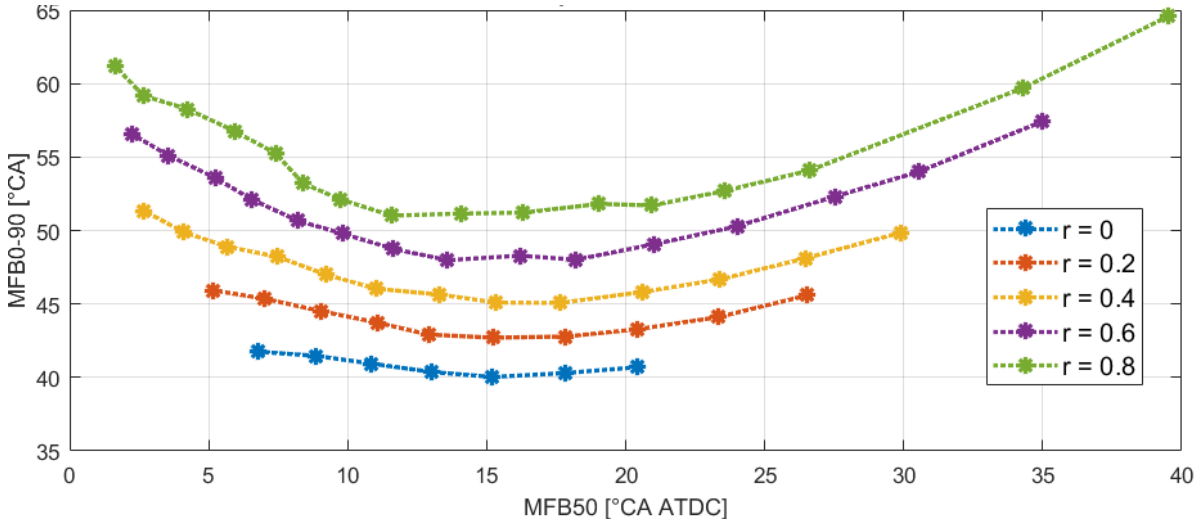

Figure 3.6 Angular duration between MFB0 and MFB90 compared at same MFB50, at different r

The most important finding from this graph is the detection of the combustion elongation produced by water that can be isolated by considering operative points with same MFB50. This elongation is enhanced when MFB50 is far from optimal position (too delayed or too advanced). The same analysis has been repeated splitting the combustion angular time in three parts: from MFB0 to MFB10, from MFB10 to MFB50, from MFB50 to MFB90, respectively displayed in Figure 3.7, Figure 3.8, Figure 3.9. These figures highlight very clearly in which section the water injected has an impact. In fact, the increase of *r* can expand the MFB0-MFB10 part from 20° to 25°-30° depending on the combustion phasing. This effect is more relevant especially for advanced MFB50 conditions. The effect of *r* is also shown in Figure 3.10, representing the in-cylinder pressure profile of the combustion phase, considering only points with MFB50 close to 9° CA aTDCf to match the evolution of combustion dynamics in presence of increasing water injection at comparable combustion phases.

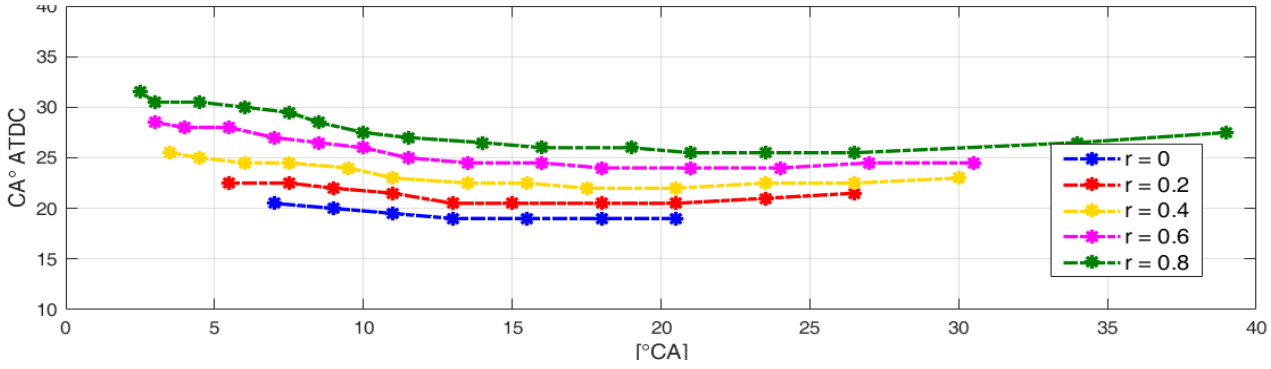

Figure 3.7 Angular duration between MFB0 and MFB10 compared at same MFB50, at different r

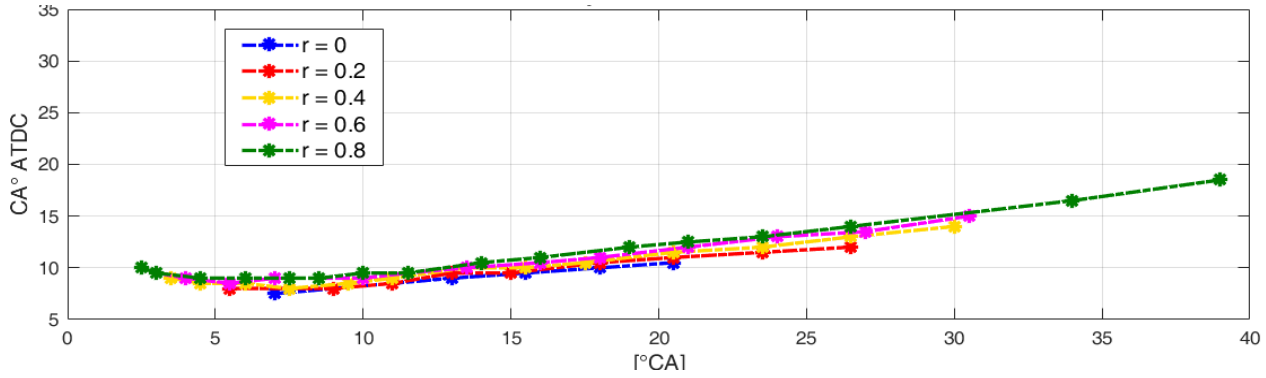

Figure 3.8. Angular duration between MFB10 and MFB50 compared at same MFB50, at different r

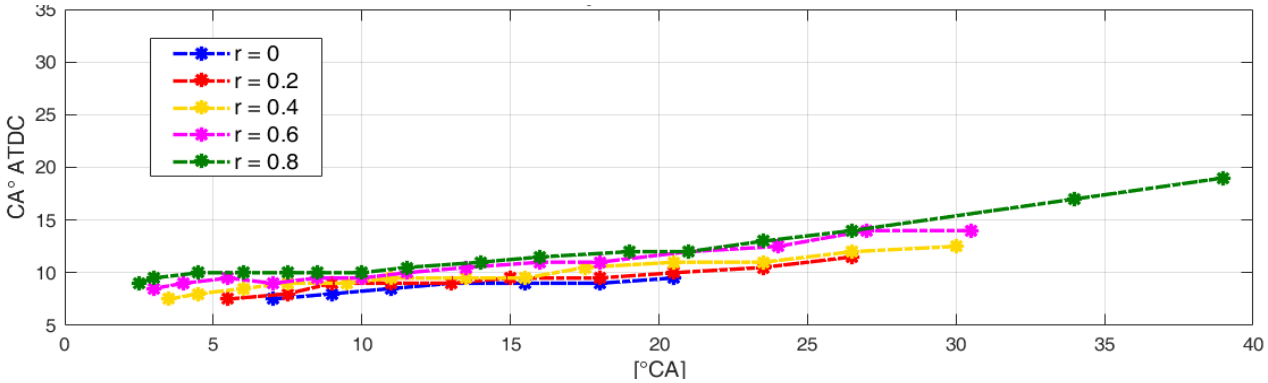

Figure 3.9 Angular duration between MFB50 and MFB90 compared at same MFB50, at different r

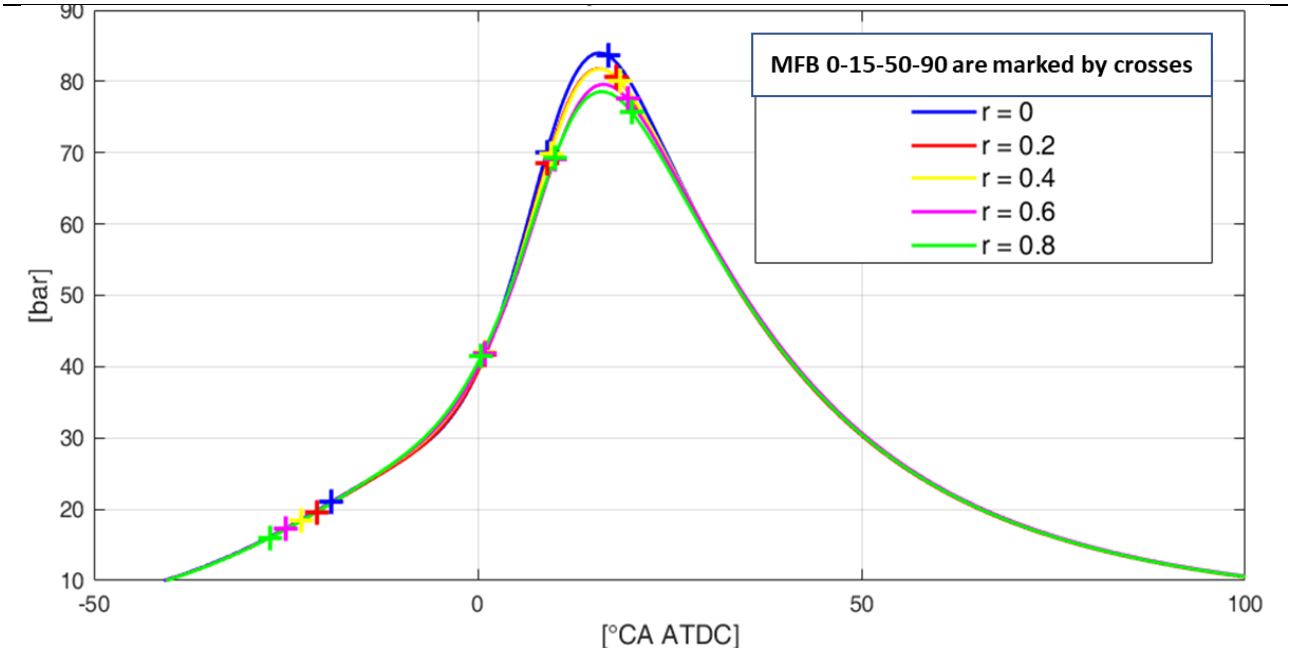

Figure 3.10 Effect of WI on combustion on In-cylinder pressure for points with MFB50 close to 9° CA aTDCf.

In conclusion, the analysis from this first investigation campaign highlights a delaying effect of the water on the combustion dynamics. Summarizing:

- The relationship between MFB50 and SA can be fitted by a 2nd order polynomial function. The water-fuel ratio increase further delays the angular position of MFB50, but the relationship is still fitted by the same kind of function
- The delay effect is mainly focused in the early combustion phase (MFB0-10). The following process is less affected, therefore, the combustion of water injected can be shifted to the desired phasing advancing the SA angle
- At same MFB50, the injection of water can actually mitigate the knock tendency.

These findings have been the base for the development of the WI combustion controller described in Chapter 5.

3.2 Start of Injection Effect

After a general evaluation of the effect on combustion related to the injected water mass, another preliminary investigation has been carried out to study the effect of injection phasing. In this case the test has been performed with the following condition.

RPM	2500
Manifold Pressure [barA]	1.5
Water Rail Pressure [barA]	[3 9 20]
Start of Injection [CA bTDCf]	[0:120:720]
SA [CA bTDCf]	14
Water-fuel ratio	0.4

The effect of SOI has been studied using 2 possible feedback parameters: MFB50 and temperature inside intake runner. In this case, a variation of rail water pressure has been taken into account to consider also the effect of different injection time durations. It can be seen in Figure 3.11, Figure 3.12 and Figure 3.13 that the variation of SOI does not lead to significant effects on MFB50. From the perspective of the runner temperature, the effect is more relevant. In other words, the injection phase has an impact on runner wall cooling.

The very poor effect of SOI on MFB50 can be explained considering the sub-optimal lay-out of the TSI runner. In fact, there is a too long path that water droplets must travel to reach the cylinder and in the last part of the duct there is a bend. If the spray is injected before the intake phase, the droplets inevitably impact the wall, increasing the water film. On the other hand, if the spray is injected during intake phase the droplets are dragged by the air flow but great part of the liquid water impacts the wall and the valves. This phenomenon is described in [25], in which a CFD analysis has been carried out on the same set-up. Therefore, in every case great part of the injected water reaches the cylinder in vapor form.

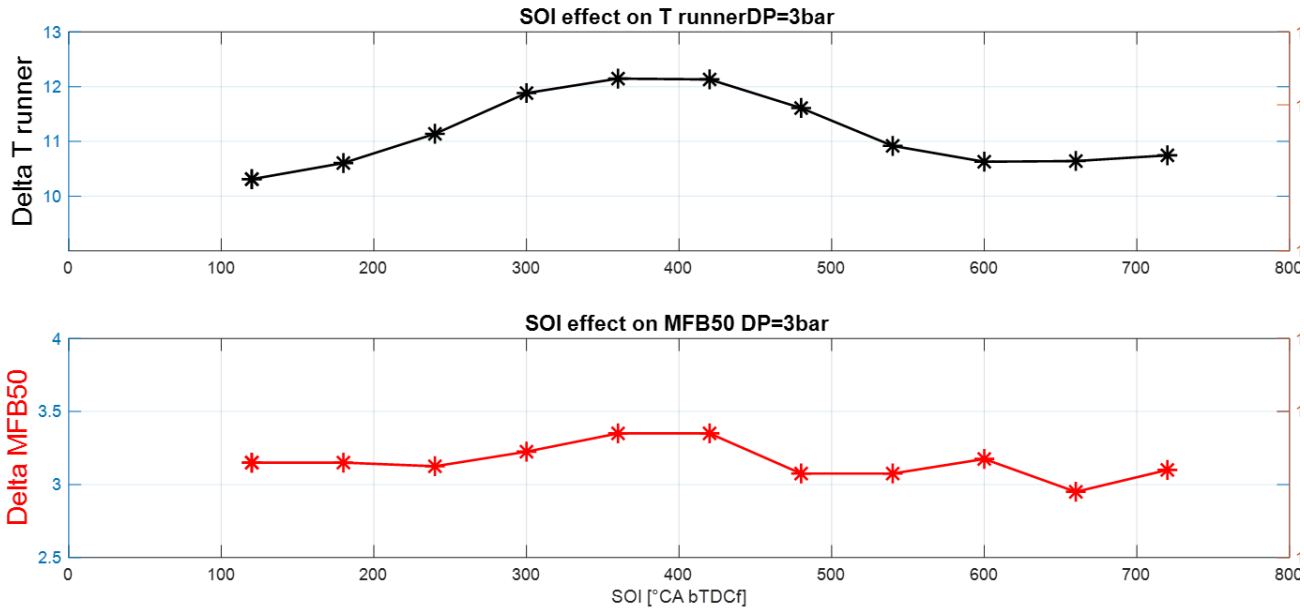

Figure 3.11 On top temperature reduction (as absolute) inside runner, at bottom variation of MFB50. Both values in respect to case without WI. The pressure gap between water rail and intake manifold fixed at 3 bar.

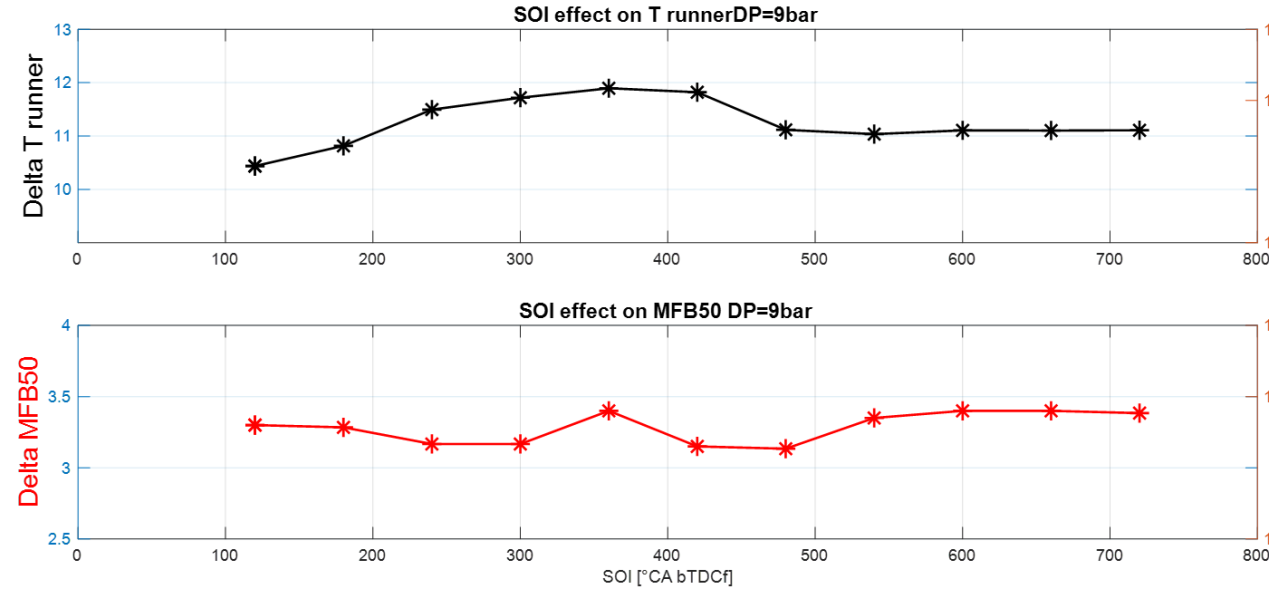

Figure 3.12 On top temperature reduction (as absolute) inside runner, at bottom variation of MFB50. Both values in respect to case without WI. The pressure gap between water rail and intake manifold fixed at 9 bar.

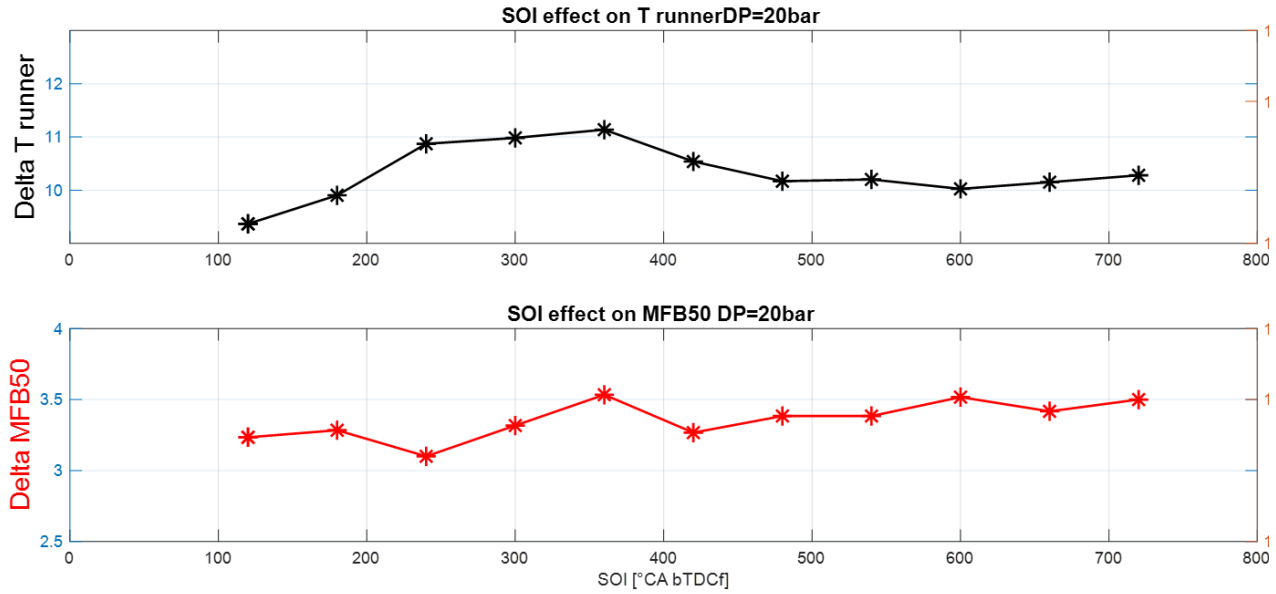

Figure 3.13 On top temperature reduction (as absolute) inside runner, at bottom variation of MFB50. Both values in respect to case without WI. The pressure gap between water rail and intake manifold fixed at 20 bar.

4 Combustion Model

This chapter presents the development of a combustion model able to compute the proper Spark Advance to obtain a target of combustion phasing (MFB50), at every operative condition (speed and Load), and taking into account the effect of Water Injection. This work represents the first step in the design of a controller oriented to WI technology management. The main contents of this chapter have been published in [27].

4.1 Calibration Campaign

A dedicated campaign has been planned on the set-up described in 2.1 to explore the effects of WI in a wide operating engine field, focusing on the areas with high knock tendency. Therefore, a grid of operating points has been defined by 2 levels of loads and 4 engine speeds, as shown in Table 4-1. The load is expressed with the Net Load (NL) parameter defined in equation below:

$$NL = pressure_{manifold} * \eta_{intake} \qquad (3)$$

Where η_{intake} is a factor that takes into account pressure drop within intake runners and valves.

Table 4-1 Experimental campaign summary

Engine point	Speed [RPM]	NL [bar]	λ	r
1	2500	1	1	0:0.2:0.8
2	2500	1.00	1	0:0.2:0.8
3	2500	1.4	1	0:0.2:0.8
4	3000	1	1	0:0.2:0.8
5	3000	1.33	1	0:0.2:0.8
6	3000	1.6	1	0:0.2:0.8
7	3500	1	1	0:0.2:0.8
8	3500	1.3	1	0:0.2:0.8
9	3500	1.6	1	0:0.2:0.8
10	3500	1.8	1	0:0.2:0.8
11	4000	1	1	0:0.2:0.8
12	4000	1.3	1	0:0.2:0.8
13	4000	1.6	1	0:0.2:0.8

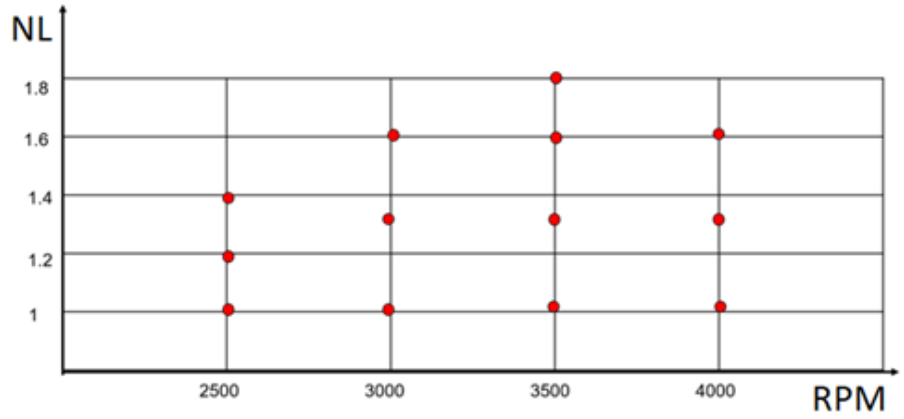

Figure 4.1 Calibration operative points

For each operating point the same investigation methodology has been carried out. It consists in the execution of a specific SA sweep at different *r* values that are applied in ascending sequence from 0 to 0.8, with incremental steps of 0.2. The angular SA step used in every sweep depends on Knock Limited Spark Advance (KLSA), and near Knock Limit Spark Advance (nKLSA). Such indexes define the SA angle that causes a knock tendency close to the safety threshold (KLSA) and close to 60% of the same threshold (nKLSA). The knock intensity is quantified as the 98th percentile of MAPO [22]. It is defined as the value below which 98 percent of MAPO index values are contained, in a sorted set of consecutive combustions. The threshold for this index is defined as:

$$MAPO98_{threshold} = \frac{RPM}{1500} \qquad (4)$$

The first element (*SAfirst*) of each SA sweep is defined as below, unless the limit on maximum exhaust gas temperature is exceeded:

$$SAfirst = SAbase + \frac{3*r}{0.2} \qquad (5)$$

In which:

- *SAbase* is the calibration value of SA
- The 3 CA offset has been arbitrarily assumed as the average value of combustion delay related to a step of 0.2 *r*

In conclusion the SA sweeps are carried out with the following specifications:

1. Angular steps of 3CA from *SAfirst* to nKLSA
2. Angular steps of 1 CA from nKLSA to KLSA

This methodology has been conceived to obtain a wide vision of WI effects on MFB50 and, at the same time, to investigate with more accuracy all combustion indexes near the KLSA area.

4.2 WI Combustion Model

Experimental data has been processed, point by point, to analyse the relationship between SA and MFB50, for each tested *r* value. For a single spark sweep, the most appropriate fitting function to analytically describe the relationship between SA and MFB50 is the quadratic polynomial, as clearly shown in Figure 4.2. Such figure displays some spark sweeps for different values of parameter *r*, highlighting the influence of such parameter on the trend that could be identified in the absence of water injection. Therefore, a parabolic function (Eq.6) can define polynomial fitting of the SA on MFB50 domain.

$$SA = a\,MFB50^2 + b\,MFB50 + c \qquad (6)$$

This analysis allows to conceive a WI Combustion Model that processes the RPM, NL, *r* and the target of MFB50 as inputs, to compute the corresponding SA to be applied. The base concept is to calculate the parameters a, b and c of the parabolic function and investigate the analytical dependence of each parameter from the *r* value. Three different methods have been designed to build such model, and the respective performances have been evaluated by comparing experimental and modelled SA. The fitting quality has been quantified for each proposed method by evaluating the correlation coefficient.

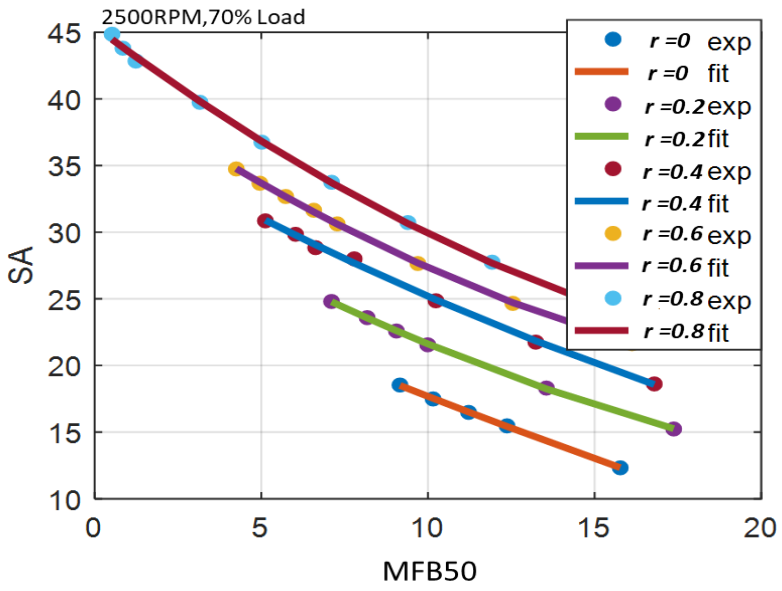

Figure 4.2 Parabolic fitting of the SA trend with respect to MFB50, for the engine point characterized by NL=1.2 and RPM=2500, and for different water-to-fuel mass ratios. It is an example of the parabolic trend that links the SA to the MFB50 for fixed operating conditions

4.2.1 Polynomial Model

Through the parabolic fitting of MFB50 and SA data for each engine point and for each value of *r,* the three coefficients *a*, *b, c,* (called Parabolic Coefficients), have been identified. Each parameter has been fitted with a polynomial function of RPM and NL (Net Load), for each value of *r*. The resulting equation for *a, b* and *c* is the following:

$$PCoeff = p_{00} + RPM * p_{10} + NL * p_{01} + + RPM * NL * p_{11} + RPM^2 * p_{20} \quad (7)$$

Where $p_{00}, p_{10}, p_{01}, p_{11}, p_{20}$, are called Surface Coefficients. Figure 4.3 shows all the resulting surfaces, for r = 0.

Every single surface is described by a set of 5 Surface Coefficients p_{xx} and each coefficient features a quite constant slope in *r* domain as displayed in Figure 4.4, so it can be fitted with a linear function:

$$p_{xx} = o_{xx} + r * g_{xx} \quad (8)$$

Where o_{xx} is the constant term and g_{xx} the curve slope.

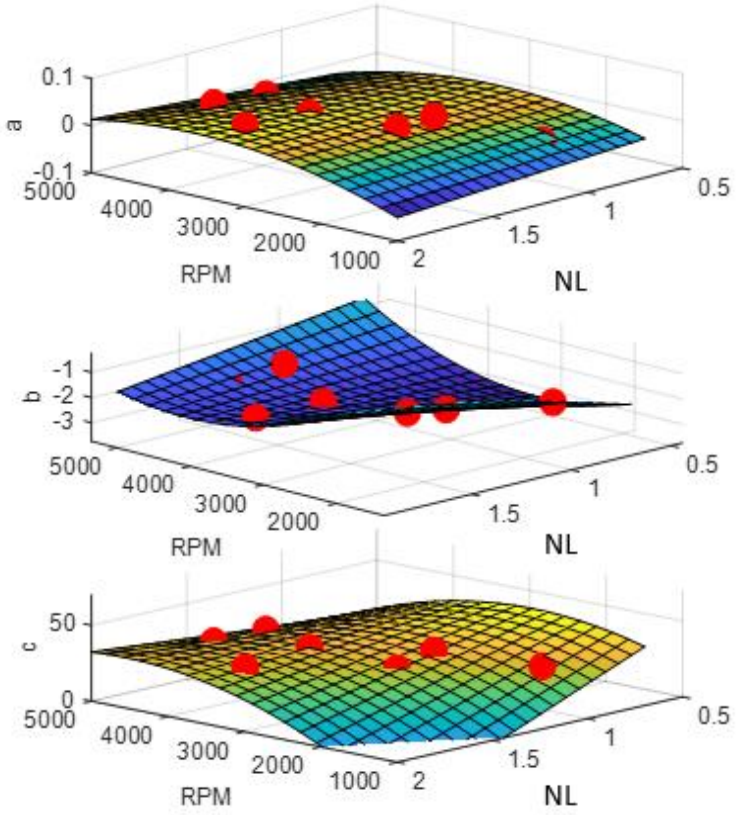

Figure 4.3 Fitting surfaces of the parabolic coefficients in (RPM, NL) domain, for r=0. The calibration points are displayed as red dot.

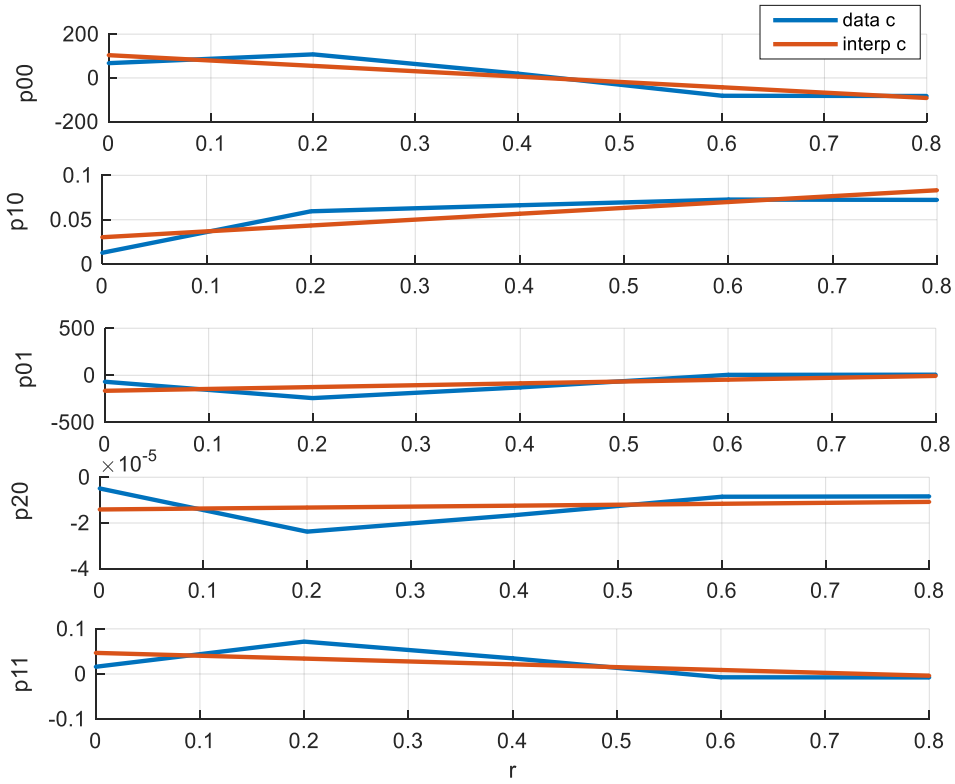

Figure 4.4 Fitting of surface coefficients by linear function.

Figure 4.5 shows a block diagram of the model based on polynomial fitting, relating the SA to the MFB50 target, for different combinations of *r*, RPM, and NL (i.e., the model inputs).

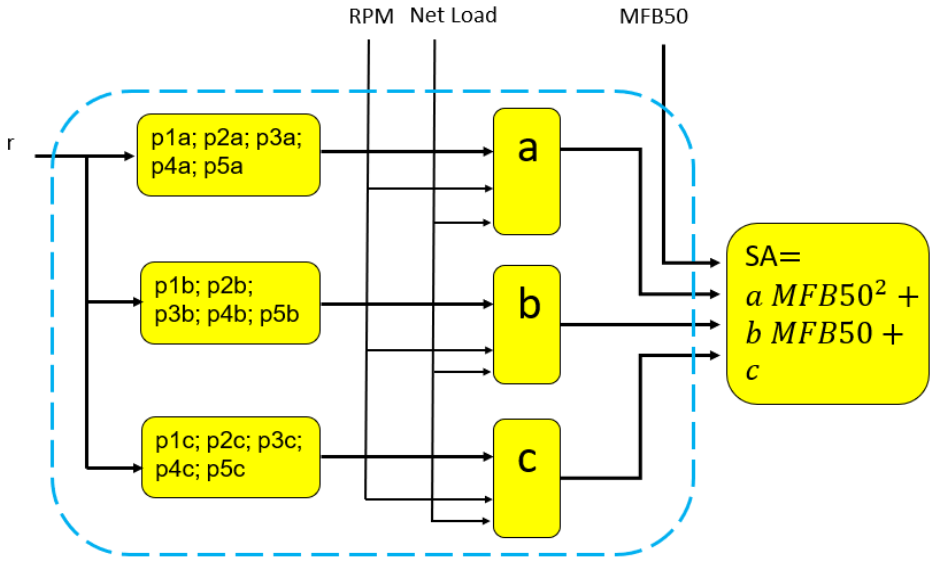

Figure 4.5 WI Combustion Model layout

4.2.2 Effects Separation Method 1-D

To verify the possibility of reducing the computational load and the allocated memory, other two implementation methods of the MFB50-SA open-loop combustion model have been investigated.

The first one is the simplest and fastest one, where the effects of water-to-fuel ratio, described by the parameter r, are considered to be independent of speed and load. With this method, the mean surface for r=0.5 of parameters a, b and c has been calculated and it has been defined as the reference between all surfaces obtained for the different r values (Figure 4.6).

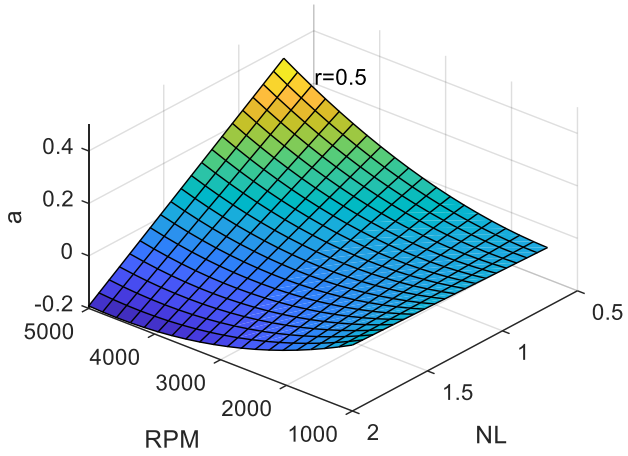

Figure 4.6 The calculated surface of parameter a, for r=0.5

Every coefficient has then been identified for all values of parameter r, for each engine point. Such values have been normalized with respect to the value which corresponds to r=0.5. The final trend is then described by the mean of the normalized values. In this way, such curve represents the gain of the related parameter which adapts the reference parameter value when r is different from 0.5. The three normalized curves are discretized as arrays called Ka, Kb, Kc, with r as input. In Figure 4.7 the trend of Ka for each engine point and the mean curve are shown.

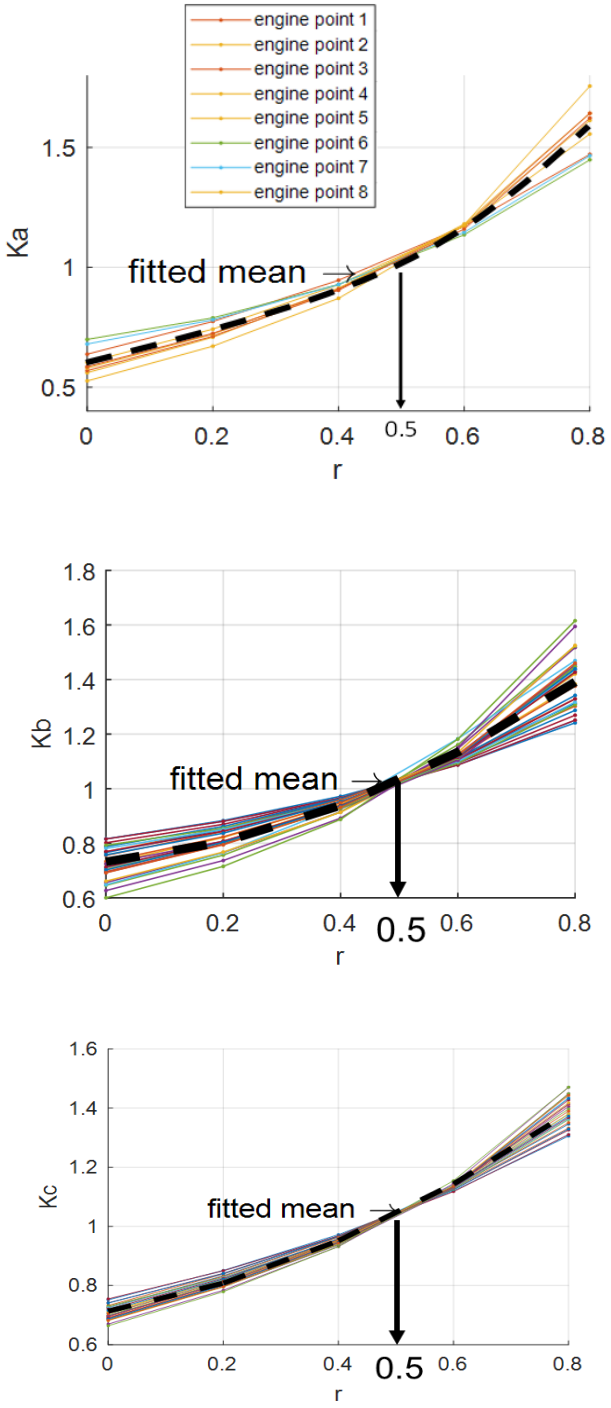

Figure 4.7 From top: Normalized curve Ka, Kb, Kc

In other words, the final approximated coefficient value can be recovered by multiplying the gain identified by the injected water mass *r* with the respective value of the same parameter at *r*=0.5, which depends on the engine point (RPM, NL). Figure 4.8 shows a block diagram of the model based on full mono-dimensional effects separation.

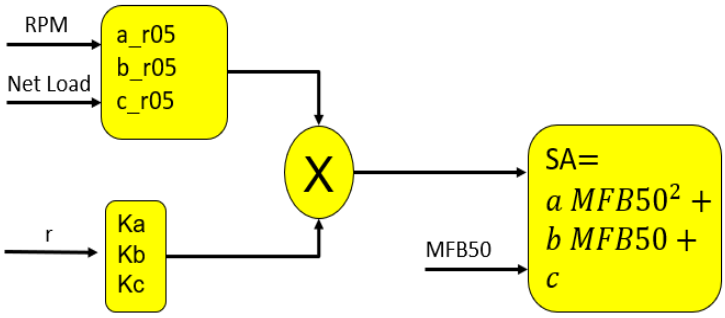

Figure 4.8 Combustion model with Separation Effect 1-D.

4.2.3 Effects Separation Methods 2-D

In this case, a degree of complexity is added to the previous model, by mapping the "correction" factors Ka, Kb and Kc as two-dimensional functions, depending on r and on another influent parameter, chosen between NL and RPM. To identify the most influencing factor, every coefficient has been displayed through two different representations, for each engine point. First, as surfaces on r-RPM domain, and second, as surfaces on r-NL domain. For both representations, a normalization over the 0.5 r value has been investigated, and the mean of all normalized surfaces has been computed and displayed. The comparison between the two representations highlights that NL has more influence on surface gradient than RPM. Thus, in this method the gain has been replaced by a 2-D matrix with NL and r as inputs. Figure 9 shows a block diagram of the model based on partial effects separation.

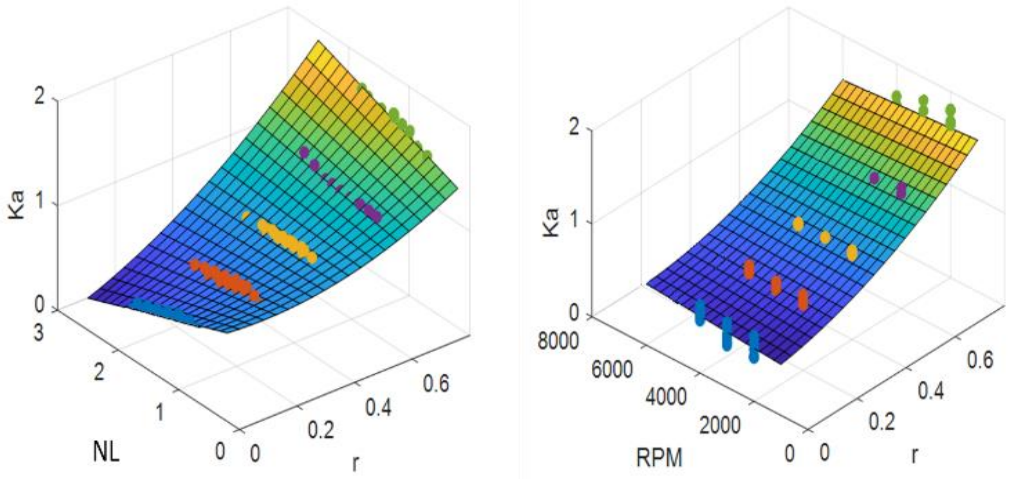

Figure 4.9 Average surface Ka on NL-r domain (left) and on RPM-r domain (right).

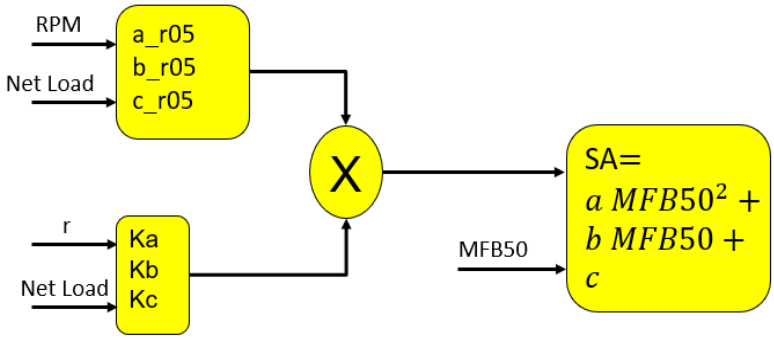

Figure 4.10 Combustion model with Separation Effect 2-D.

4.2.4 Comparison by Correlation Coefficient

To evaluate the accuracy of each method, the relative Correlation Coefficients ρ have been computed, as defined by the following equation:

$$\rho(A,B) = \frac{1}{N-1} * \sum_{i=1}^{N} \left(\frac{\overline{A_i - \mu_A}}{\sigma_A}\right) * \left(\frac{B_i - \mu_B}{\sigma_B}\right) \qquad (9)$$

Where:

- A is the array of the computed SA values by the different methods
- B is the array of experimental SA values
- μ_A and σ_A are the mean and standard deviation of A
- μ_B and σ_B are the mean and standard deviation of B

As shown in Table 3, the polynomial method produces the highest ρ value. Thus, this approach has been selected for control implementation. Also, the choice was relatively simple because in this phase of the project the computational burden of the controller has not been considered as a hard constraint.

Table 4-2 Correlation Coefficient values for the three different methods used to define the combustion model. The green box highlights the best result and the corresponding method.

Method	Polynomial	Eff. Sep. 2-D	Eff. Sep. 1-D
ρ	0.99	0.97	0.91

4.3 Model Validation

The accuracy of this Combustion Model can be evaluated on both experimental setups. The performance in obtaining a MFB50 angle from a target value in the TSI setup will be highlighted in Chapter 7, when the experimental validation of the overall controller will be presented. The setup described in 2.2 has also been used for an analysis of model response on a wide database. The calibration dataset is displayed in Table 4-3, and the validation dataset is displayed in Table 4-4.

Table 4-3 Calibration dataset

RPM	Net Load
1500	1.2
2000	0.8 1 1.2 1.6
2400	0.8 1 1.2 1.6 2
3000	0.8 1 1.2 1.6 2
3600	0.8 1 1.2 1.6
4000	0.8 1 1.2 1.6
4400	0.8 1 1.2 1.6
5200	0.8 1 1.2

Table 4-4 Validation dataset

RPM	Net Load
1500	0.7 1.1
2500	0.53 0.87 1.36 1.8
3500	0.56 0.91 1.38 1.86
4500	0.6 0.98 1.38 1.89
5500	0.6 1.34

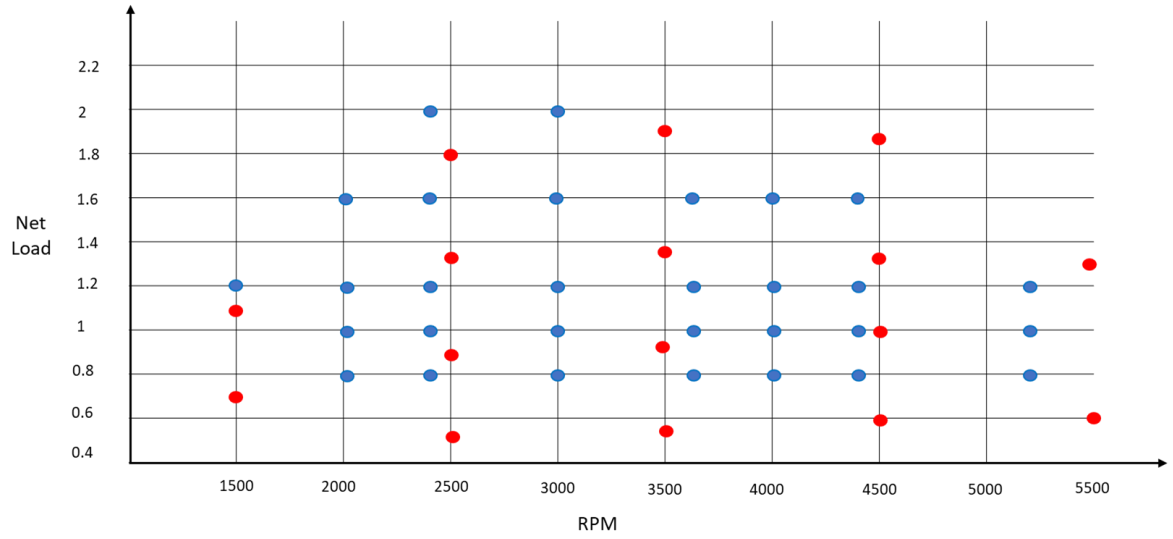

Figure 4.11 Calibration points (blue dots) and validation points (red dots)

To estimate the accuracy of the model, the error between the SA applied during a single experimental recording (or single engine point) and the SA computed by the model calibrated by the first dataset is considered. In Figure 4.12 it is displayed a comparison of the SA errors computed on calibration and on validation points. In the figure, great part of the error of the calibration data stays within ±1 CA. The validation data shows a similar response except for the points with Net Load below 0.8 and for a group of tests (inside the green circle) affected by registration error.

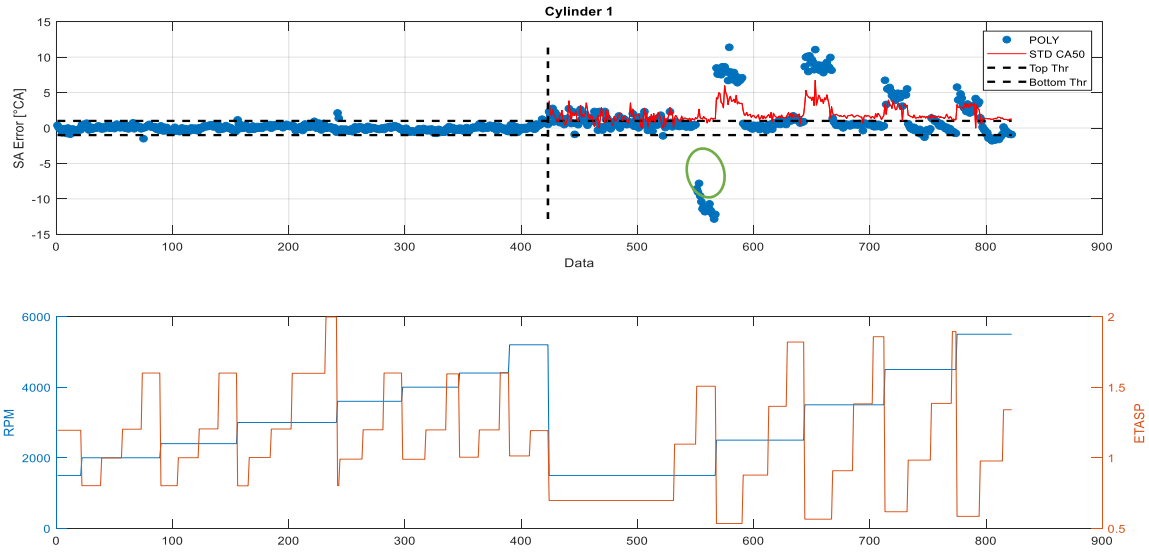

Figure 4.12 Comparison between validation points (left) and validation points (right).

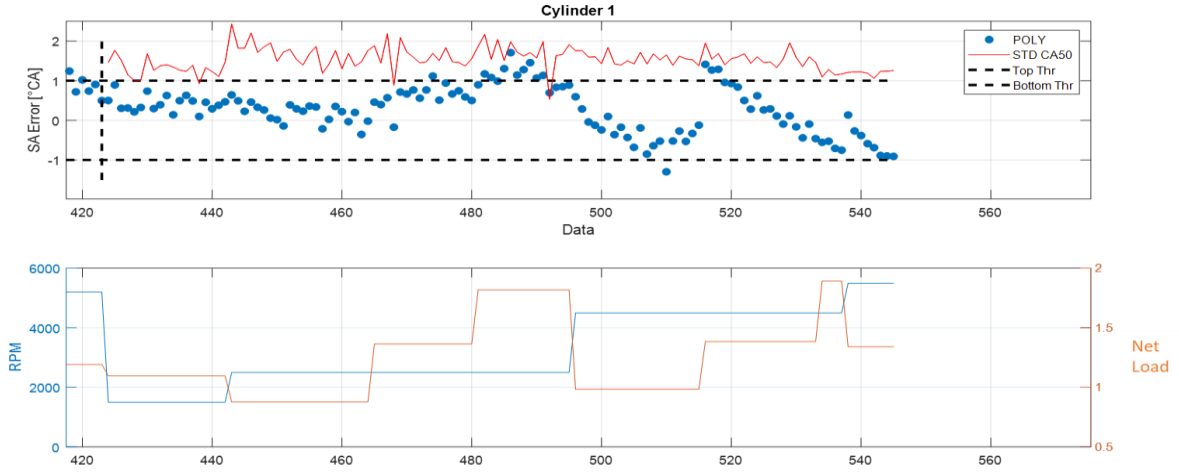

Figure 4.13 Focus on validation points for combustion model for Cyl1

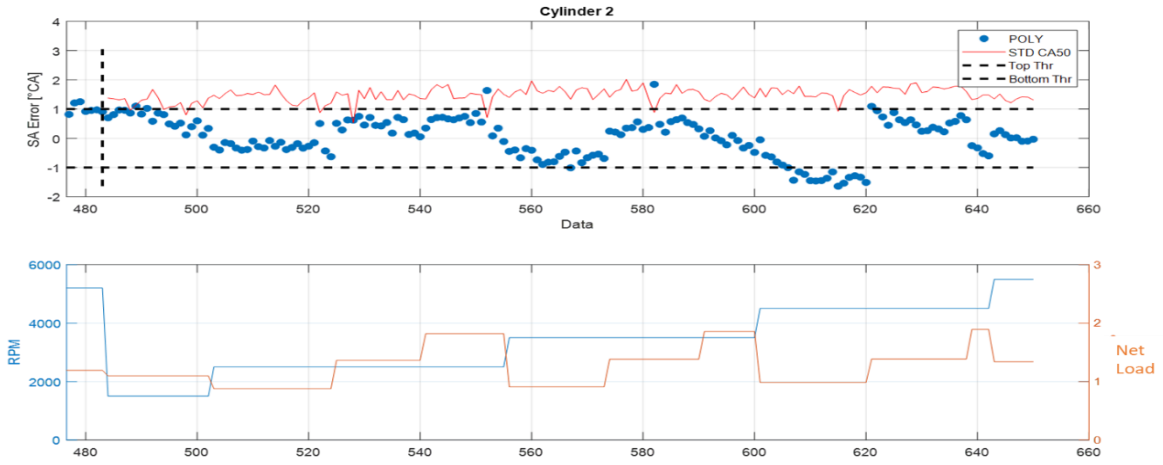

Figure 4.14 Focus on validation points for combustion model for Cyl2

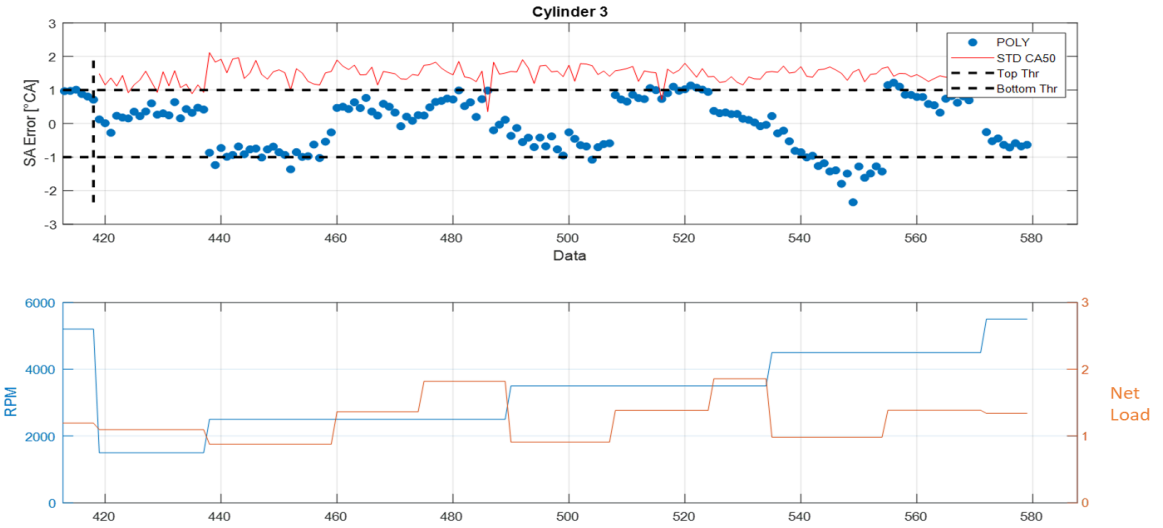

Figure 4.15 Focus on validation points for combustion model for Cyl3

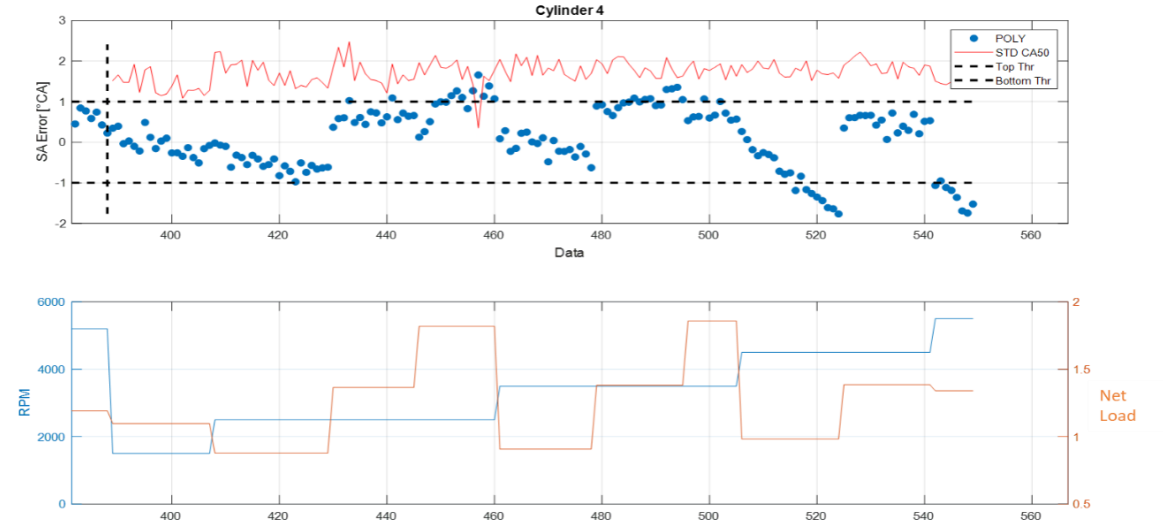

Figure 4.16 Focus on validation points for combustion model for Cyl4

In Figure 4.13 through Figure 4.16 the SA errors of the validation points excluding the ones inside the operative area below NL=0.8 are displayed. The SA error is mostly within ±1 CA also in validation points, except for the set at lower Net Load than the calibration field (see Figure 4.11).

5 Water Injection Combustion Control

The definition of a combustion model able to compute the SA required to reach the MFB50 target at a specific r, allows a WI combustion controller based on a combustion phasing target to be design. In this chapter a complete description of the development process of the controller is provided. The goal of the final controller is oriented to knock mitigation at high loads, while keeping MFB50 at its optimum value.

In the first version, the controller is able to reach a MFB50 target with an Open Loop lay-out requiring as inputs the water-to-fuel mass ratio (r) and the MFB50 target. For this reason, two look-up tables (one for r and one for MFB50) have been defined. In a second step, a CL operates to maintain the measured MAPO98 close to the threshold, with a statistical approach (MAPO98 is the 98th percentile of the MAPO distribution considered in the given buffer of MAPO values). A third version of the CL controller has also been developed. Such algorithm can control also the MFB50 by closing the loop on its measurement, to overcome errors of the combustion model and to meet the target. In this stage MFB50 measurement is achieved by indicating measurement system.

The performance of the 3 algorithms are evaluated simulating several steady state engine points and several transient conditions.

5.1 Open Loop SA Management

The developed OL branch requires a MFB50 target map and a r map, both based on RPM and NL (Net Load), to provide the necessary inputs for the combustion model. The first one provides the MFB50 target angle, and the second the nominal r value to be actuated. The model receives these 2 inputs together with RPM and NL and computes the proper SA to achieve the target.

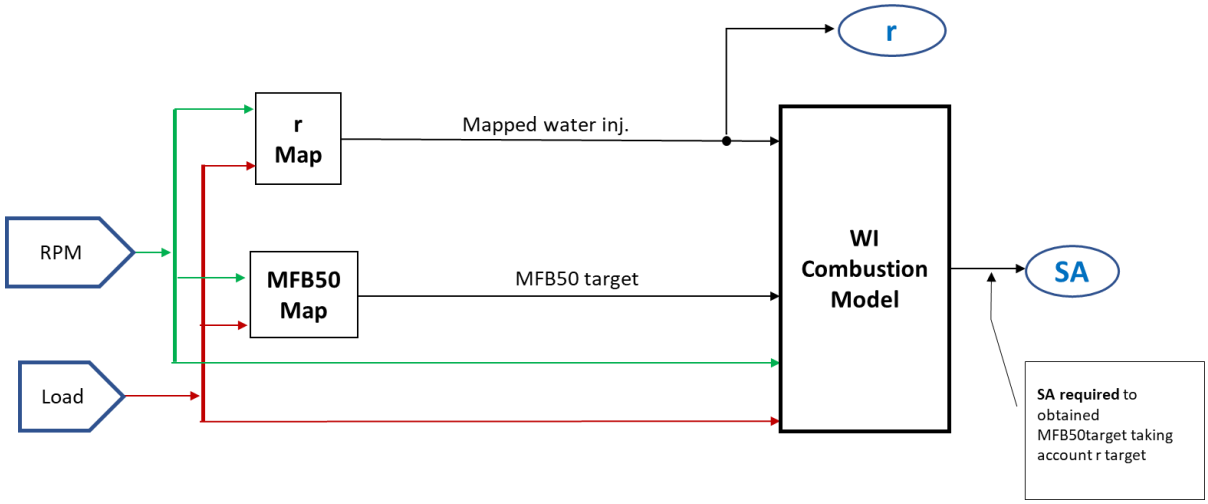

Figure 5.1 Open Loop WI Controller

The 2 maps (MFB50, *r*) are calibrated with the same methodology for all the investigated experimental points. The calibration methodology consists of three steps. At first, the required SA angles to target the optimum MFB50 (arbitrarily fixed to 8°CA ATDCF) are computed by processing the related parabolic function (Eq. 10), for all injected water masses, for each experimental point (Figure 5.2).

$$SA_{opt} = a\ MFB50_{opt}{}^{2} + b\ MFB50_{opt} + c \qquad (10)$$

Where:

- *a, b* and *c* are the coefficients of the parabolic function *SA=f(CA)*, for a *r* value and for a fixed engine point
- SA_{opt} is the spark angle which guarantees the $MFB50_{opt}$

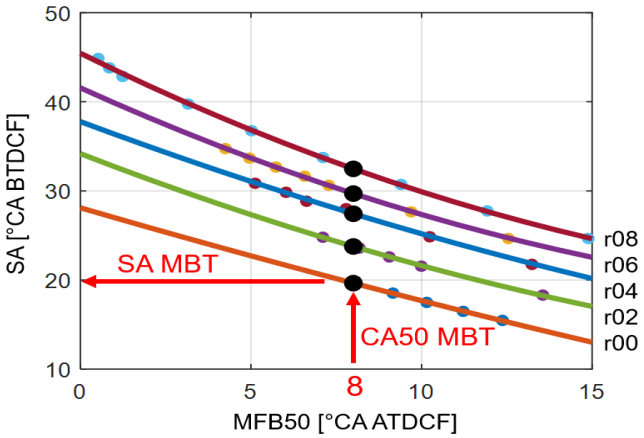

Figure 5.2 SA Maximum Brake Torque (MBT) determination procedure.

Then the MAPO98 values corresponding to optimum SA are determined by evaluating the exponential function, one for each *r* value (coloured curves in Figure 5.3):

$$MAPO98_{opt} = g\ SA_{opt}{}^{f} + k$$

Where:

- *g, f* and *k* are the parameters of the exponential function *MAPO98=f(SA)*, for a *r* value and for a fixed engine point
- $MAPO98_{opt}$ is the MAPO98 value obtained for the $MFB50_{opt}$

At last, optimal MAPO98 values are fitted with another parabolic function, described by next equation, on the *r* domain (red curve in Figure 5.3), and through intersection with MAPO98 threshold (KL, in Figure 5.3), it is possible to evaluate the minimum *r* value that guarantees a permissible MAPO98 (equal to 0.2 in the example shown in Figure 5.3, where the corresponding SA MBT is also highlighted):

$$r_{map} = m\ MAPO98_{thr}{}^{2} + n\ MAPO98_{thr} + l \quad (11)$$

Where:

- *m, n* and *l* are the parameters of the parabolic function $r=f(MAPO98_{opt})$, for each engine point
- r_{map} is the minimum *r* value which allows respecting the $MAPO98_{thr}$

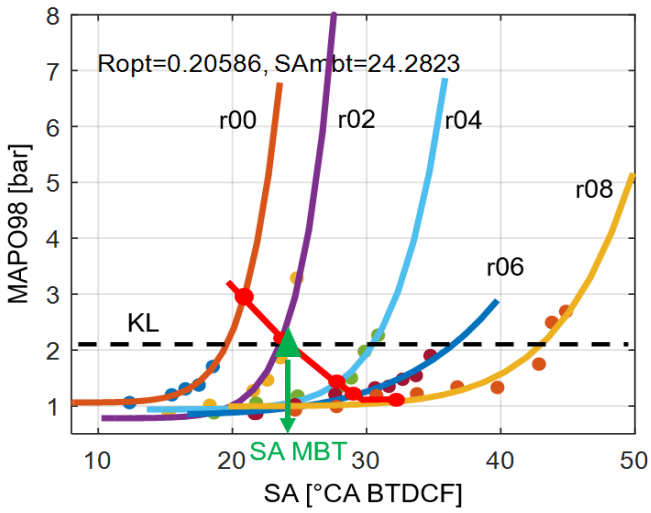

Figure 5.3 R map determination and related SA MBT.

When this value saturates at maximum *r* value allowed (arbitrarily fixed at 0.8), a spark retard is necessary to guarantee knock reduction. Thus, a new SA angle must be defined (Eq.12) in the intersection between the exponential MAPO98 function calculated for *r*=0.8 and knock threshold (Figure 5.4, where SA ACT does not correspond to SA MBT):

$$SA_{act} = e^{\frac{\log\frac{MAPO98_{thr}-k_{08}}{g_{08}}}{f_{08}}} \qquad (12)$$

Where:

- g_{08}, f_{08} and k_{08} are the parameters of the exponential function *MAPO98=f(SA)* for *r*=0.8, for a specific engine point
- SA_{act} is the spark advance actuated to obtain a MAPO98 equal to the threshold

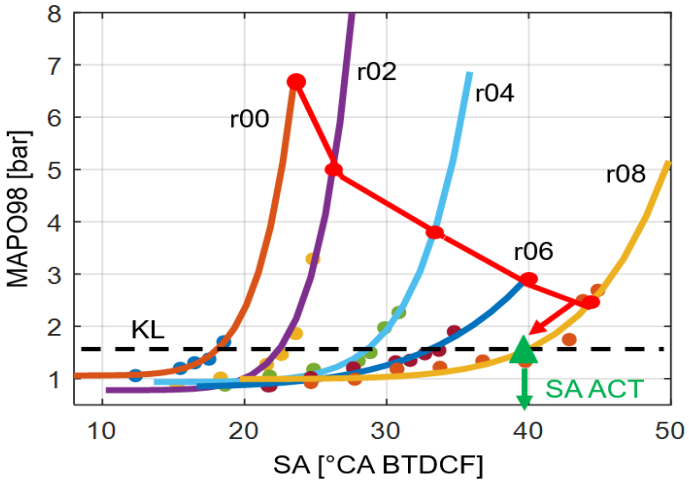

Figure 5.4 SA determination, when r is saturated to 0.8.

As a result, the MFB50 map provides the optimum value (equal to 8CA ATDCF) when *r* < 0.8 and a delayed value when *r* = 0.8. The experimental data demonstrate that this circumstance is never verified, and the parameter *r* does not saturate to the maximum value. Consequently, the MFB50 target is equal to 8 °CA ATDC on the entire operating field [26]. Moreover, the experimental tests have been carried out at the highest load for the tested engine speeds. Thus, for the operating filed characterized by lower load levels, the choice of a MFB50 target equal to 8 is absolutely legitimate. The resulting *r* map for the mean cylinder is shown in Figure 5.5. The consequent MFB50 target map within the explored range and for lower loads becomes a constant equal to 8.

After defining a *r* map, an investigation on benefit related to WI in terms of Brake Specific Fuel Consumption has been carried out. The analysis starts from the evaluation of the BSFC related to some of the calibration points used on TSI setup (Table 4-1) at *r*=0 condition and considering an AFR mapped value to keep knock level under the predefined threshold $MAPO98_{threshold}$ (Chapter 4). For each of these operative points defined by RPM and Net Load, the experimental BSFC values (recorded with stoichiometric AFR) have been fitted by a 2nd order polynomial function of *r* and MFB50 angle. In this way, the BSFC obtained applying the mapped *r* value is known. Thanks to the water injection, the same knock threshold can be obtained with a stoichiometric and the benefit can be seen in Figure 5.6 Figure 5.7 and in Table 5-1.

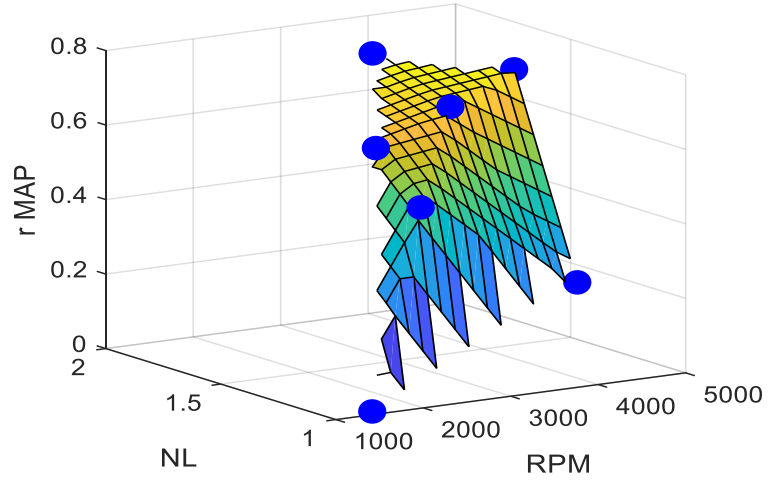

Figure 5.5 R map for the explored operative field.

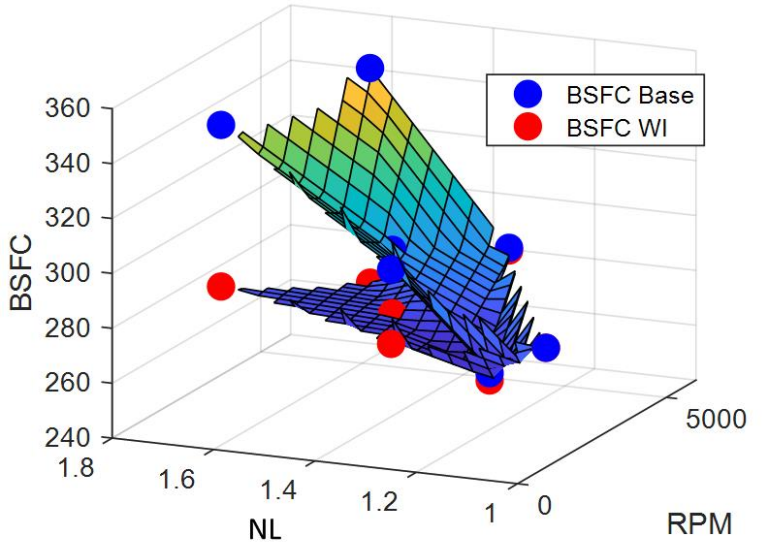

Figure 5.6 BSFC evaluation. Blue dots represent the base condition without WI, the red point represent the case with active WICC

Table 5-1 BSFC obtained in case of no WI (experimental data) and in case of activated WICC (simulation data)

Net Load	RPM	BSFC (without WI) [g/kWh]	BSFC (activated WICC) [g/kWh]
1.2	2500	260	257
1.4	2500	294	267
1.45	3500	293	270
1.8	3500	332	273
1.3	4500	292	290
1.55	4500	340	273

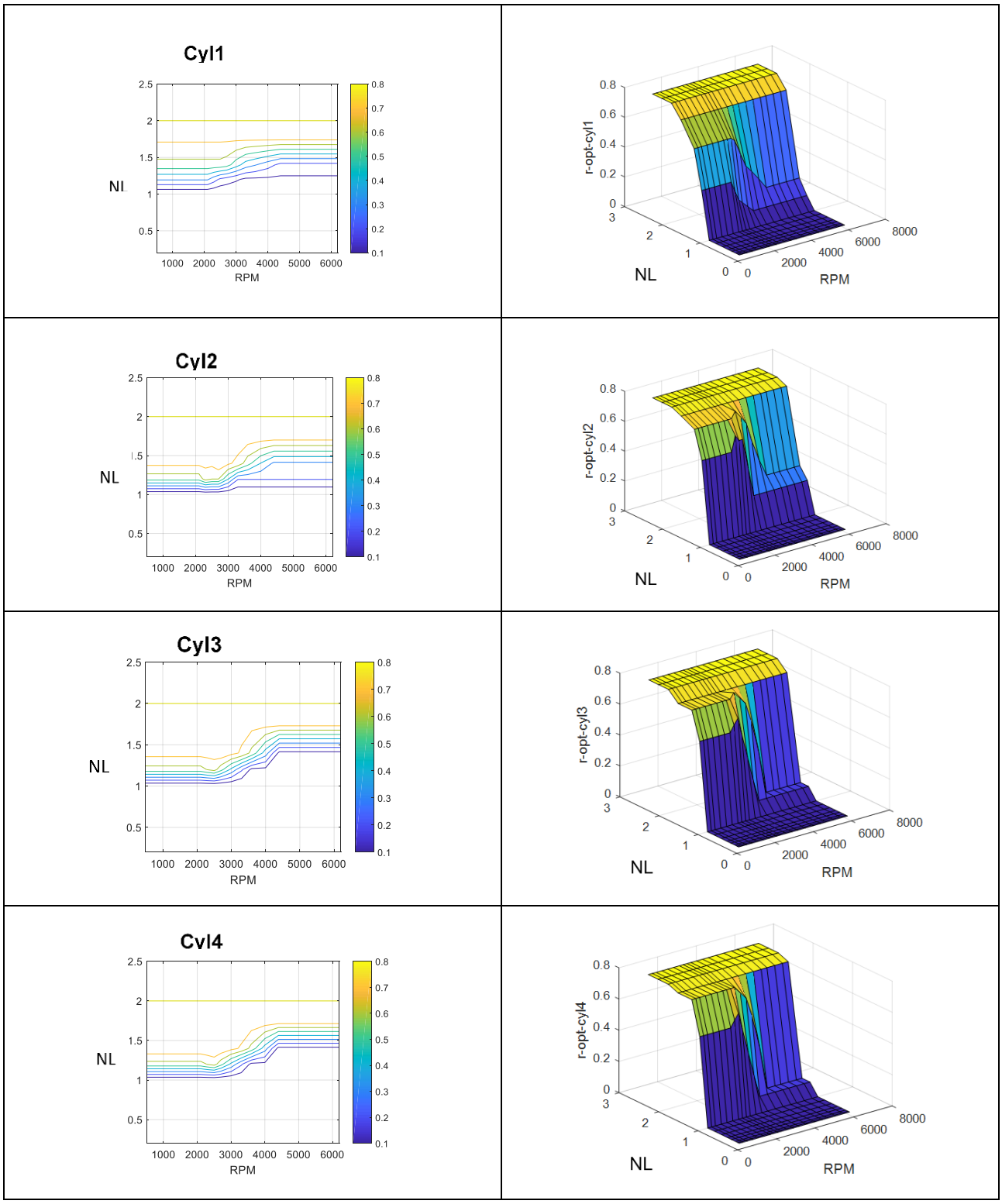

Figure 5.7 Ultimate r Map employed in the control system

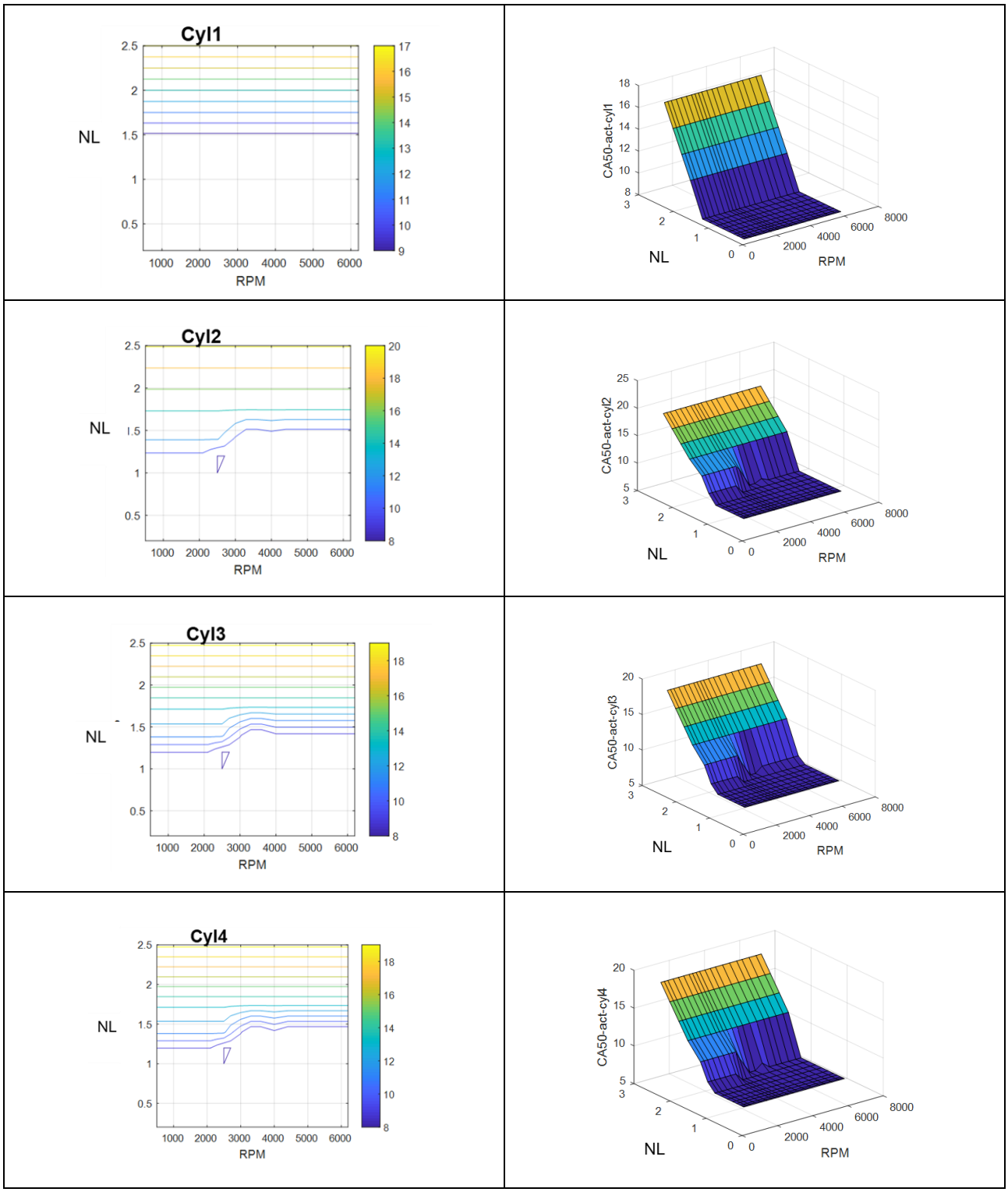

Figure 5.8 Ultimate MFB50 Map employed in the control system

Outside the operative field explored during the experimental campaign, the r map trend has been linearly extrapolated considering a maximum value of 0.8 and a minimum value of 0. After having defined the *r* value to apply on a wider operative field, the MFB50 target map has been prepared. Using a GT model (described in Chapter 6) the function of $MAPO98_{opt}$ is obtained considering the relative target of *r* for all

the points within the map operative field. Then the SA_{opt} value and the related MFB50 angle are computed for each point completing the MFB50 target map. The resulting surfaces are shown in Figure 5.7 and Figure 5.8.

5.2 Closed Loop Management on Knock Intensity

The controller is also composed by a CL contribution. The first version of such closed-loop controller manages the MAPO98, computed from MAPO measured cycle by cycle via in-cylinder pressure signal, by applying corrections to r and SA outputs. Basically, the implemented algorithm is based on a Proportional and Integral (PI) control system, which has been evolved to freely split the entire correction between the two levers on which the controller can act. The error between the measured MAPO98 and the corresponding threshold is translated into a proportional and integral correction through a gain scheduling PI structure. The resulting sum of two contributions is then converted in a percentage value which represents the total amount of the correction (Total Percentage Correction, TPC) which is required by the system for that specific operating condition. Such correction is then converted into r and SA variations, with a pre-defined logic. In this way, the TPC allows also to define a common reference to manage the two available actuators to control knocking events. When a r correction is applied, the OL chain compensates the final r value with the SA calculated by the Combustion Model, since the r correction is considered as input to such model. If the water-to-fuel ratio (r) reaches its saturation value (arbitrarily defined), to further reduce knocking a SA correction is also applied by the CL controller. Complete controller scheme is shown in Figure 5.9

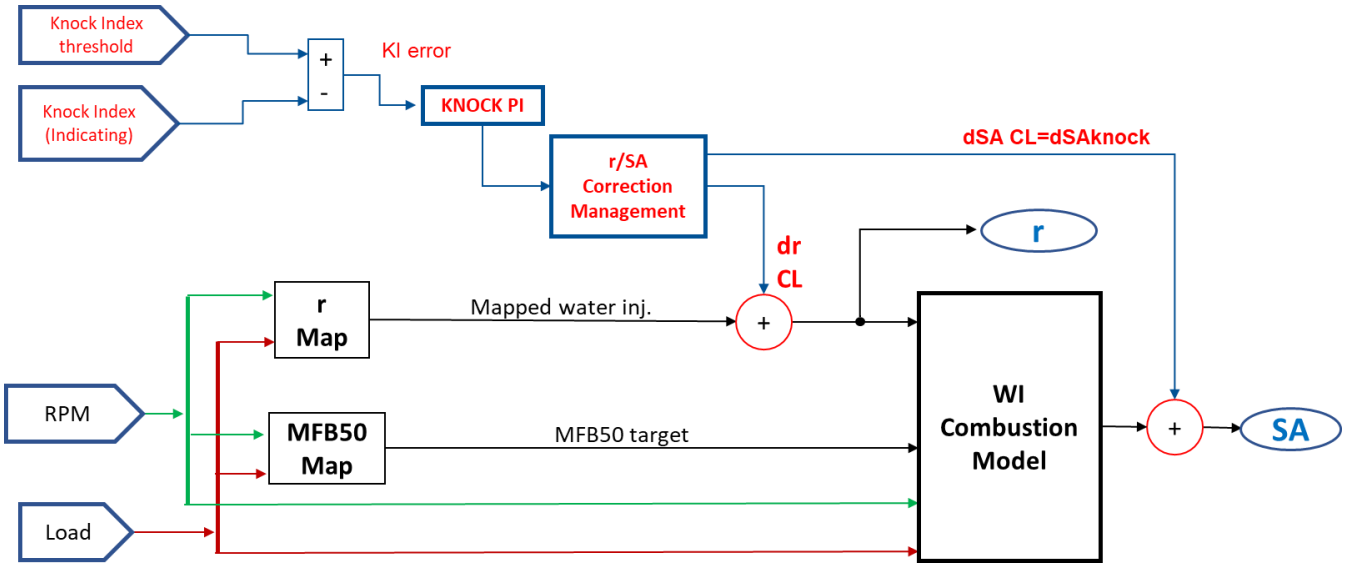

Figure 5.9 WI Controller: OL on MFB50 CL on Knock

5.2.1 *r*/SA Correction Management

The controller management of r and SA correction processes the TPC and the aim of this system consists in a correction of water injected to maintain the knock index on threshold value. At the same time, the combustion phasing can be guaranteed by the contribution of the model. This approach allows phasing and knock tendency to be independently managed. In fact, every correction applied on *r* is compensated by the model that corrects the SA instantaneously in OL, to obtain the MFB50 target. In this way, even if applied *r* is constantly modified by knock CL, the phasing control system is not affected by delay and error related to PI.

As mentioned before, the mitigation effect provided by water injection becomes ineffective over a certain *r* value. This is due generally to the fact that combustion becomes too much diluted and unstable, and further increment of water-fuel ratio can be dangerous for the integrity of the engine components. Therefore, as the *r* Map features a saturation over 0.8, also the *r* correction is limited to a maximum value. When the saturation value is reached, the control system reaches the maximum benefit achievable from the WI and the only way to mitigate knock is sacrificing efficiency, for this reason the *r*/SA Management switches to a new strategy. Instead of maintaining the MFB50 target by correcting *r*, this time the controller must keep the maximum value *r* while the knock is managed by moving the MFB50 thanks to the SA CL branch (dSAknock). Thus, the overall strategy can be summarized in 2 cases:

1. Low requested Knock PI TPC (black arrow in Figure 5.10):
    - *r* = *r* target + drCL
    - SA= SA Model (by MFB50 target)
2. High requested Knock PI TPC (red arrow in Figure 5.10):
    - *r* = *r* target + drCL (saturated value)
    - SA=SA Model + dSAknock

An interesting additional advantage of this approach is the possibility to optimize the water consumption since in case of excessive water injection (knock index below threshold) the controller can adjust the waste by reducing the *r* value. This leads to a reduction of overall water consumption.

In Figure 5.11 a representation of *r*/SA Management lay-out is displayed. The knock PI consists in a gain scheduling to produce the Total Percentage Correction. The TPC becomes the common input for a *r*-SA split system. The split is performed using two 2-D maps to manage separately d*r*CL and dSAknock. There is also a dynamic low threshold as fast correction for critical single knock events (MAPOcc). This block can quickly

force the TPC to the highest value by changing the response from case 1 to case 2 in order to stimulate a fast reaction to face the abnormal knock event.

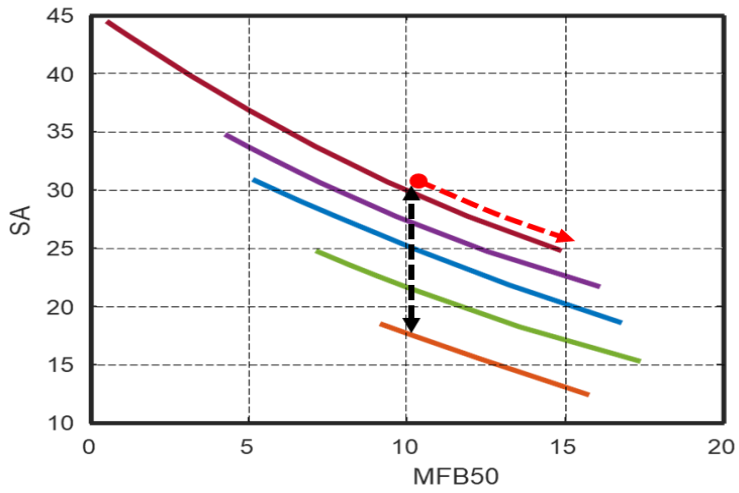

Figure 5.10 r/SA Management

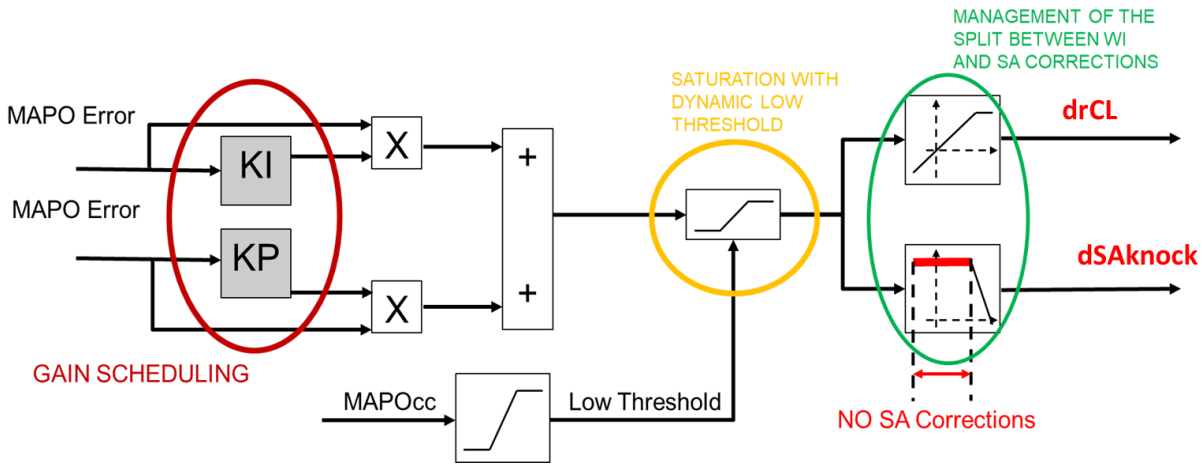

Figure 5.11 r/SA Management lay-out

5.3 Closed Loop Management on Knock Index and MFB50

The CL chain has been further developed and it has been integrated with an algorithm that evaluates the SA corrections needed to respect the MFB50 target. In other words, the second version of the Closed Loop branch can calculate the SA variations also to reduce the error between the measured MFB50 (obtained from in-cylinder pressure signal) and the target one, which is the output of the map implemented within the OL chain.

The MFB50 values are filtered with a moving average, to avoid the signal oscillations caused by the Cycle-to Cycle Variation (CCV) and to prevent a consequent unstable controller behaviour. The idea is to create a second TPC related to MFB50 error (MFB50TPC), which defines the SA correction only when the engine works in not-knocking or light-knocking conditions. In particular, the MFB50TPC cannot be increased when the TPC related to the MAPO98 error is over the level which activates SA correction for knock mitigation. The complete layout of the second version of the Water Injection based Combustion Control is shown in Figure 5.12.

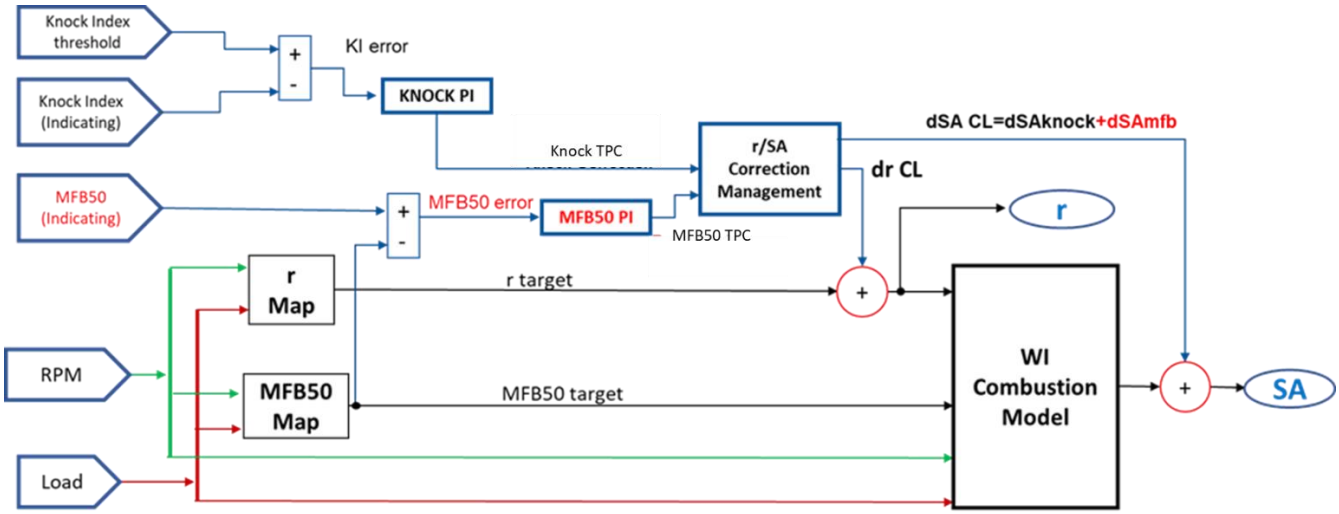

Figure 5.12 WI Controller: CL on MFB50 CL on Knock

The strategy of this new version of *r*/SA Management is displayed in Figure 5.13.

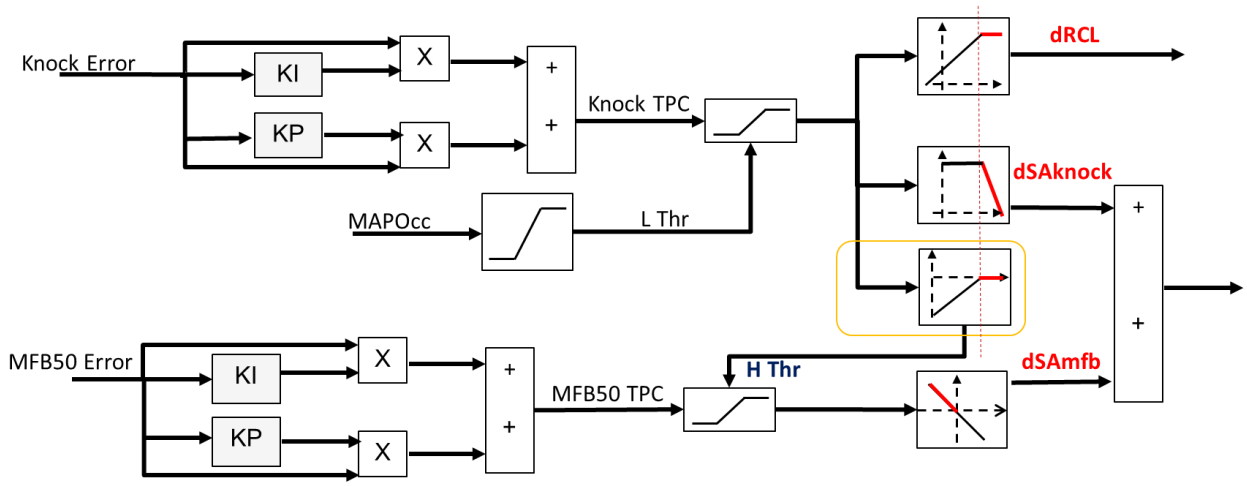

Figure 5.13 r/SA Management lay-out

With such approach the final SA correction is always a sum of two contributions. For this reason, a hierarchy between dSAknock and dSAmfb must be defined. The solution adopted is shown in Figure 5.13. When the knock TPC is increasingly close to the threshold which discriminates between acceptable and not-acceptable

knock level, the minimum MFB50TPC is progressively forced to 0. So, with an appropriate calibration of the vector that defines the SA correction with respect to MFB50TPC, it is then possible to have two controllers that act corrections on spark advance (the first based on MAPO98 error and the second on MFB50 error) without conflicts.

The new *r*/SA Management strategy can be summarized as seen before:

1. Low requested Knock PI TPC:
    a. *r* = *r* target + drCL
    b. SA= SA Model (by MFB50 target) + dSAmfb
2. High requested Knock PI TPC:
    a. *r* = *r* target + drCL (saturated value)
    b. SA=SA Model + dSAknock + dSAmfb (only if <0)

The hierarchy avoids the conflicts between dSAmfb and dSAknock but it can have an effect on the integral branch of PI when the correction is forced to move towards 0. In fact, if during the transition from low requested knock TPC to high knock TPC the correction is limited downstream of PI block, the integral part will raise and MFB50 TPC will reach to maximum value. Therefore, when the knock tendency (and also knock TPC) decreases the system can be unstable if the dSAmfb is restored too quickly because of the too advanced value of final SA. For this reason, the hierarchy has been designed without a simple step between the case 1 and 2, but features a slope to gradually lead the actual dSAmfb from original value to the saturated one.

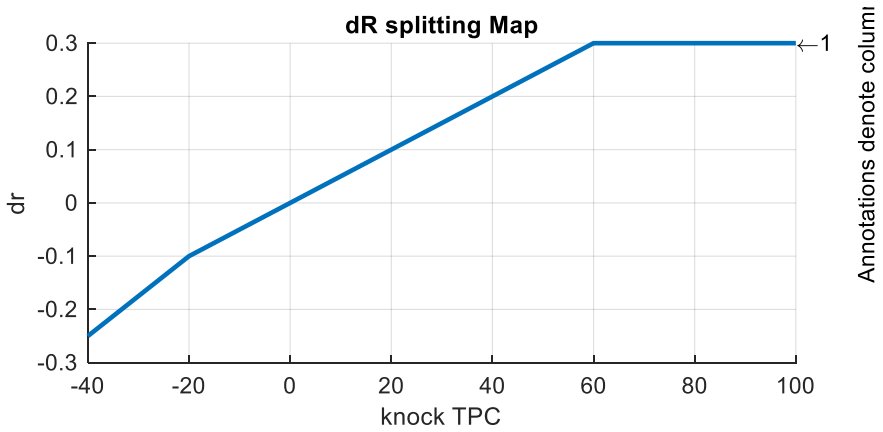

Figure 5.14

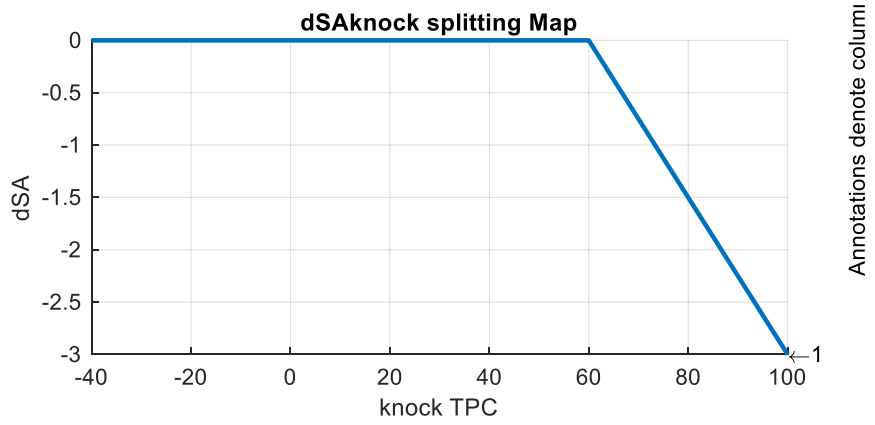

Figure 5.15

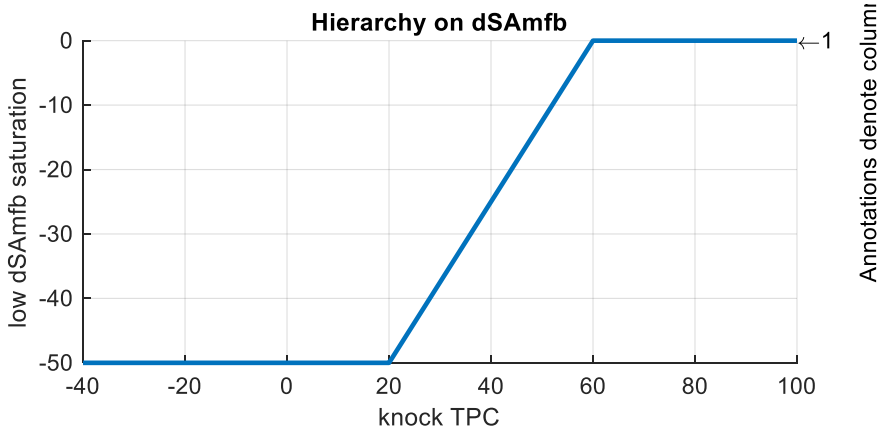

Figure 5.16

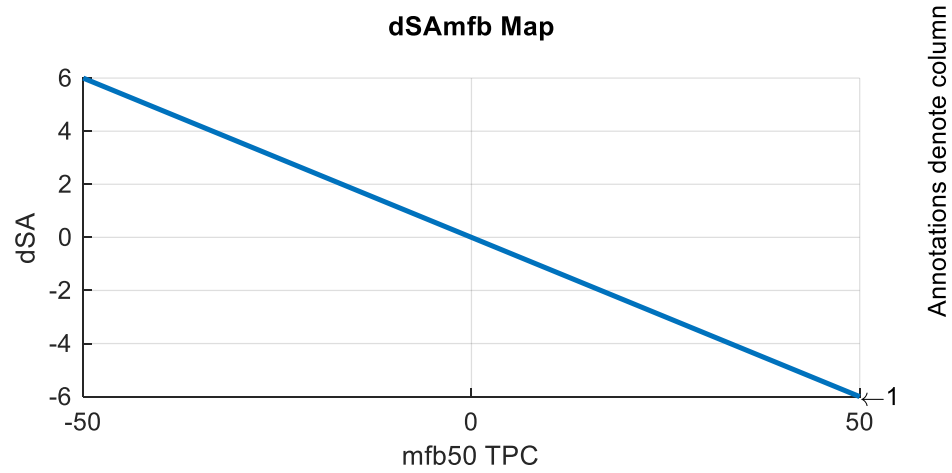

Figure 5.17

In a next configuration, this strategy has been simplified. Instead of featuring a hierarchy, all the dSAmfb branch, including the PI computation, can be frozen when knock TPC switches from case 1 to case 2 and can

be released in the opposite condition. In this way, the mfb50 TPC won't produce the instability described before.

In Figure 5.18 the Simulink lay-out of this new version is shown. The red line represents the knock TPC. This signal goes to both (d*r*, dSA) splitting blocks. At the same time, the signal goes to 2 switch blocks: one forces the integral step to be null and the other repeats in memory loop the value of dSAknock. Both blocks switch at value 60 of knock TPC, the same threshold that defines the transient between low and high knock correction.

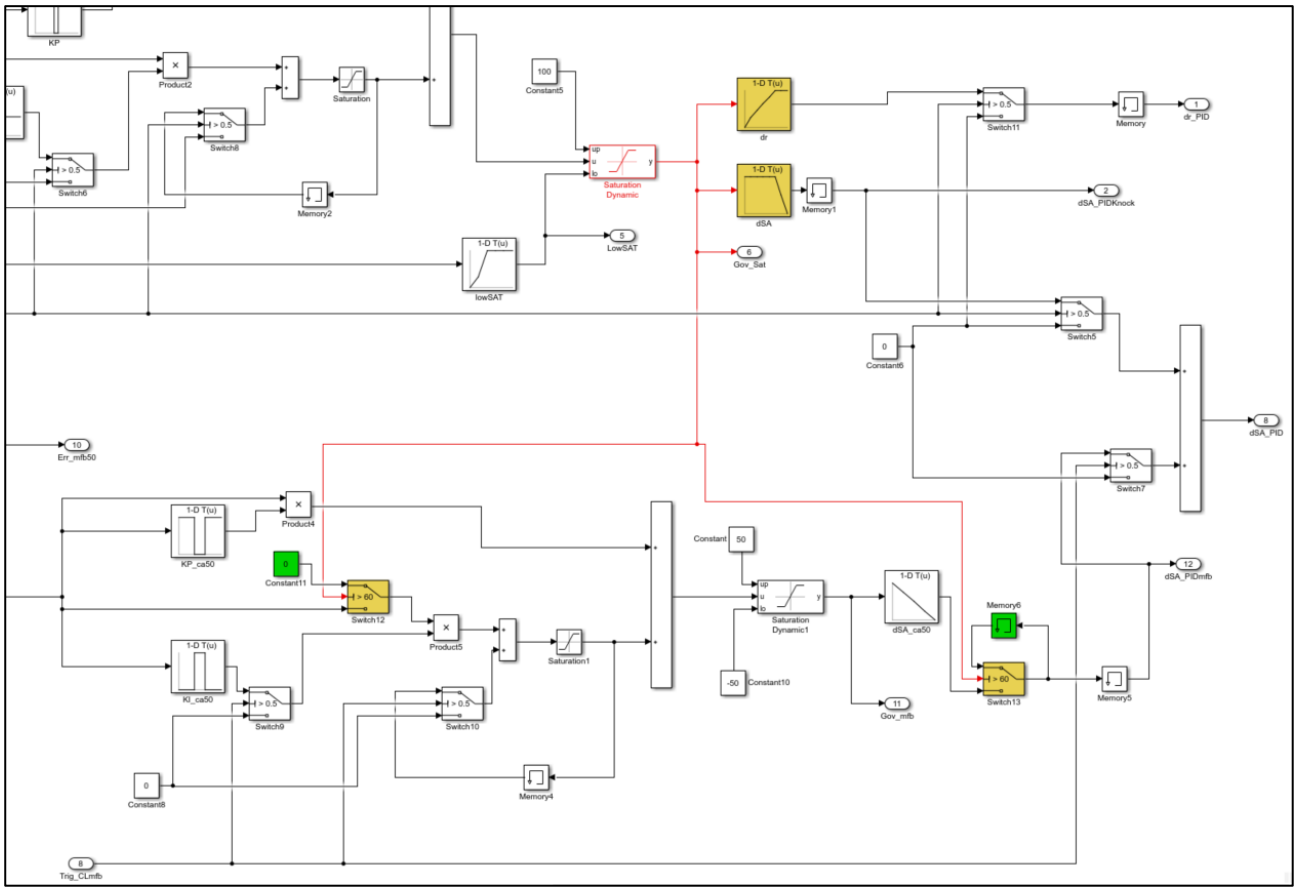

Figure 5.18Partial Simulink lay-out of the last version of WICC.

6 Software in the Loop

Two versions of the WICC, the first featuring MFB50 Open Loop and Knock Closed Loop and the second one featuring both MFB50 and knock Closed Loop, have been tested and validated via Software in the Loop (SiL) simulations. As reported in [27], the controller has been coupled with a mono-dimensional mean-cylinder engine simulator which includes the WI, the CCV and a knock model as shown in Figure 6.1. Such simulator consists in a GT Power model of the experimental setup, in which the combustion model has been calibrated via Three Pressure Analysis (TPA). The GT model has been also converted in a Fast Running Model (FRM), to test the controller in Real-Time (RT). Nine different engine points have been simulated, covering almost the entire boosted operating field. Of course, the lowest loads points have been neglected, because of the absence of knocking events and the consequent controller inactivity. The quality of the simulations results is defined through the R-squared index. Moreover, the simulations with the first version of the controller (the one with the CL only on the knock intensity), are also a validation of the reliability of the Combustion Model, because the accuracy on the MFB50 target is ensured only by the OL chain.

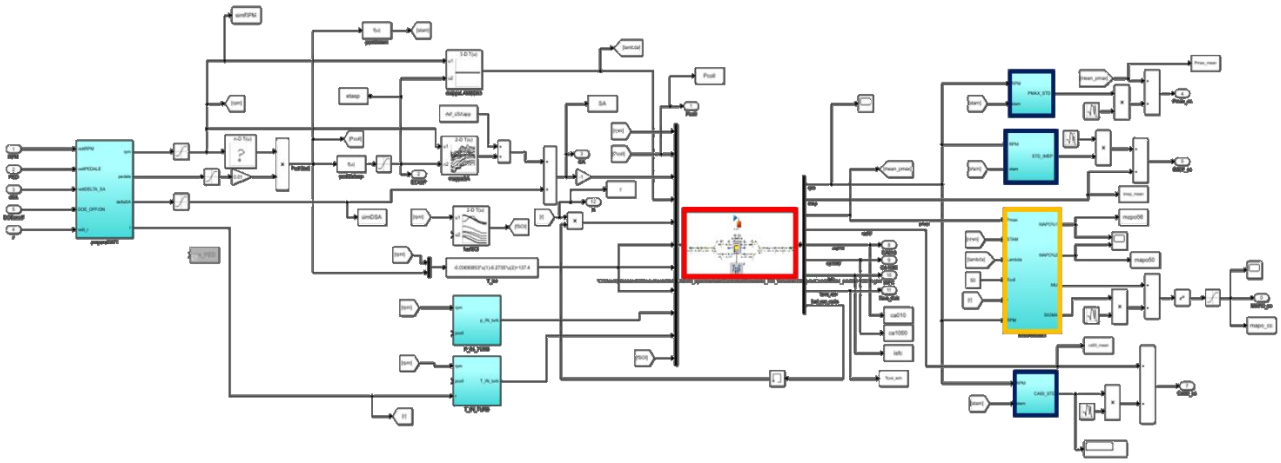

Figure 6.1 Simulink Lay out of Engine Model. The GT Power model of the mean cylinder has been highlighted in red and the knock models has been highlighted in yellow.

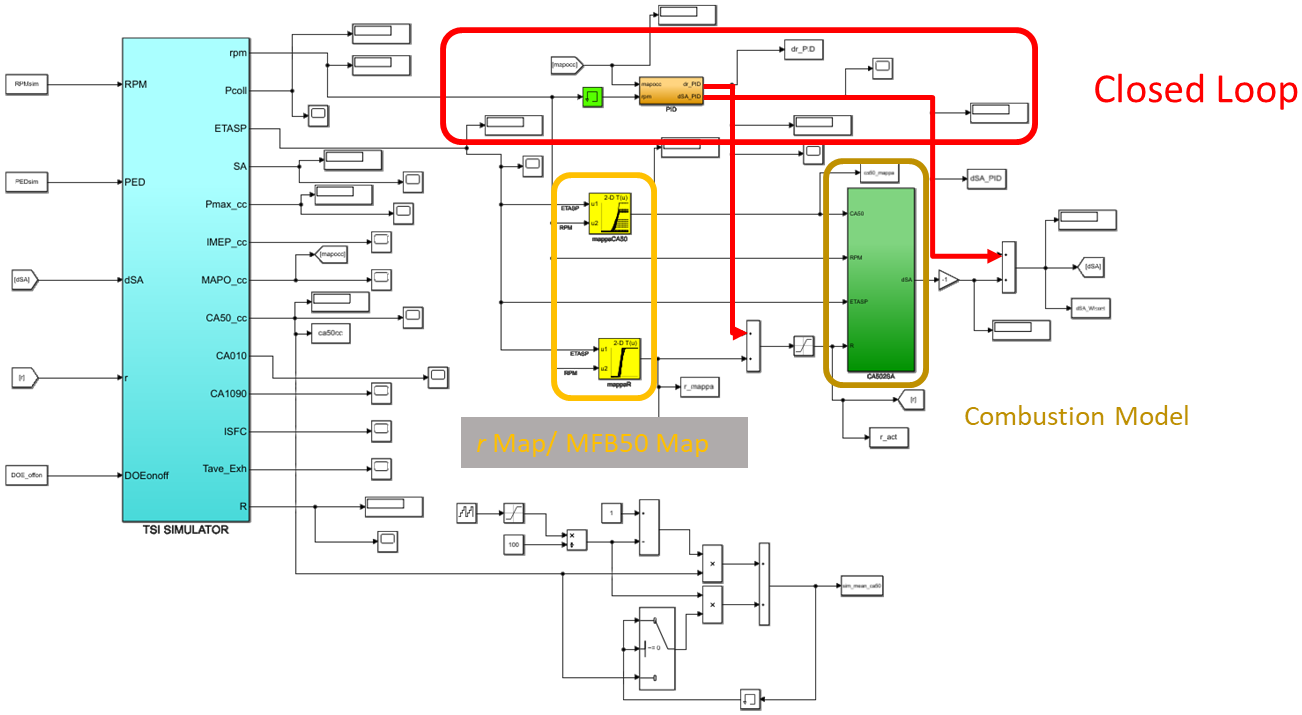

Figure 6.2 TSI Simulator (blue block) coupled with WICC, Simulink code.

6.1 Fast Running GT Power Model

The GT Power model of the TSI engine has been converted in a Fast Running Model. This procedure consists in the reduction of engine model complexity, mainly through the combination of single ducts in parts with larger volumes. On the contrary, the combustion model and the intake and exhaust valves and ports are not modified, and this allows to maintain the predictive capabilities of the detailed model. While the accuracy of some ducts signals (like pressure and flow rate waves) is partially lost, the entire conversion process can be driven by the tolerance (imposed by the user) that has to be maintained for some combustion indexes (like maximum in-cylinder pressure, MFB50, etc.). In this way, the detailed model can be easily adapted for RT simulations. Also, the WI modelling has been modified to be in accordance with the new ducts configuration.

As accurately described in [21] the WI system has been modelled with two injectors, where the first is a Port Water Injector (PWI) and the second is a Direct Water Injector (DWI). Through the calibration of parameters that define how the injected water mass is split between such injectors, the water vapor quantity and the angular duration of in-cylinder water evaporation can be correctly reproduced. Also, the WI modelling has been modified to be in accordance with the new ducts configuration.

6.2 Calibration by Simulated data

The modelling of the engine coupled with a simulation of CCV and knock led to the possibility to obtain quickly more data, simulating several operative points in the same field used during experimental campaign. These simulated data have been used to perform a more precise calibration of the combustion model. Adopting the same approach described in Chapter 4 for each point, the three parabolic coefficients (a,b,c) that define the model have been computed. As shown in Figure 6.3, each parameter can be fitted with a surface on RPM and load domain in the same way as the experimental data. Furthermore, in Figure 6.4 it can be seen in which way the water-fuel ratio modifies the surface of one parameter (a) in a more effective way.

Using this simulated database, the combustion model has been calibrated again to perform the software in the loop process. During the process, a first attempt calibration has been carried out for the gain scheduling and management of TPC (for knock and mfb) by dr Map, dSAknock Map, dSAmfb and its hierarchy.

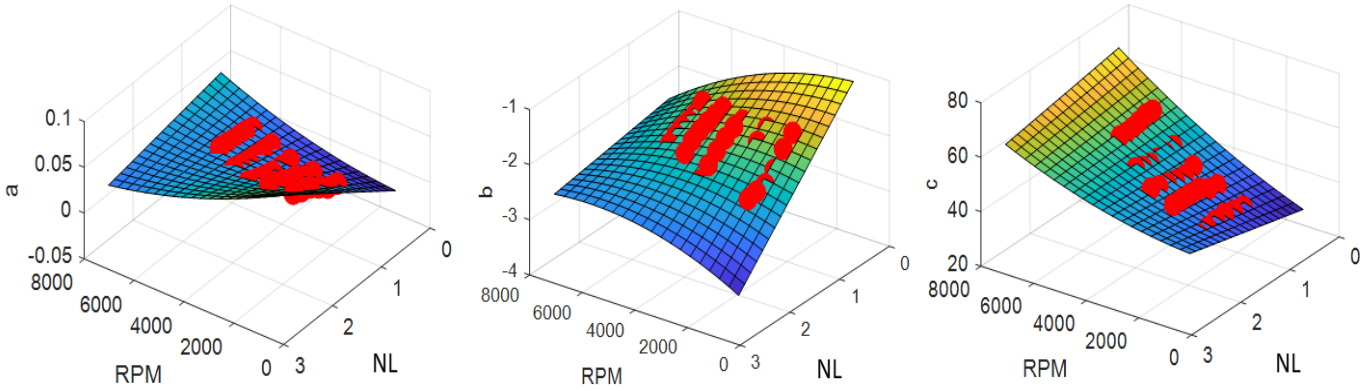

Figure 6.3 Simulated parabolic parameters a, b, c for r=0, provided by simulation

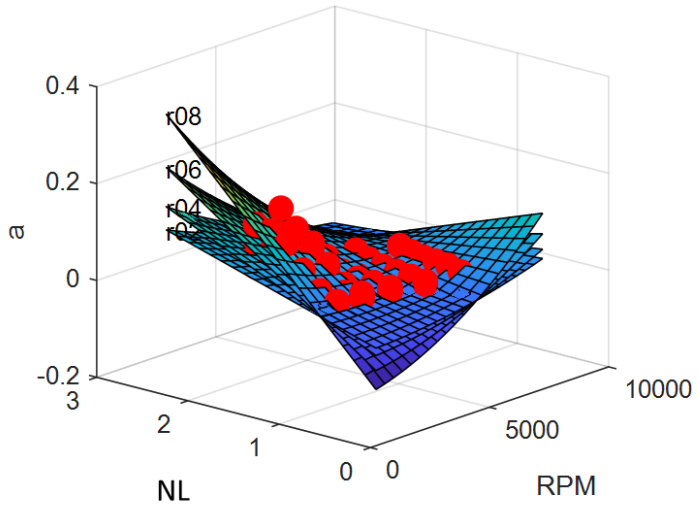

Figure 6.4 Simulated parabolic parameter a at different r values, provided by simulation

6.3 Simulation Results

The FRM has been appropriately compiled and it has been consequently implemented in a 0-D co-simulation environment. The first simulations allow the best calibration parameters set for the CL controller to be identified. They have been carried out for different engine points, in steady state and in transient conditions. During such simulations the PI controller applies r corrections that are then added to the map value, and CL contribution is not saturated above a specific value. This means the final r can assume too high values. Of course, this is not representative of a real application, in which the maximum r is certainly much lower, but such strategy allows studying the PI behaviour on r and SA corrections also for high load conditions. It is important to accurately calibrate the CL parameters on the entire operating field. In Figure 6.5, Figure 6.6, Figure 6.7, and Figure 6.8, the results of simulations with the first version of the Water Injection based Combustion Control (characterized by the CL on MAPO98) are collected, for two different engine points.

In Figure 6.6 and Figure 6.7 it has been simulated a medium NL condition and the CL works only with r corrections. In Figure 6.8 a high load engine point has been simulated and during the firsts 50 cycles it is possible to highlight the protection action with a SA decrement, due to a high MAPO cycle. For small errors on MAPO98 the PI manages the water mass and for high errors it introduces also SA variations. The r corrections can have also a negative sign, to reduce the mapped water mass when the recorded MAPO98 is lower than the threshold (Figure 6.5). The CL parameters set has been chosen to guarantee a good correction stability and, at the same time, fast responses during transients. Figure 6.9 shows a transient simulation and during the rising ramp the CL is able to manage the knock intensity only with r corrections. In first four figures the error between the mean MFB50 and the map value (the target) is due to inaccuracies of the Water Injection based Combustion Model used in the open-loop controller, which are quantified with the Root

Mean Squared Error. Table 6-1 collects the RMSE of the controller on the MFB50 and MAPO98 targets for each simulation, because they represent the indexes that allow to quantify the controller robustness. The errors are evaluated excluding the firsts cycles, due to the MAPO98 and MFB50 buffers which are filling and do not produce coherent values.

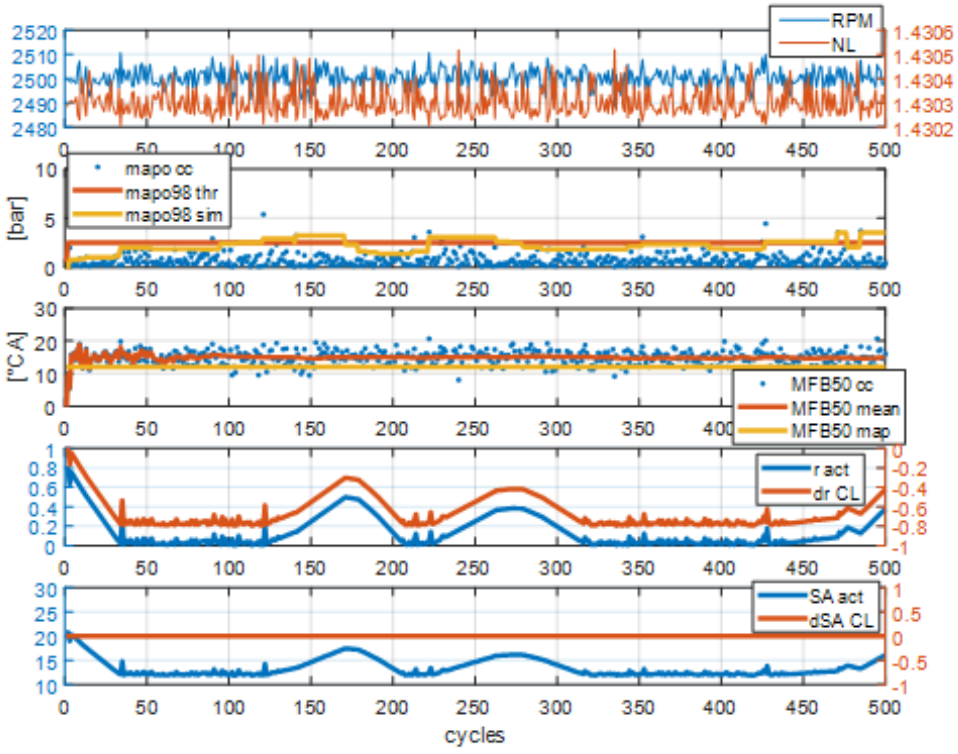

Figure 6.5 Steady state simulation results for engine point 2500 RPM, NL 1.43. Five subplots show (from top to bottom): RPM-NL, cycle-to-cycle recorded MAPO, MAPO98 and the MAPO98 threshold, cycle-to-cycle recorded MFB50, mean MFB50 and the corresponding target, the actuated r and the r correction calculated by CL chain, the actuated SA and the SA correction calculated by the CL chain.

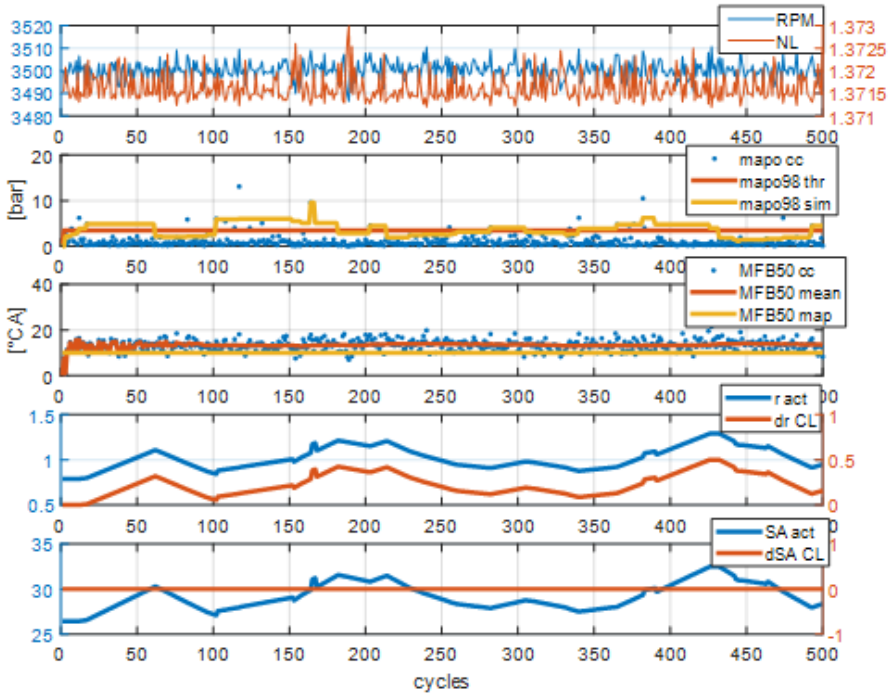

Figure 6.6 Steady state simulation results for engine point 3500 RPM, NL 1.37. Five subplots show (from top to bottom): RPM-NL cycle-to-cycle recorded MAPO, MAPO98 and the MAPO98 threshold, cycle-to-cycle recorded MFB50, mean MFB50 and the corresponding target, the actuated r and the r correction calculated by CL chain, the actuated SA and the SA correction calculated by the CL chain.

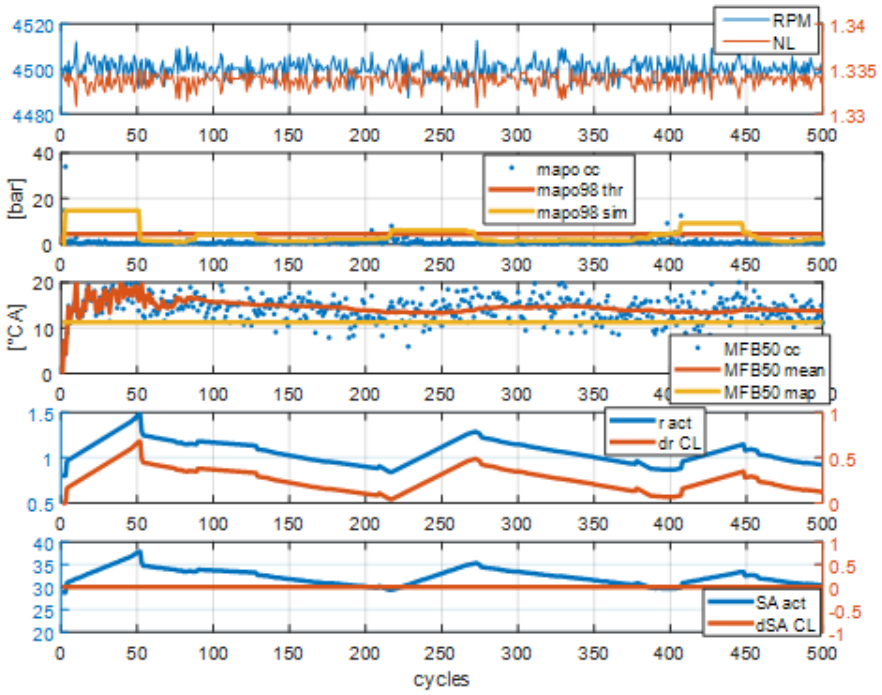

Figure 6.7 Steady state simulation results for engine point 4500 RPM, NL 1.33. Five subplots show (from top to bottom): RPM-NL, cycle-to-cycle recorded MAPO, MAPO98 and the MAPO98 threshold, cycle-to-cycle recorded MFB50, mean MFB50and the corresponding target, the actuated r and the r correction calculated by CL chain, the actuated SA and the SA correction calculated by the CL chain.

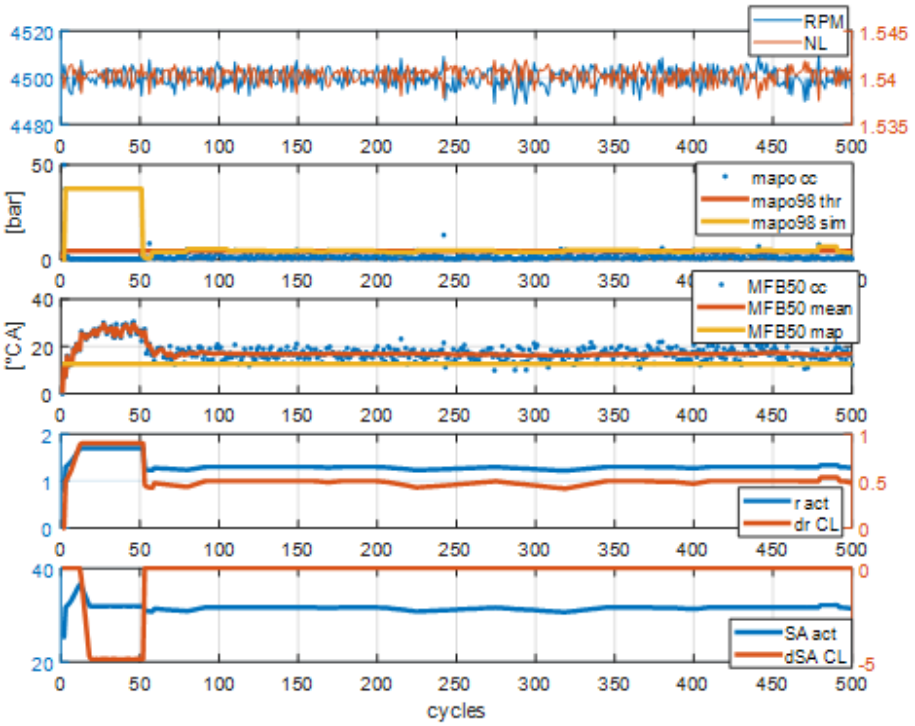

Figure 6.8 . Steady state simulation results for engine point 4500 RPM, NL 1.54. Five subplots show (from top to bottom): RPM-NL cycle-to-cycle recorded MAPO, MAPO98 and the MAPO98 threshold, cycle-to-cycle recorded MFB50, mean MFB50 and the corresponding target, the actuated r and the r correction calculated by CL chain, the actuated SA and the SA correction calculated by the CL chain.

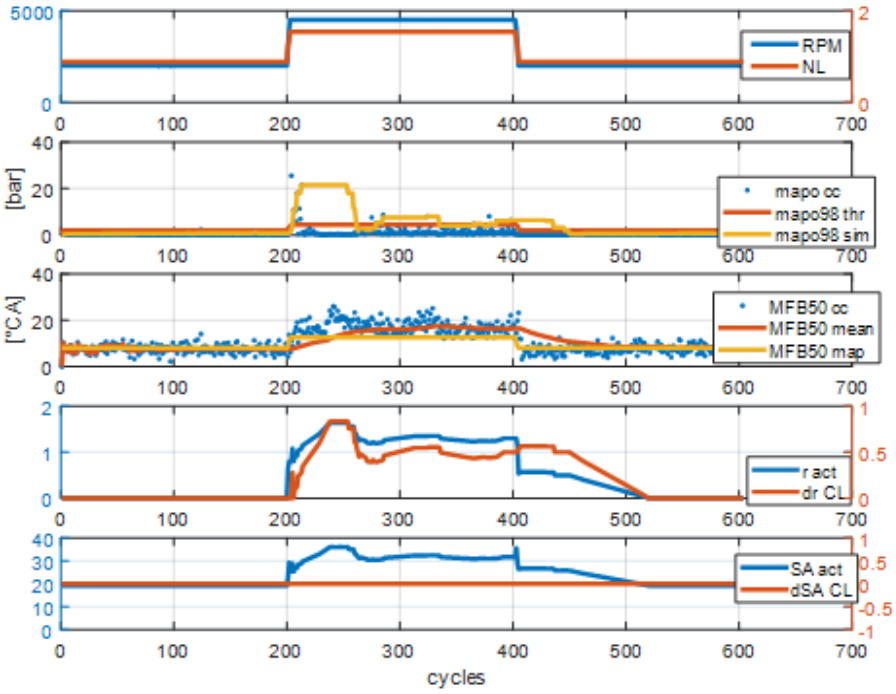

Figure 6.9 Transient simulation results. Five subplots show (from top to bottom): RPM-NL, cycle-to-cycle recorded MAPO, MAPO98 and the MAPO98 threshold, cycle-to-cycle recorded MFB50, mean MFB50and the corresponding target, the actuated r and the r correction calculated by CL chain, the actuated SA and the SA correction calculated by the CL chain.

Table 6-1 Root Mean Squared Errors for the validation simulations with the first version of the WI based Combustion Control. The mean value of the RMSE on mean (by moving average) MFB50 represents the accuracy of the Combustion Model.

Engine Point	RMSE MFB50 [°CA]	RMSE MAPO98 [bar]
RPM 2500 NL 1.43	1.81	0.55
RPM 3500 NL 1.37	2.55	1.24
RPM 4500 NL 1.33	2.10	0.63
RPM 4500 NL 1.54	1.61	0.81
RPM 2000-4500-2000 NL 0.8-1.7-0.8	1.75	4.02
Mean	1.96	1.45

Results of simulations with the second version of WICC (characterized by CL on MAPO98 and MFB50 target) are shown in Figure 6.10, Figure 6.11, Figure 6.12 and Figure 6.13. The CL on MAPO98 parameters values does not change, but during these simulations the final SA correction is the sum of two contributions (from MAPO98 and MFB50 CL controllers). The positive SA corrections are accepted only when the TPC is under a predetermined value. In Figure 6.12 it is possible to highlight negative and quick SA corrections in correspondence with a cycle characterized by a high MAPO level. In fact, in such simulation, the high MAPO value produces a high lower saturation of TPC, which is translated in an upper saturation of MFB50TPC to manage measured knock levels. This system avoids also on-off CL responses. In both figures it can be clearly seen that the MFB50 target is reached by the control system, thanks to the closed loop corrections evaluated by the MFB50 CL controller.

Figure 6.14 shows the transient simulation results during which the controller is able to maintain the mean MFB50 on the corresponding target. The CL calibration parameters have been set on values which guarantees fast responses of the controller to have quite fast responses also in few simulated cycles, at the expense of the best stability. The Table 5 collects the RMSE for all simulations. The values highlight the reduction of the error on the MFB50 target.

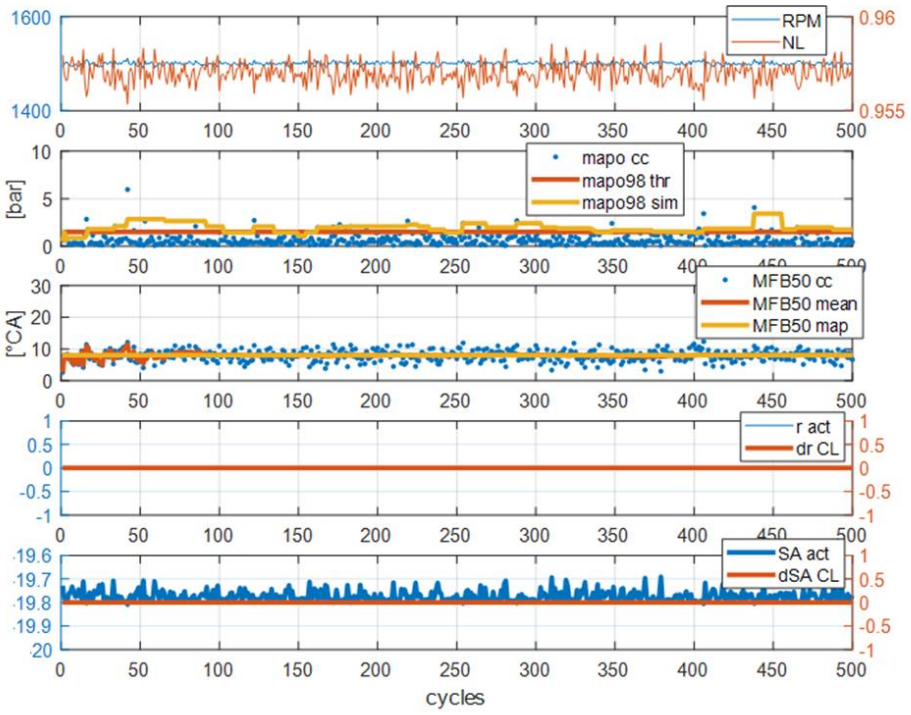

Figure 6.10 Steady state simulation results for engine point 1500 RPM, NL 0.95 with the CL on MFB50. Five subplots show (from top to bottom): cycle-to-cycle recorded MAPO, MAPO98 and the MAPO98 threshold, cycle-to-cycle recorded MFB50, mean MFB50 and the corresponding target, the actuated r and the r correction calculated by CL chain, the actuated SA and the SA correction calculated by the CL chain.

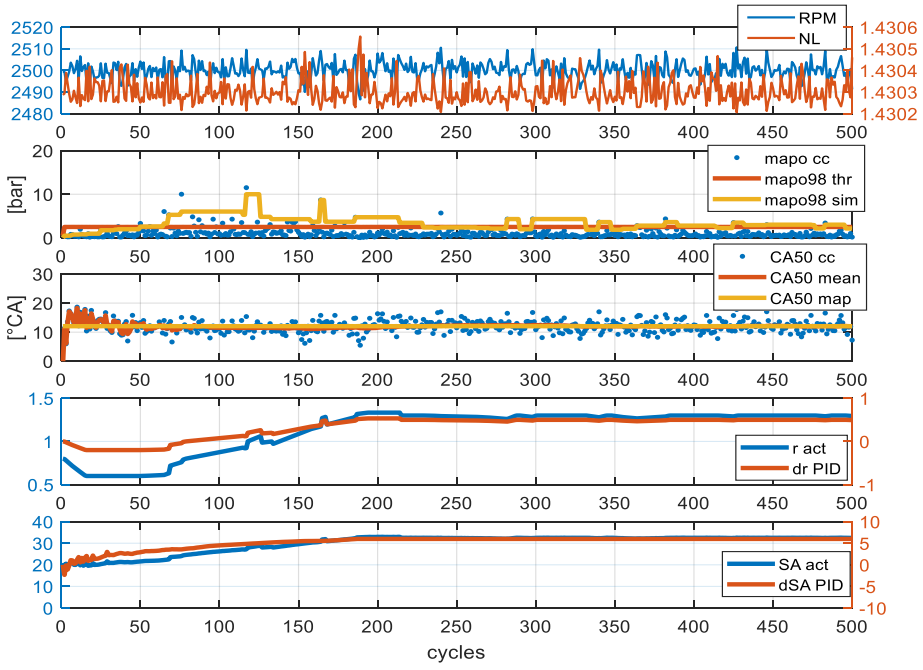

Figure 6.11 Steady state simulation results for engine point 2500 RPM, NL 1.43 with the CL on MFB50. Five subplots show (from top to bottom): cycle-to-cycle recorded MAPO, MAPO98 and the MAPO98 threshold, cycle-to-cycle recorded MFB50, mean MFB50and the corresponding target, the actuated r and the r correction calculated by CL chain, the actuated SA and the SA correction calculated by the CL chain.

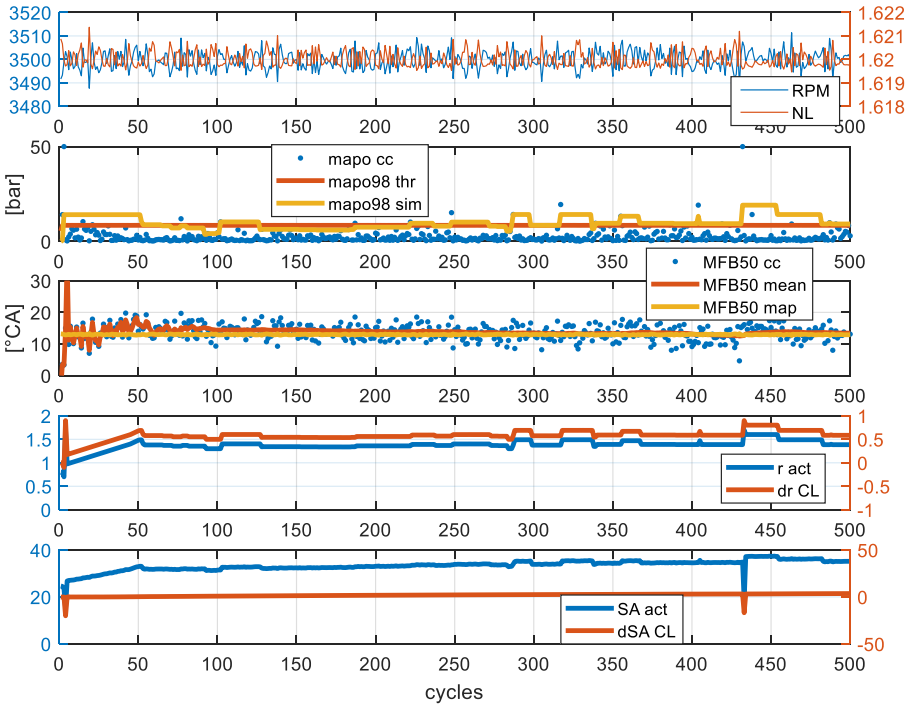

Figure 6.12. Steady state simulation results for engine point 3500 RPM, NL 1.62 with the CL on MFB50. Five subplots show (from top to bottom): RPM-NL, cycle-to-cycle recorded MAPO, MAPO98 and the MAPO98 threshold, cycle-to-cycle recorded MFB50, mean MFB50and the corresponding target, the actuated r and the r correction calculated by CL chain, the actuated SA and the SA correction calculated by the CL chain.

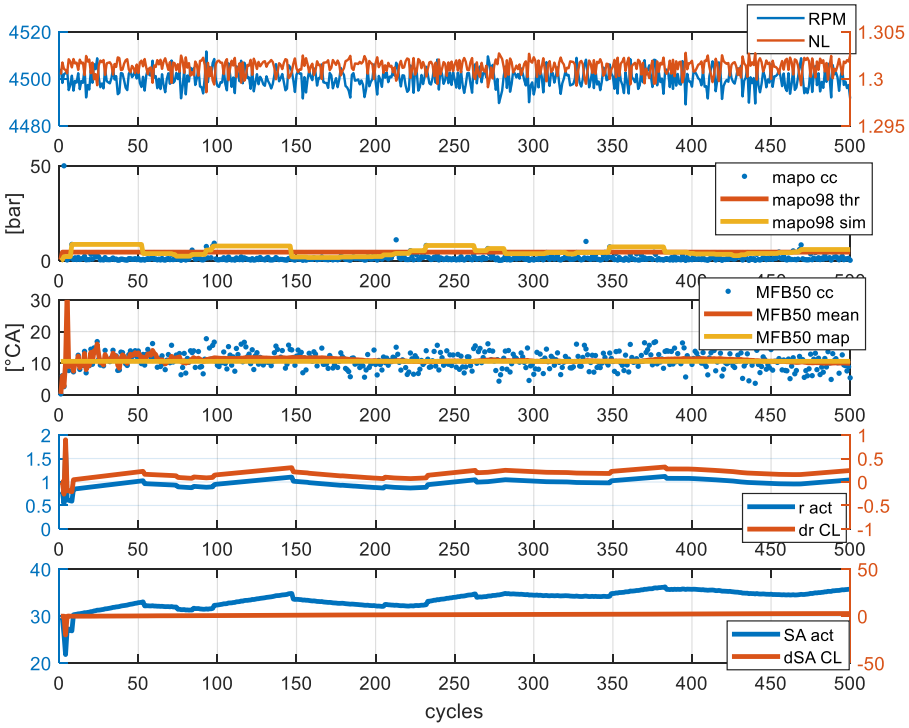

Figure 6.13. Steady state simulation results for engine point 4500 RPM, NL 1.3 with the CL on MFB50. Five subplots show (from top to bottom): RPM-NL cycle-to-cycle recorded MAPO, MAPO98 and the MAPO98 threshold, cycle-to-cycle recorded MFB50, mean MFB50

and the corresponding target, the actuated r and the r correction calculated by CL chain, the actuated SA and the SA correction calculated by the CL chain.

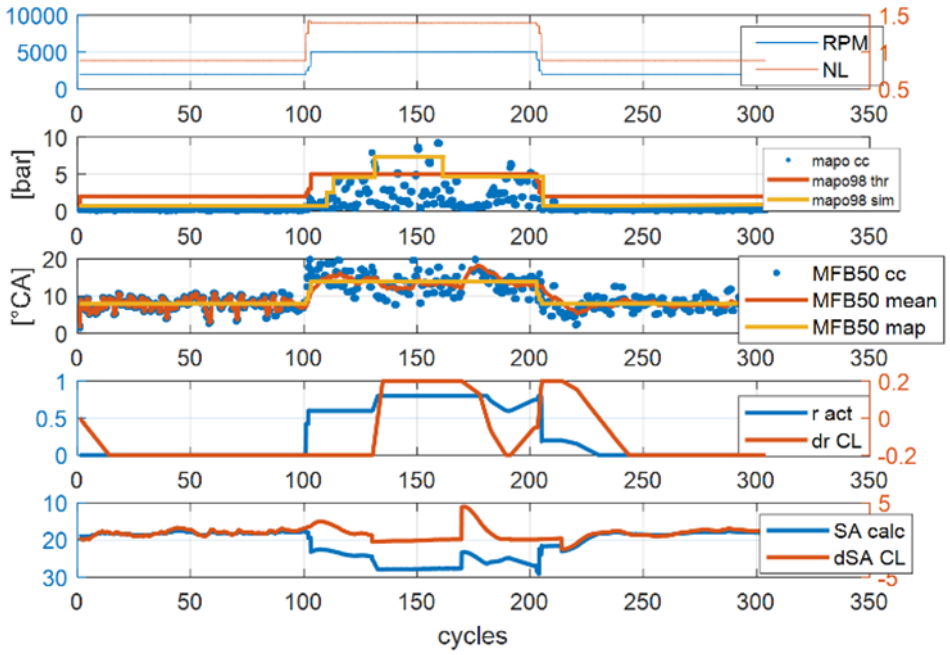

Figure 6.14. Steady state simulation results for engine point 4500 RPM, NL 1.3 with the CL on MFB50. Five subplots show (from top to bottom): RPM-NL cycle-to-cycle recorded MAPO, MAPO98 and the MAPO98 threshold, cycle-to-cycle recorded MFB50, mean MFB50 and the corresponding target, the actuated r and the r correction calculated by CL chain, the actuated SA and the SA correction calculated by the CL chain.

Table 6-2

Engine Point	RMSE MFB50 [°CA]	RMSE MAPO98 [bar]
RPM 1500 NL 0.957	0.17	0.87
RPM 2500 NL 1.43	0.32	1.89
RPM 3500 NL 1.62	0.62	1.04
RPM 4500 NL 1.3	0.45	0.93
RPM 2000-4500-2000 NL 0.88-1.49-0.88	0.88	2.34
Mean	0.49	1.41

7 Experimental Validation of WICC

The validation of WI Combustion Controller has been carried by evaluating step by step the performance of every part of the whole system. This evaluation has been possible through the evolution of the RCP system described in 2.1.3 The main findings have been reported in [24].

7.1 Open Loop on MFB50

At first, WICC has been tested disabling the entire r/SA Correction Management subsystem, to highlight the functioning of WI Combustion Model. In fact, in this configuration there are no corrections on r and SA and the controller works in total open loop.

As shown in Figure 7.1, the test is composed by two different stages. The first one (from second 10 to second 45) features steps of MFB50 target at a fixed value of r (Ract) of 0. For each step the model modifies the actuated SA (SAact) accordingly and can produce an actual MFB50 (MFB50 meas) close to the target within a range of 2 CA, even during transients. In the second stage (from second 45 to 75) the MFB50 target is set at a single value and steps of r are applied. In this case the model modifies SA to compensate the effect of water injection and the measured MFB50 remains close to the target. It is important to observe that the model's (OL) precision also varies depending on the value of r.

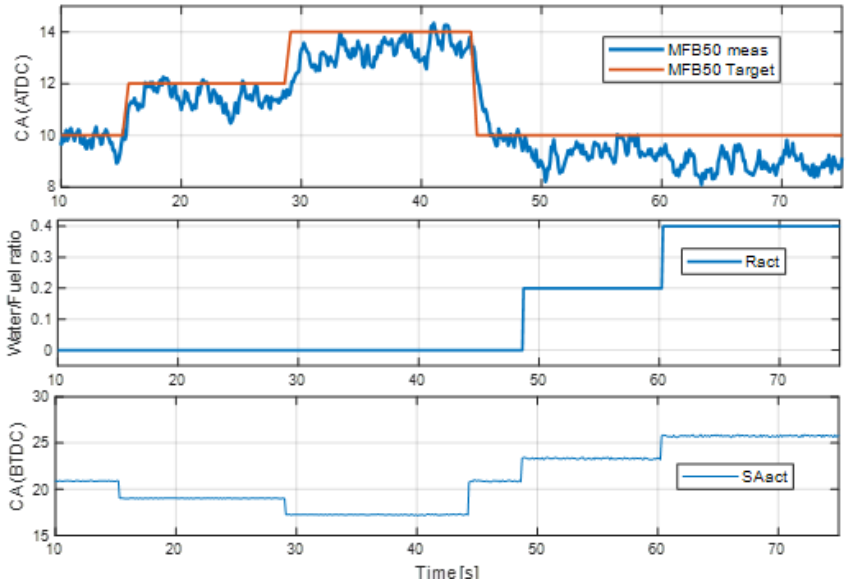

Figure 7.1 Steady state engine point 3300 RPM, 1.25 NL, Cylinder 2. On top has been displayed the match between MFB50 measured and MFB50 target, in the middle the value of r actuated, at the bottom the SA as model output to achieve the MFB50 target.

7.2 Closed Loop on MFB50

After the evaluation of the model performance, the CL on MFB50 branch has been tested. The procedure is similar to the previous one because the same steps of MFB50 target and r target are imposed, but this time at second 13.5 the MFB50 CL branch is activated as displayed in Figure 7.2. When the CL is activated, dSAmfb starts to apply correction on SA provided by model and SAact becomes the sum of these two terms. From this instant actual MFB50 is forced to correspond to the target value. The value of dSAmfb can also be used to evaluate the precision of the WI Combustion Model in defining SA. Closed-loop aids in correcting for the previously mentioned imprecisions of the model with increasing values of r.

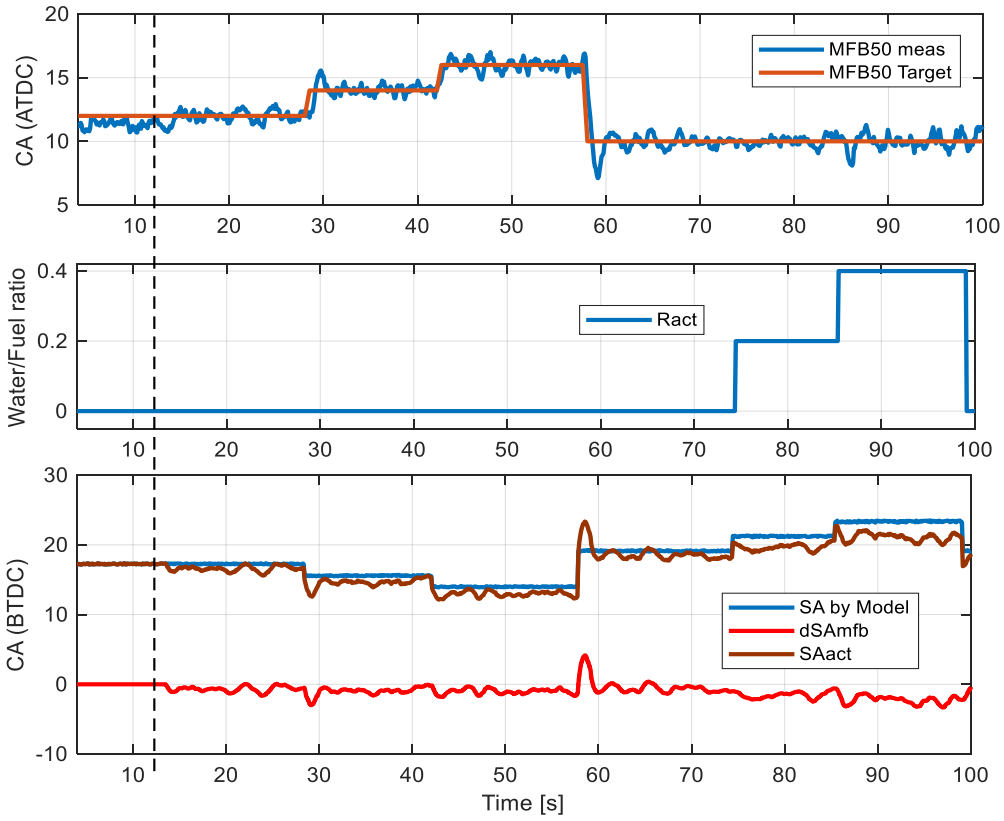

Figure 7.2 Steady state engine point 2800 RPM, 1.25 NL, Cylinder 2. At time 0 controller starts in open loop (as seen in Figure 9). After second 13.5 the controller switches in closed loop mode and the PI correction dSAmfb compensates the error on MFB50. SAact represents the sum of SAbyModel and dSAmfb.

7.3 Closed Loop on MFB50/Closed Loop on MAPO98

In the next three figures, the behaviour of the CL on r/SA Management is displayed. Two different situations are presented, one in which the correction of WI (dR PID) does not saturate (preestablished value of saturation of dR PID = 0.3) and two others in which it does.

MFB50meas corresponds to a moving average from cycle by cycle MFB50 measured angle while MFB50target is the value of the MFB50 Map. Ract and Rmap are the final r value actuated and r value obtained from the map, respectively. dR PID is the correction applied by the knock branch of the PID on actuated r, and dR PID sat is the previously mentioned saturation value imposed on the correction of r by the PID. SA act represents the finally actuated SA, that is composed of SAmodel (calculated by the model) and corrected by both dSAmfb and dSAknock which are the contributions of both closed loop branches. MAPOcc indicates the cycle by cycle value while MAPO98 and MAPO98thr are the calculated 98th percentile and its threshold value accordingly.

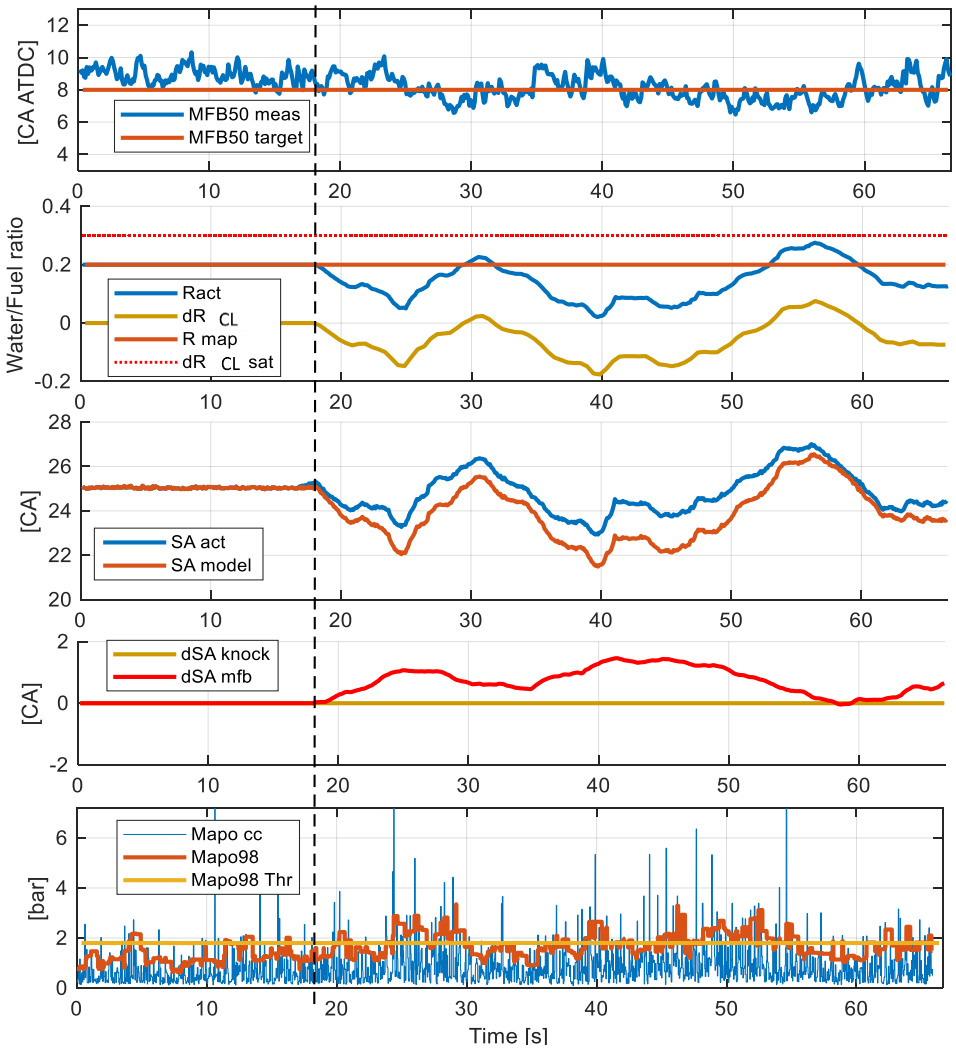

Figure 7.3 Steady state engine point 2700 RPM, 1.22 NL, Cylinder 1. At second 18 the controller switches from open loop to closed loop: dSAmfb starts to compensate SA model (as seen in Figure 10) and correction dR CL compensates R map (mapped value of r) to keep Mapo98 (knock Index) close to threshold (Mapo98 Thr).

Figure 7.3 and Figure 7.4 display a test (looking respectively to Cylinder 1 and Cylinder 3) in which the controller operates in complete open loop until second 18 (SA controlled solely by the model and WI only by the r obtained from the r MAP). At second 18 both CL branches (knock and MFB50) are activated. In the first

one it can be seen how shortly before activating CL, knock is generally under threshold and MFB50 is slightly retarded. The response of the knock branch is an initial negative dR PID correction (reducing amount of water injected to save water) while the MFB50 branch applies positive correction (dSAmfb) in order to get closer to the MFB50 target, given the previous slightly retarded OL response. From there on, both branches continue to keep both knock and MFB50 at target without saturating the dR PID. Values of dR PID keep the quantity of injected water close to the one set by the r MAP. The corrections given by both branches correspond only to the integral part, this is what gives the slow oscillating behaviour close to each respective target. SA calculated by the model follows the form of Ract since it considers the effects of r. In cylinder 3, the controller reacts in similar way but this time the actual MFB50 angle is slightly advanced. Therefore, the reaction at second 18 is directed in the opposite way, dSA mfb goes negative whereas dr CL goes positive.

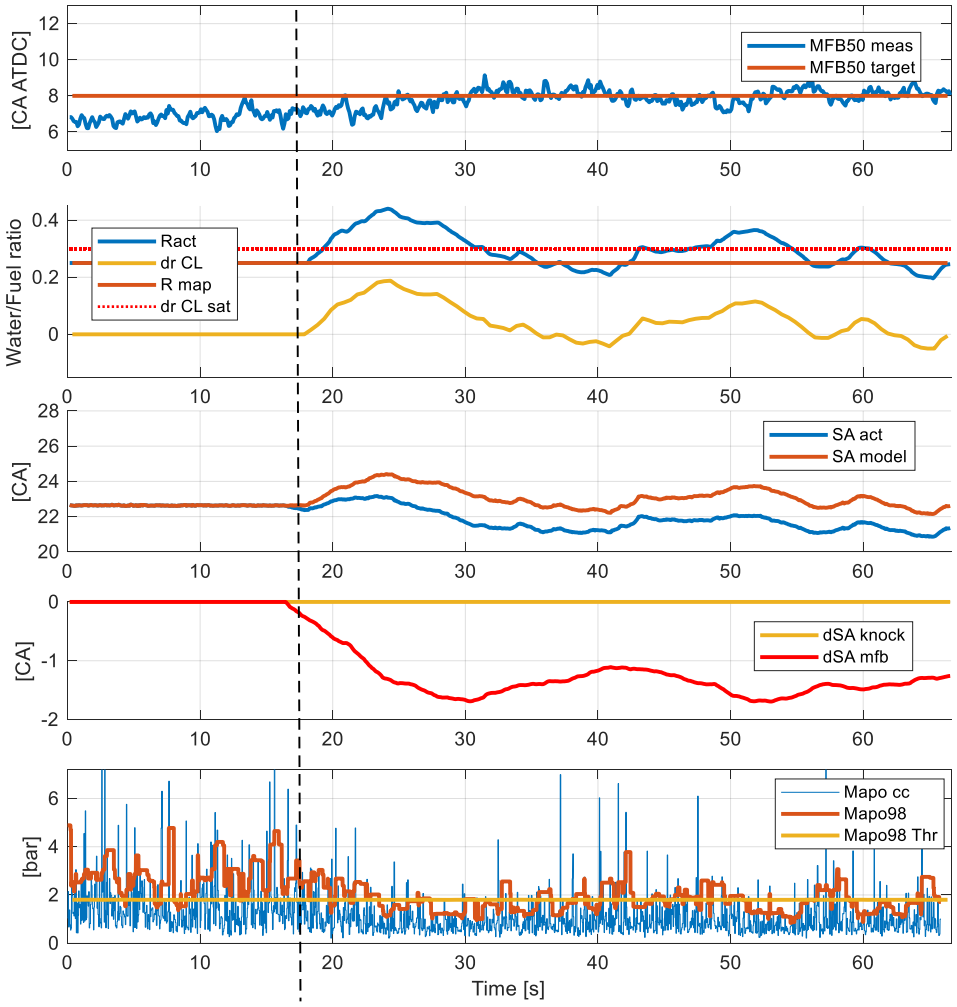

Figure 7.4 Steady state engine point 2700 RPM, 1.22 NL, Cylinder 3. At second 18 the controller switches from open loop to closed loop: dSAmfb starts to compensate SA model (as seen in Figure 10) and correction dR CL compensates R map (mapped value of r) to keep Mapo98 (knock Index) close to threshold (Mapo98 Thr).

Figure 7.5 displays a situation in which from the start both branches are set in CL. At second 13 a sudden change in MFB50 target is imposed in order to generate a high knock tendency with the intention of stimulating a strong response of the controller. After second 13, SA changes instantly due to the model's reaction to the MFB50 target change, real MFB50 is anticipated and knock level increases. The knock branch immediately acts to lower knock by adding water and quickly saturates at dR PID = 0.3. In case of saturation, MFB50 branch is forbidden to add positive contributions to SA (advancing SA). From the moment in which dR PID saturates, the SA calculated by the model remains constant due to a constant MFB50 target and R map (given dR PID saturation) and the SA correction from the knock branch (dSAknock) starts to retard combustion until MAPO98 is lowered to threshold. Furthermore, a delaying of MFB50 respect to the target is allowed giving the priority to maintain MAPO98 at threshold

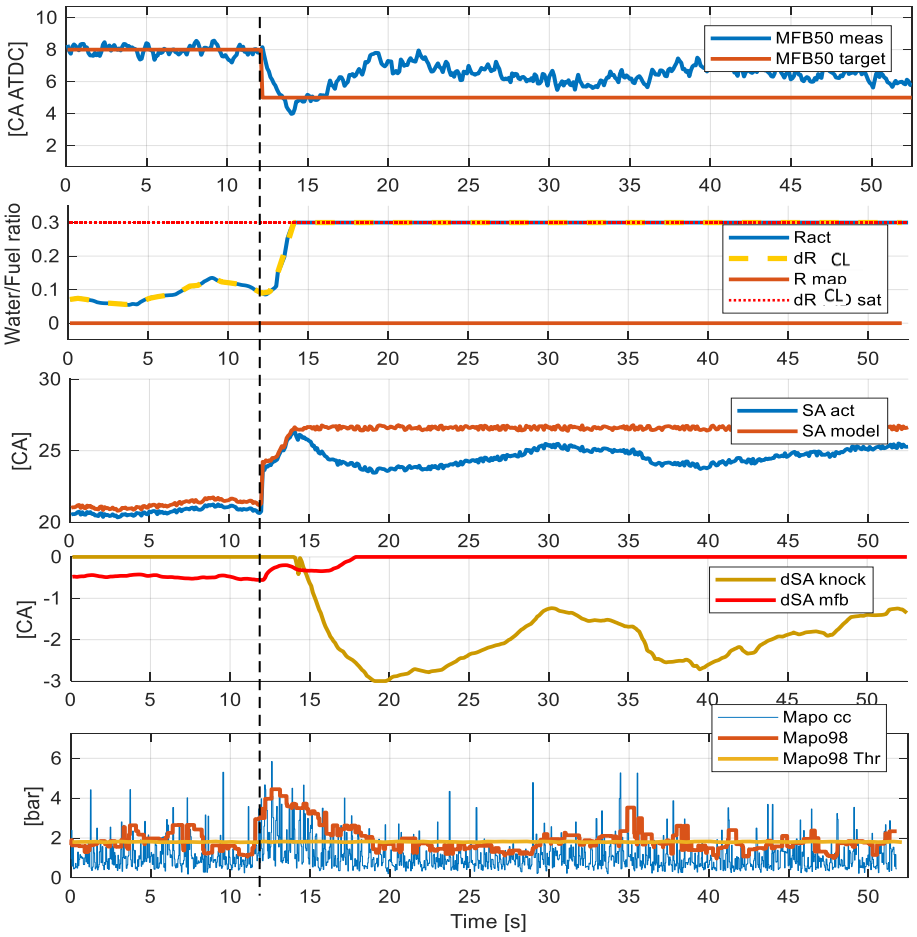

Figure 7.5 Engine point 2700 RPM, 1.22 NL, Cylinder 4. The controller is in closed loop. After second 13 MFB50 target is moved to an advanced value to stimulate high knock tendency. After 2 seconds dR PID, attempting to compensate Ract reaches saturation value (dR PID sat). After saturation, dSA mfb is limited to negative values and correction dSAknock starts to apply correction on SAact to delay MFB50.

Figure 7.6 presents a situation in which the value R map has been lowered from the calibrated one in order to obtain a higher knock level (over threshold of MAPO98). In this test the MFB50 branch is activated from the beginning and at second 35 also the knock CL branch is activated as well.

This test proves that the knock branch is able to quickly lower MAPO98 to threshold when being activated in a over-threshold situation. In this case, after dR PID saturation around second 38, MFB50 can still be close to target since the amount of water injected at saturation is almost just enough to keep MAPO98 at threshold. This is also the reason why corrections of dSA knock are small (less than 2 CA).

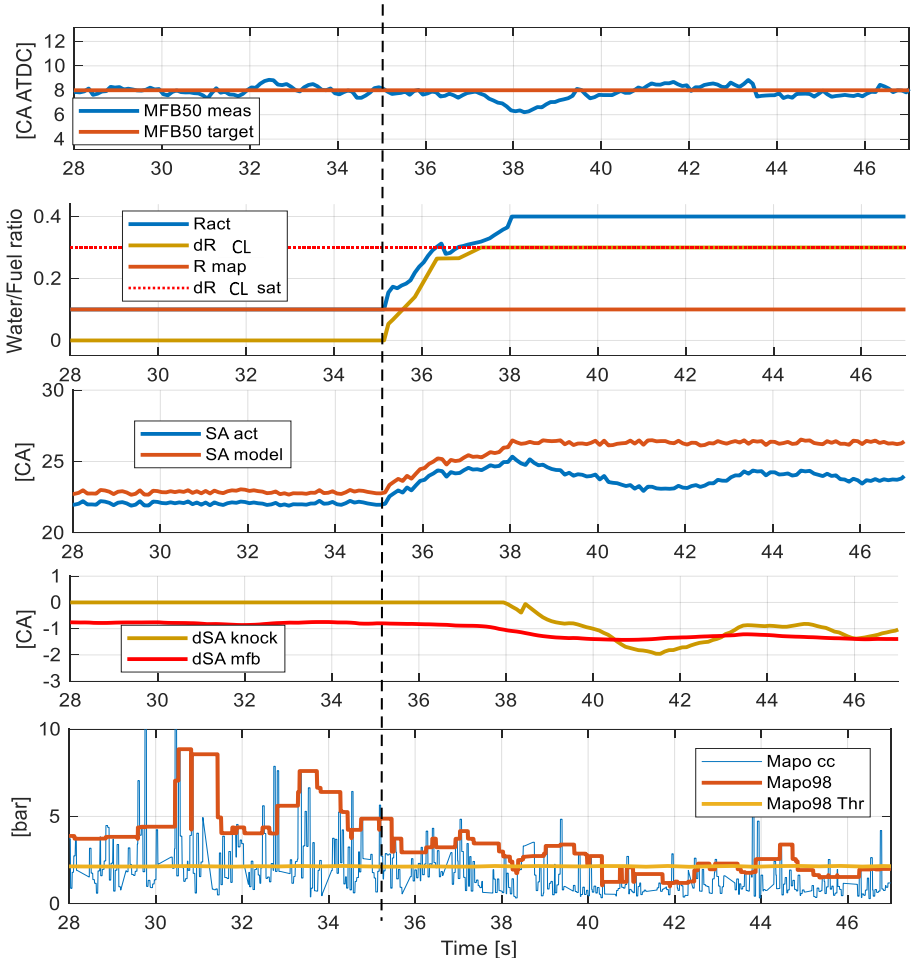

Figure 7.6 Engine point 3200 RPM, 1.3 NL, Cylinder 4. At time 0, the controller is in closed loop only for MFB50 and knock index exceeds the threshold value. After second 38 even loop on Mapo98 is closed.

7.4 Controller response in a transient condition

In Figure 7.7 a transient situation is presented, reproducing a real situation in which there is a sudden change of load and RPM increase gradually.

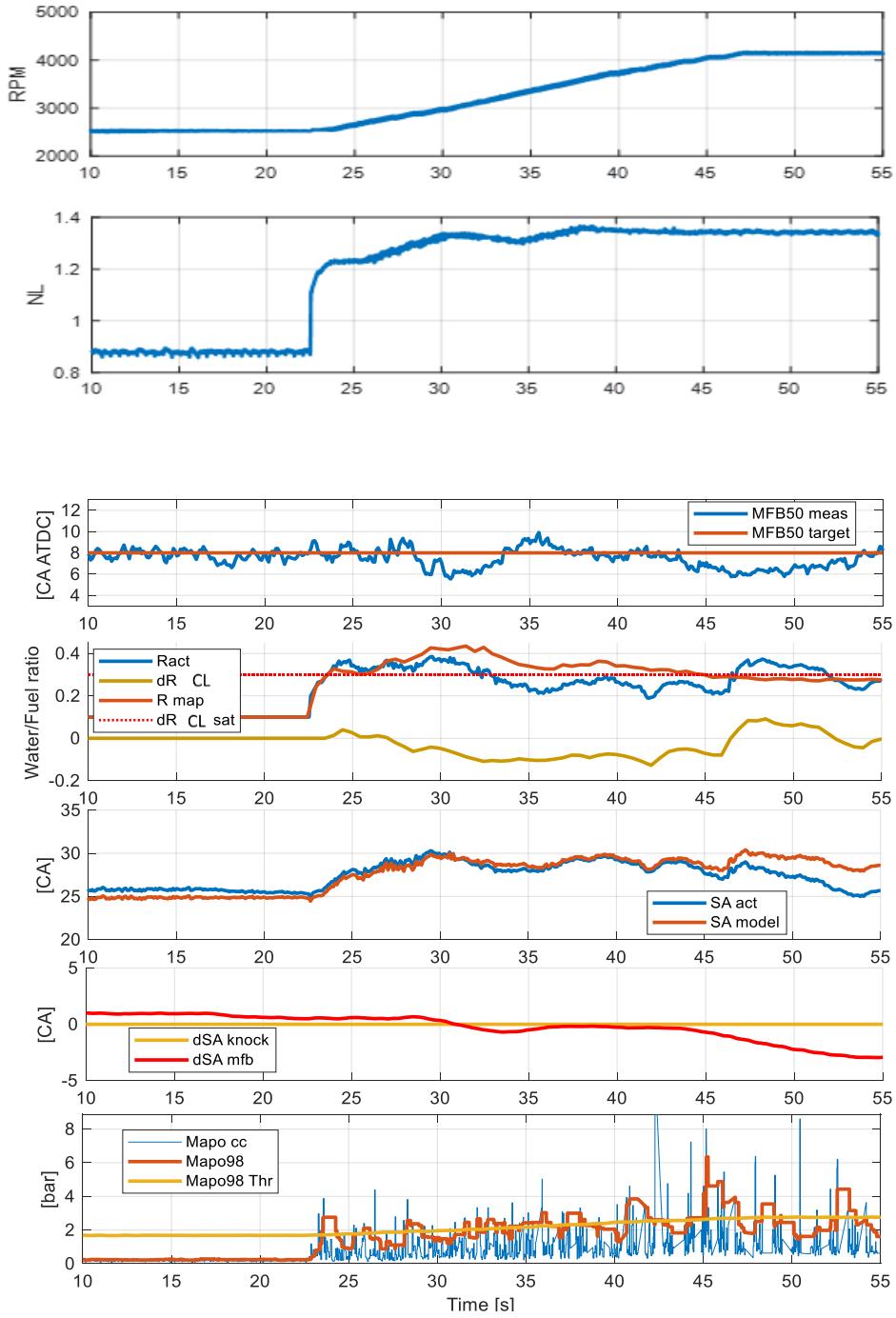

Figure 7.7 Transient test controller performance, Cylinder 1.

It has been displayed how the controller can retain knock levels at MAPO98 threshold while in transient conditions as well. R map changes over time due to the everchanging engine point and the knock branch does not saturate at any moment due to a well calibrated r MAP. dR PID adds corrections that keep r values close to mapped ones. This can also be noted by the fact that when the sudden change in load is applied, MAPO98 still stays at threshold and does not go over it, demonstrating the capabilities of the open loop. Closed loop works as it should, making small adjustments to keep MAPO98 and MFB50 at threshold.

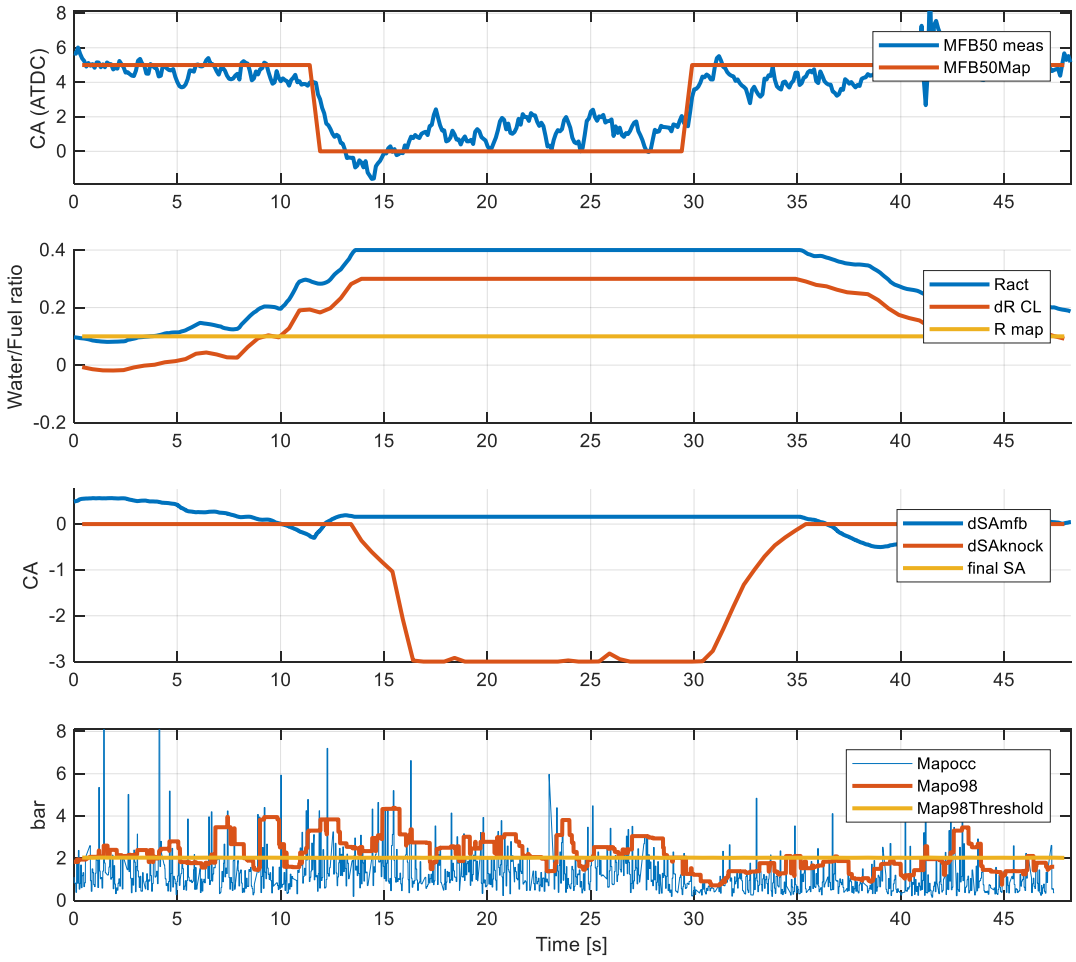

Figure 7.8

7.5 Fuel consumption implications

The performance of the Combustion Controller can be also quantified in terms of fuel consumption savings. WI is utilized to mitigate knock and lower EGT while allowing for greater values of SA. When not using WI, it is necessary to enrich the mixture to achieve these same goals, with the inevitable associated increase in fuel consumption.

To evaluate this fuel consumption difference, two tests were made, one with WI and another without. Both tests were conducted at 2700rpm and 1.45 NL. In the case of WI, a value of r = 0.8 was used to mitigate knock as much as possible and SA was set so that MFB50 was as close as possible to the optimum 8 CA ATDC, while remaining below an established MAPO98 limit value of 2 bar. The non-WI test was conducted in a similar way, in which λ and SA are set up in order to be as close as possible to optimal MFB50 and stay below the 2 bar MAPO98 limit. The results are summarized in Table 7-1.

The results with WI show an improvement in fuel consumption of 16% compared to the non-WI test, given mainly by the difference in λ. Even though the WI test has a more anticipated MFB50 value, the non-WI test shows a higher IMEP. The reason is related to the IMEP degradation at high r value. Therefore, in this case the gain of efficiency is due to both the avoiding of λ enrichment and the achievement of a more efficient combustion phase.

Table 7-1 Comparison between WI and non-WI tests (2700rpm, 1.45 NL).

	With WI	Without WI
Water / Fuel ratio (*r*)	0.8	0
MFB50 [CA ATDC]	12	18
MAPO98 [bar]	1.9	2
IMEP [bar]	16.7	17.3
Lambda	1	0.89
EGT [°C]	786	818
Indicated Torque	185	187
Fuel Consumption	11.3	13.5
Indicated Specific Fuel Consumption [g/kWh]	216	257

8 MFB50 Estimation by accelerometric signal

8.1 Signal analysis

The main inputs for the closed loop section of the Combustion Controller are MAPO98 and MFB50, being both measurements taken from the processing of the in-cylinder pressure signal, during the previously shown WICC validation campaign. With an on-board application as a goal, the replacement of the in-cylinder pressure sensor with an on-board available alternative is necessary. Accelerometers are widely used to detect knock via a high pass filtering of the signal. This opens the opportunity to evaluate the possibility of using this very same signal, processed differently, for combustion phasing detection as well. It is already known that there is a correlation between the peak angular position of in-cylinder pressure derivative and MFB50 [29], reason why the first step of the analysis is to determine if the accelerometer can generate a signal that is able to identify this peak.

A vast number of experimental tests at different engine points have been carried out, ranging from 1500rpm to 5500rpm and values of NL that are between 0.4 and 1.4. During these tests, both in-cylinder pressure sensors and accelerometers installed have been recorded.

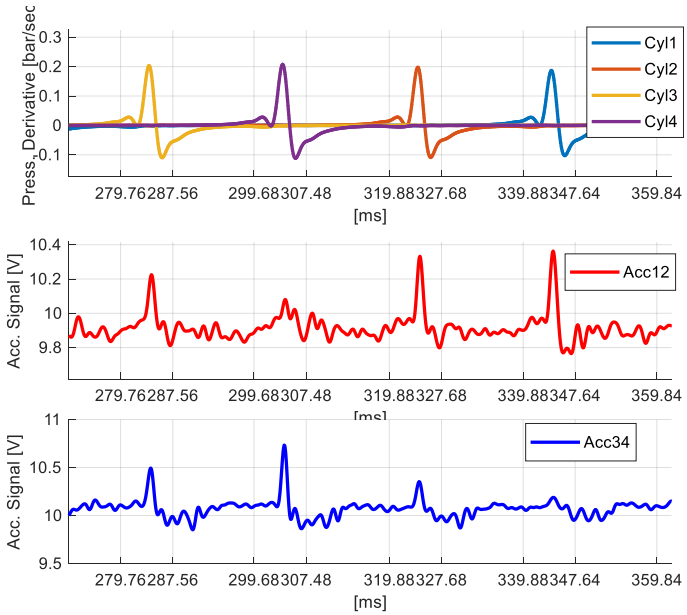

Figure 8.1 On top, derivative of in-cylinder pressure signal. In the middle and in the bottom, filtered accelerometric signal from the accelerometers (low pass 1 kHz), 1500 RPM and 1.2 NL.

A first processing of the accelerometric signal was made in order to understand the placement of the main frequencies related to combustion phasing. Contrary to knock, characterized by frequencies above 5 kHz, components of the accelerometric signal that can be used to identify combustion phasing are found in a frequency domain that can be as much as five times lower. A first analysis is made, using a 4th order Butterworth low pass filter with a cut-off frequency of 1 kHz. Figure 8.1 shows the results of this signal processing stage, from which it is immediately observed that near the peak of derivative of in-cylinder pressure related to a combustion event, there is a corresponding accelerometric signal peak as well. This implies that there is the possibility to directly correlate the position of the accelerometer peak and pressure derivative peak position (and therefore MFB50), as shown in Figure 8.2. As shown in Figure 15, the peak is more relevant for the cylinder located near to the sensor analysed. To ensure a more precise peak detection, its identification is carried out inside an angular window in which only combustion occurs, excluding all the rest of the cycle phases.

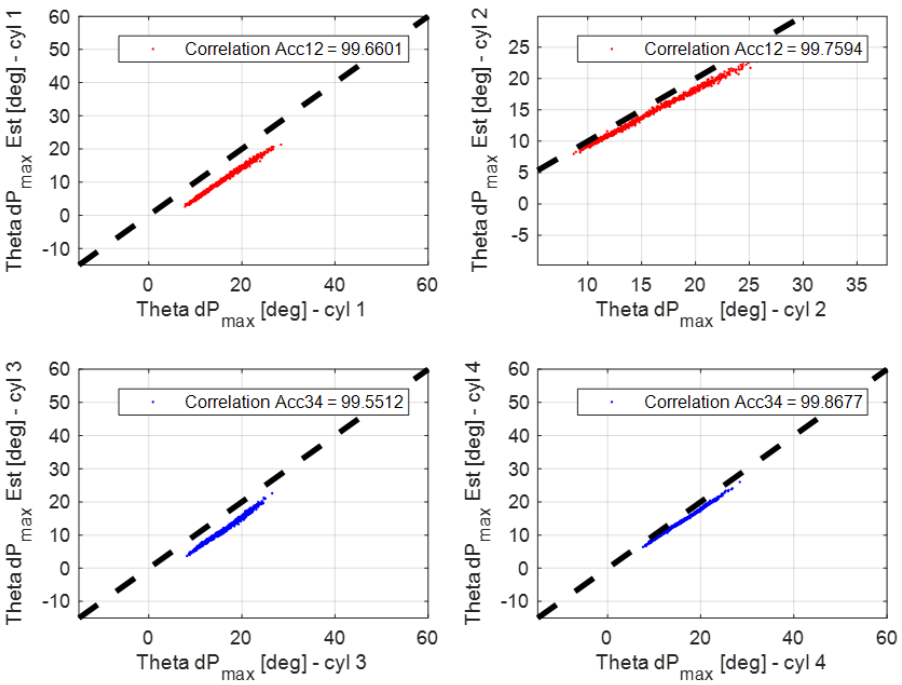

Figure 8.2 Correlation between derivative pressure angular position (Theta dPmax) and accelerometric signal peak (Theta dPmax Est.).

From this preliminary analysis, mainly two observations can be made. The first, there is a time (and thus angular) delay between the peak of the pressure derivative signal and the one from the accelerometric signal. The physical explanation relies on the fact that the vibrations from the instant of maximum in-cylinder pressure variation must mechanically travel through the engine block before arriving to the accelerometer sensor. This process takes time and generates a delay between the physical event in the combustion chamber

and its detection by the accelerometer. This delay, called angular delay, is not constant for all engine points and needs to be adequately identified. The second observation is that the cut-off frequency used on the low pass filtering process of the accelerometric signal impacts on the correlation between its peak and the location of MFB50. This implies that there is the need to generate a map with the cut-off frequency that maximizes correlation at each engine point. Figure 8.4 displays the results from the filtered accelerometric signal for a specific engine point as an example. Angular delay can be calculated as:

$$Angular\ delay = \sum_{i=1}^{N} \frac{(Acc.Peak - MFB50meas)_i}{N}$$

Where Acc.Peak is the position of the maximum value of the filtered accelerometric signal inside the angular window and MFB50 measured with in-cylinder pressure sensor, both registered in same cycle. Therefore, the estimation of MFB50 by accelerometric signal (for each cycle) can be defined by equation below.

MFB50est=AccPeak-Angular delay

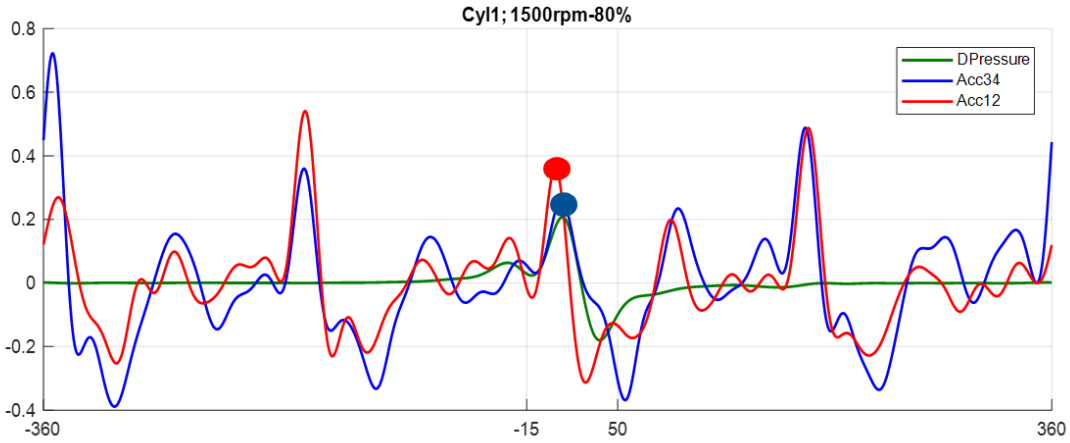

Figure 8.3 Filtered signal of accelerometer 12 and accelerometer 34 (low-pass filtered). Windowing the combustion phase, a peak can be clearly detected in both signals and also in in-cylinder pressure derivative (green).

As shown in Figure 8.4, a correlation of over 90% can be obtained between accelerometric signal peak and measured MFB50 from indicating system. All the forthcoming results are obtained using the accelerometer positioned between cylinders 1 and 2 to observe those two cylinders, and in the same way the other sensor has been used for cylinders 3 and 4. General trends show that at mid and high loads, correlation remains

above 90% while at low loads (NL < 0.6), the accelerometric signal is not able to generate a distinctive peak due to a lack of combustion intensity, resulting in a correlation under 50%.

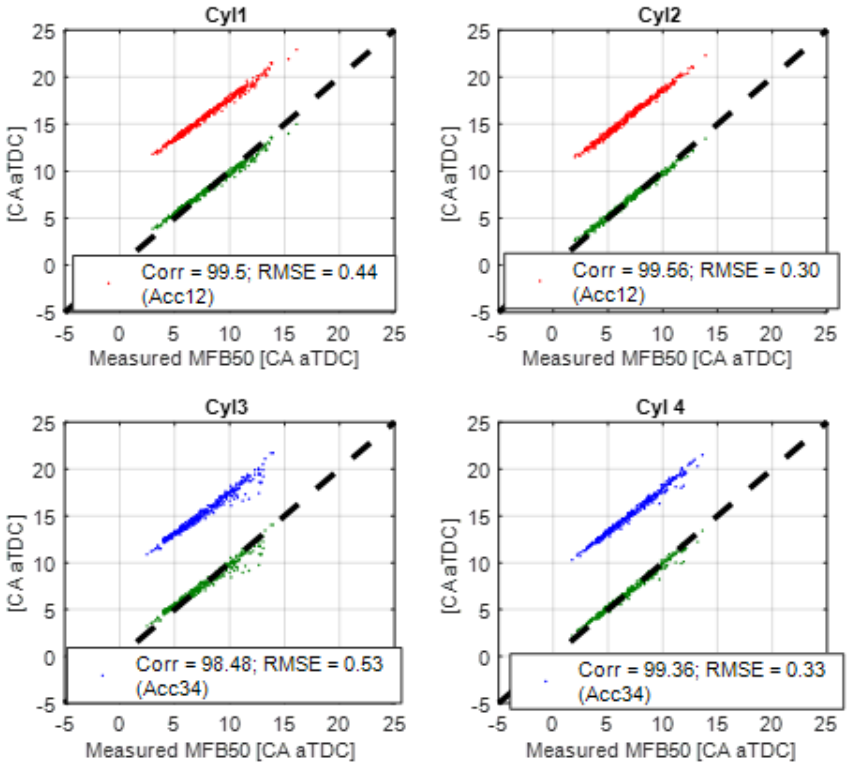

Figure 8.4 Correlation between accelerometric signal peak and MFB50 measured with in-cylinder pressure sensor. 2500 RPM 1.1 NL. Red and blue dots represent the correlation obtained without angular compensation (red=Acc12; blue Acc34). Green dots represent the correlation with angular delay compensation (MFB50 estimated).

8.2 Signal processing algorithm and calibration

Once it was established that it is possible to estimate combustion phasing with accelerometric signal, an algorithm has been designed in order to obtain the best results at each engine point. The strategy consists in signal windowing to focus on the combustion phase, a low-pass filtering, peak recognition and angular delay compensation (Figure 8.5). The algorithm has been calibrated by three steps:

- windowing of the accelerometric signal to be processed
- selection of the cut-off frequency for signal filtering
- angular delay identification.

Signal windowing has been imposed from 5 CA until 70 CA after spark event, interval in which accelerometric signal peak is generally located. Regarding the other two factors, optimum cut-off frequency and angular delay are identified and mapped for each of the tested engine points, process that is explained in the following paragraphs.

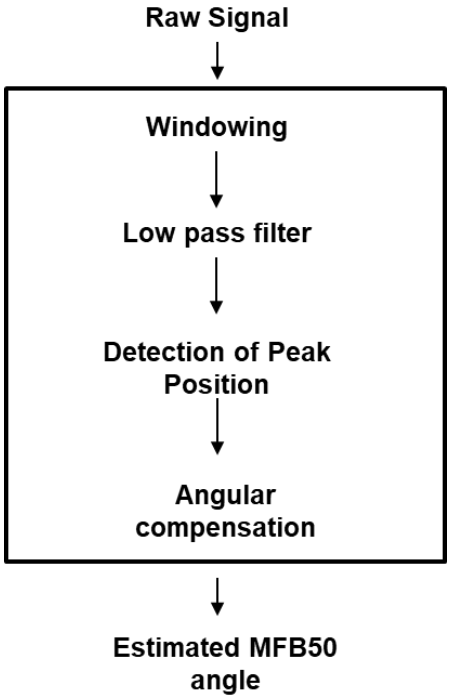

Figure 8.5 Block diagram of accelerometric signal processing algorithm

To evaluate the performance of the algorithm, the Root Mean Square Error (RMSE) is calculated for each engine point in order to determine the angular error between the estimation of MFB50 by accelerometric signal and that calculated by the indicating system. These are calculated as follows:

$$RMSE = \sqrt{\frac{\sum_{i=1}^{N}(MFB50est - \overline{MFB50meas})_i^2}{N_{Cycles}}}$$

As a first procedure, a sweep of cut-off frequency is made at each engine point using a Design of Experiment (DOE), in order to find the frequency that minimizes the calibration RMSE. Figure 8.6 displays the results from the DOE for several cases of load at 2500rpm as an example.

This optimal cut-off frequency is not equal for all four cylinders and as predicted, depends on both engine speed and load (mainly RPM), and ranges from 400 Hz to 1500 Hz. After the DOE, a cut-off frequency as

function of RPM has been selected, shown in Table 8-1. The dependence with load has been neglected in order to make the maps as smooth as possible.

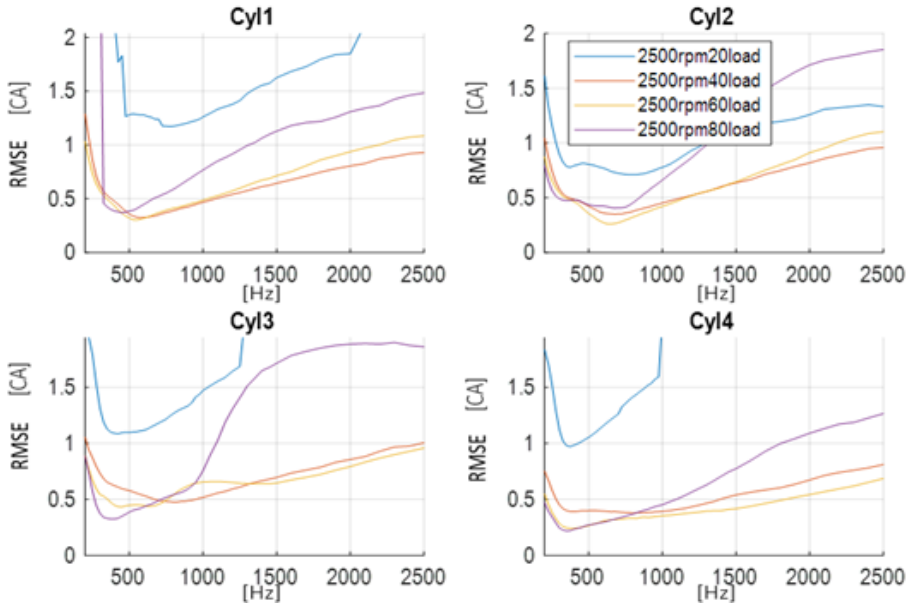

Figure 8.6 RMSE vs Cut-off frequency for 2500 RPM and 1.4 NL.

The cut-off frequency for each engine point in the grid is identified and mapped, the angular delay associated to each cut-off frequency is mapped as well. The final scatter of points is displayed by the green points of Figure 8.4, which are shifted towards the black dashed line corresponding to the real MFB50 angle. In Figure 8.8 the angular compensation map is shown. It's clear that the required compensation is higher as long the speed increase.

Table 8-1 Cut-off frequency [Hz] map

NL\RPM	**1500**	**2500**	**3500**	**4500**	**5500**
0.6	\	600	700	800	\
1.0	500	600	700	800	900
1.2	500	600	700	800	900
1.6	500	600	700	800	900

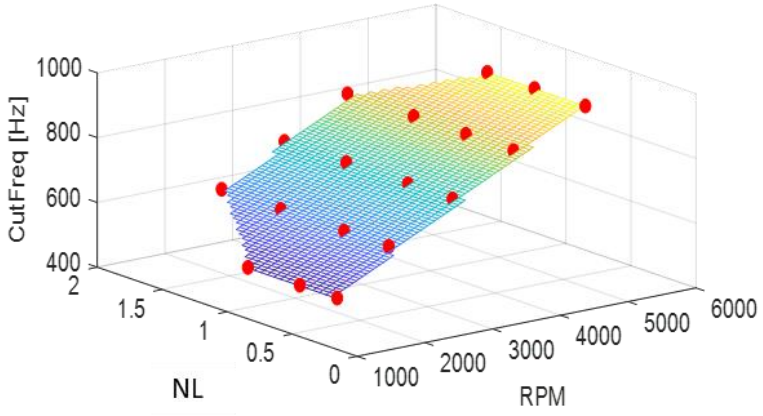

Figure 8.7 Cut-off frequency [Hz] map

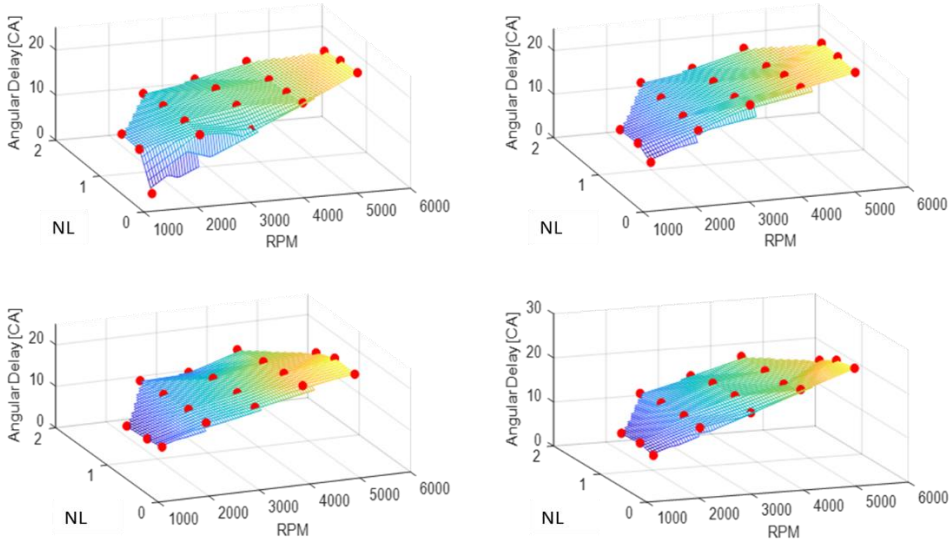

Figure 8.8 Angular compensation Map

8.3 Experimental validation

The tables below contain the results of the algorithm applied to each tested engine point, in just one cylinder as example. Correlation coefficients seen in Table 8-2 are above 95% in all cases except at 4400rpm and 1.6 NL, point in which the accelerometric signal presented difficulties to generate a clean peak, even after filtering. Table 8-3 displays the RMSE for all tested engine points and denotes those out of the preestablished limit of 1 CA. A general trend has been observed in which over a certain limit of RPM, accelerometric signal starts to be affected by vibrations from other sources that finally impact in the precision of the MFB50 estimation. These vibration disturbances in the signal could not be eliminated with filtering because of being in the same frequency spectrum than the signal coming from cylinder combustion.

Table 8-2 Correlation between estimated MFB50 from accelerometer and indicating system. From top: Cylinder 1 ,2 ,3 ,4.

NL\RPM	2000	2400	3000	3600	4000	4400	5200
0.6	98,2	96,9	96,9	96,9	87,1	95,4	93,1
0.8	99,2	99,4	99,2	98,7	96,2	96,0	96,8
1.0	99,6	99,6	99,3	99,2	98,8	98,4	97,9
1.2	99,4	99,5	99,1	99,2	98,7	98,4	97,0
1.6	\	98,8	97,1	97,7	96,9	40,3	\

NL\RPM	2000	2400	3000	3600	4000	4400	5200
0.6	98,1	98,3	98,7	98,3	97,6	95,0	93,7
0.8	99,1	99,5	99,3	99,0	98,8	96,7	94,8
1.0	99,5	99,1	99,5	99,2	99,0	98,6	95,9
1.2	99,3	99,3	99,4	99,2	98,5	98,5	96,5
1.6	\	98,9	98,8	98,3	97,6	36,4	\

NL\RPM	2000	2400	3000	3600	4000	4400	5200
0.6	93,5	91,3	95,0	94,0	94,3	94,3	87,6
0.8	98,4	97,7	97,7	97,6	96,9	96,8	92,8
1.0	98,8	98,5	96,1	97,9	98,2	98,1	94,4
1.2	98,7	98,4	98,4	97,4	98,6	97,5	95,1
1.6	\	97,1	97,2	92,5	95,8	49,1	\

NL\RPM	2000	2400	3000	3600	4000	4400	5200
0.6	93,5	91,3	95,0	94,0	94,3	94,3	87,6
0.8	98,4	97,7	97,7	97,6	96,9	96,8	92,8
1.0	98,8	98,5	96,1	97,9	98,2	98,1	94,4
1.2	98,7	98,4	98,4	97,4	98,6	97,5	95,1
1.6	\	97,1	97,2	92,5	95,8	49,1	\

Table 8-3 RMSE between estimated MFB50 from accelerometer and indicating system. From top: Cylinder 1 ,2 ,3 ,4.

NL\RPM	2000	2400	3000	3600	4000	4400	5200
0.6	0,80	0,90	1,30	2,00	2,30	1,70	4,10
0.8	0,40	0,40	1,10	1,50	1,80	1,50	1,80
1.0	0,30	0,30	0,60	0,50	0,70	0,70	1,40
1.2	0,40	0,50	0,60	0,40	0,70	1,00	0,90
1.6	\	0,40	1,50	0,60	0,70	1,80	\

NL\RPM	2000	2400	3000	3600	4000	4400	5200
0.6	0.80	0.90	0.60	1.00	0.90	1.30	2.60
0.8	0.60	0.80	0.70	0.50	0.70	1.20	1.90
1.0	0.40	0.50	0.50	0.40	0.60	0.70	1.80
1.2	0.30	0.30	0.50	0.40	0.90	0.40	1.60
1.6	\	0.40	0.50	0.50	0.60	1.90	\

NL\RPM	2000	2400	3000	3600	4000	4400	5200
0.6	1,20	1,40	1,50	1,30	1,30	1,60	2,20
0.8	0,80	0,80	0,70	0,90	1,00	0,90	1,70
1.0	0,60	0,60	1,00	0,80	1,50	0,60	1,30
1.2	0,50	0,60	0,90	0,80	1,70	0,60	1,10
1.6	\	0,70	0,70	0,80	3,40	1,70	\

NL\RPM	2000	2400	3000	3600	4000	4400	5200
0.6	0,80	1,40	2,10	1,50	0,90	0,80	1,40
0.8	0,60	0,70	0,90	0,80	2,00	1,10	2,70
1.0	0,50	0,70	0,50	0,50	0,70	0,90	3,00
1.2	0,60	0,50	0,40	0,40	0,80	0,90	2,40
1.6	\	0,60	0,50	0,50	0,80	2,30	\

9 Control strategy for Hybrid Powertrain

The management of vehicle efficiency can be extended considering a more complex powertrain such as a hybrid lay-out. In fact, a combustion controller able to manage the engine efficiency could be very important as a part of energy management system of a hybrid system. In this case, the control design must involve an overall approach considering all the single components with less detail. In fact, the focus is actually the power flow that connect engine, electric motor, battery and wheels and define the best strategy to reduce the energy consumed by the vehicle.

During the period abroad the study of efficient powertrain control system has been integrated with a focus activity on hybrid lay-out. The activity consisted in a modelling phase to obtain a Simulink model of the powertrain and then has been focused on the calibration of an Energy Consumption Minimization Strategy (ECMS).

The simulation approach involved a PID to simulate a driver that is trying to follow a vehicle speed target. The driver provides as output of the PID the acceleration and deceleration requests to the HCU (Hybrid Control Unit) that applies all the command signals to the vehicle model. This model produces the actual final speed that represents the feedback for the driver PID, as shown in Figure 9.1.

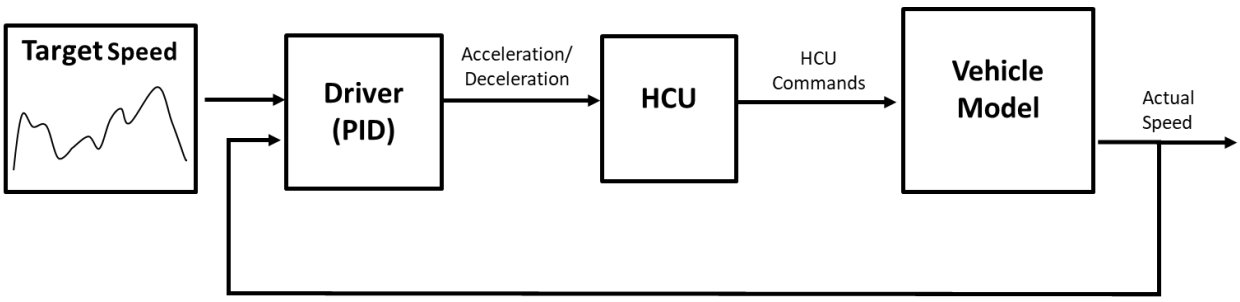

Figure 9.1

9.1 Driveline Modelling

The plant involves 3 different propulsion machines, one internal combustion engine and two electric motors, and a battery as energy storage. One motor has been coupled with the front axis (configuration P4), while on the rear axis the ICE and the other motor have been installed, mechanically linked by the gearbox. For this reason, the modelling of the gearbox has been the main focus. This part consists in a Dual Clutch Transmission type, where the even gears and the odd gears are organized in two different shafts, and each shaft can be

coupled to the engine shaft by a dedicated clutch. The rear electric motor can be coupled to the odd gear shaft.

In this way, a wide range of combination of ICE gears and EM gears can be applied even if some specific combinations are mechanically unfeasible. This configuration is called P2.5 and is shown in Figure 9.2.

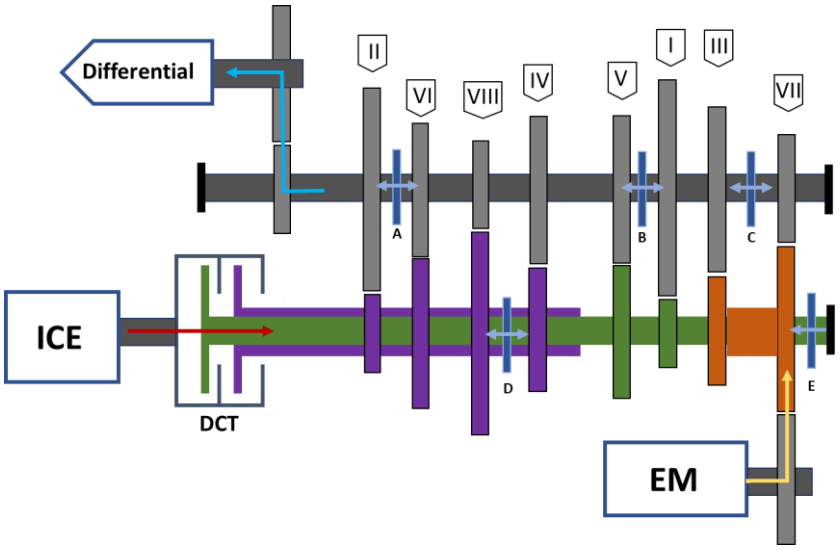

Figure 9.2 Dual Clutch transmission layout. A,B,C,D,E represent the synchronizer

. The drivetrain layout is explained in Figure 9.3, and can be summarized in 3 steps.

1. The DCT model receives the ICE and rear EM torque together with command signal of every gear from ECU. Regarding ICE torque, the DCT requires at same time the command of present gear and the preselected gear. The second one represents the next gear to be applied, because it can be actually prepared on the free shaft (the one not engaged with the ICE). During the gearshift, the ICE engagement shifts from one shaft to the other, changing quickly the gear ratio.
2. Front and rear differential model. The front one receives the input torque DCT block and the other one receives the front EM torque. Each one provides the output torque to the respective wheel block that gives in return the wheel speed feedback.
3. In the same way each wheel block provides the horizontal force to the vehicle model (that simplifies the problem considering only one dimension of movement). In return this model provides as feedback the vehicle speed.

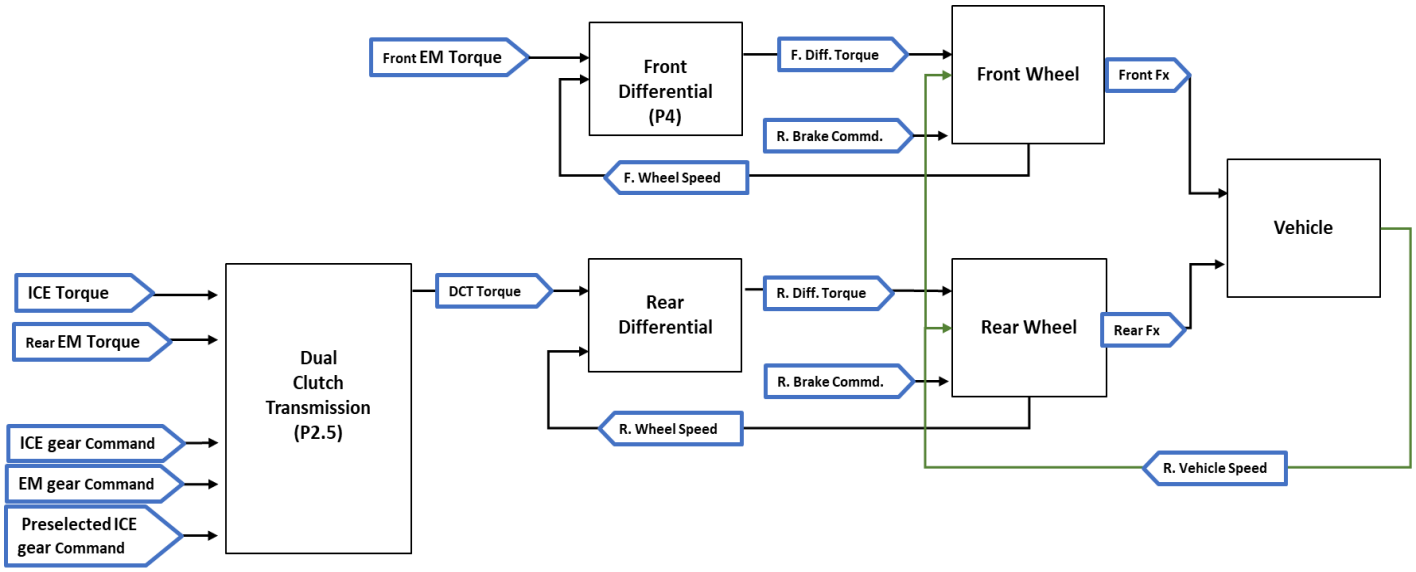

Figure 9.3 Driveline Layout

In Figure 9.4 the DCT layout is displayed. From this point the shafts related to clutch 1 and clutch 2 are called respectively K1 and K2. The DCT model consists in 3 main blocks:

1. the DCT controller processes the command from ECU commands together with the K1 and K2 position and ICE speed. This block must combine and coordinate the requests by a low-level controller and it provides an internal command for each DCT part (clutches K1 and K2 and synchronizers).
2. The clutch model receives the commands from the controller and processes the physical inputs of ICE torque, K1/K2 speed and a feedback on synchronizers operative state (sliding or locked). It provides the values of K1 and K2 torque together with the operative clutch state.
3. The model of synchronizers receives the command from the controller and processes the physical inputs of EM torque and the K1 and K2 torque together with their operative states from the previous block.

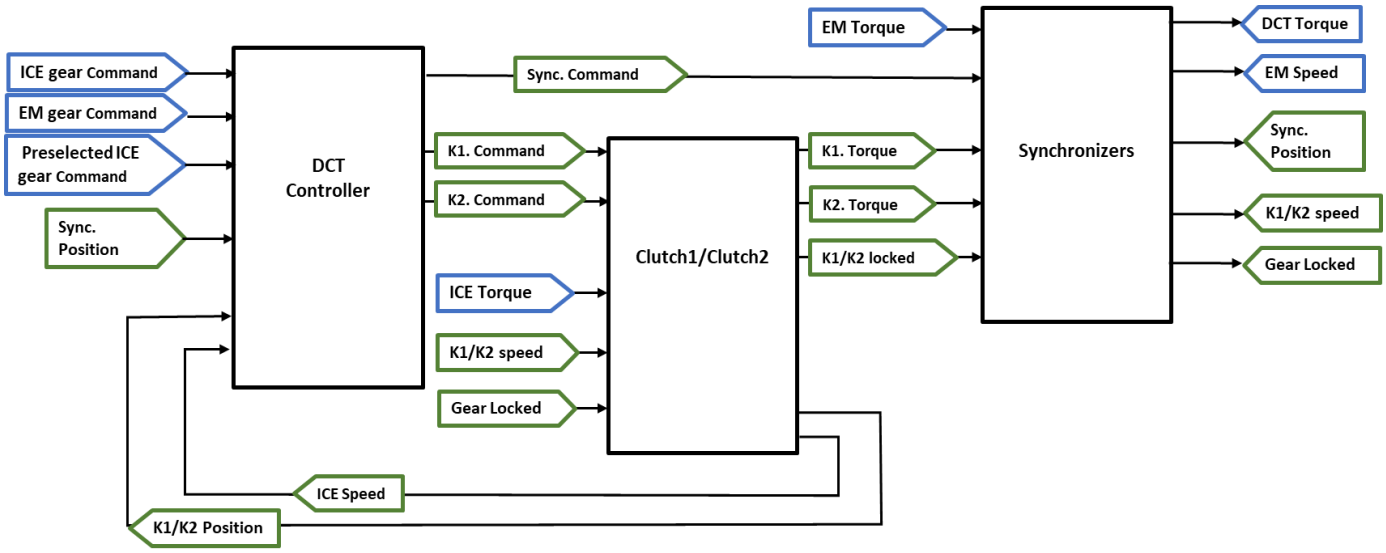

Figure 9.4 Dual Clutch Trasmission Layout

After the modelling, the lower-level control strategy has been developed to obtain a proper management of all the gearbox-controlled parts, the clutches and the synchronizers, to employ a gearshift. The strategy must handle eventually a simultaneous request of ICE shift and electric shift. The strategy implemented has been defined pursuing the maximum simplicity. During normal operation, one of the two shafts of DCT is engaged with the ICE gear while the other is not connected to the engine. This 'free' shaft must be prepared to handle the upper ICE gear if requested, therefore its synchronizers must be already set in position for the next gear.

When an upshift is requested, at first the two clutches are coordinated to transfer the ICE torque from a shaft to the 'free' one. After the torque handover, the controller manages the shifting of all the involved synchronizers. In this phase, the new 'free' shaft must be prepared to disengage the old gear and engage the next one (for example from 3rd to 5th). In the meanwhile, the synchronizers must be shifted to apply the electric gearshift if requested. The low-level control strategy has been summarized in Figure 9.5.

In case of downshift, the strategy is reverted. This time the DCT controller requests the shifting of the synchronizers at first. In fact, the free shaft that usually is ready for the upper gear must engage the lower gear and only after the engagement the DCT is ready for torque handover. Therefore, in this case the request for new clutches position must wait for the ready position of all the synchronizers.

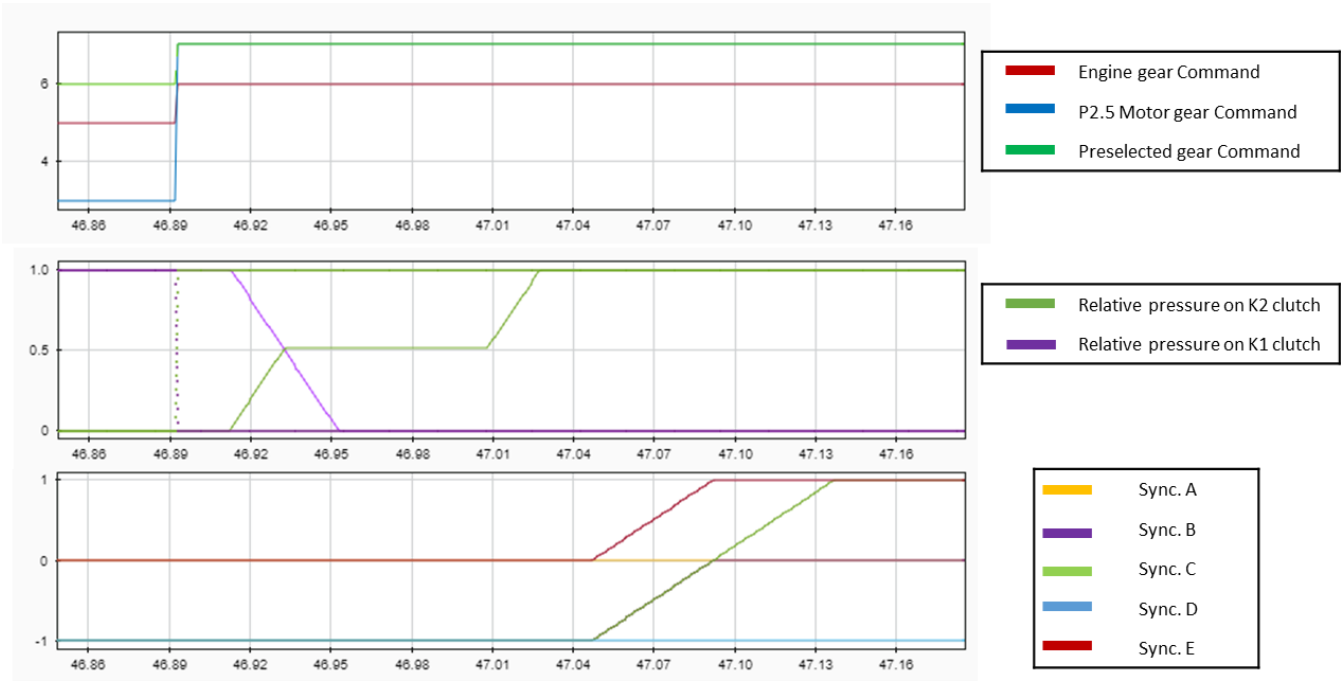

Figure 9.5 Upshift command from DCT controller for clutches and synchronizers

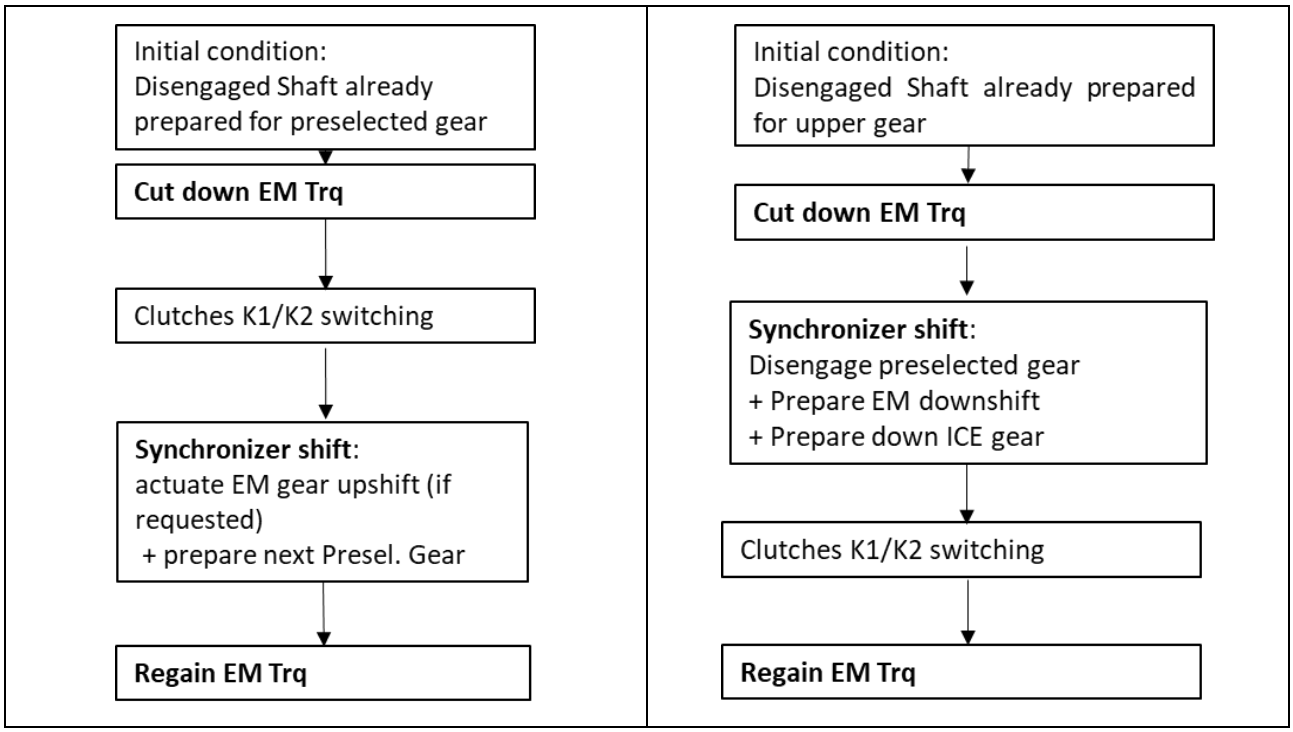

Figure 9.6 Algorithm concept for DCT controller.

9.2 ECMS calibration

In the second part of the project, the focus has been set on the energy management of the hybrid system. The strategy employed is the Energy Consumption Minimization Strategy (ECMS). In this strategy, Hybrid Control Unit computes for every iteration a set of equivalent fuel consumption ($\dot{m}_{eq}$).

$$\dot{m}_{eq}(soc, u, t) = \dot{m}_f(u, t) + \dot{m}_{bat}(soc, u, t) \qquad (13)$$

where:

- $\dot{m}_{bat} = s(soc, t, t-1) * \frac{P_{bat}(u)}{Q_{inv}}$; equivalent fuel consumption to battery energy flow, the conversion is related to a cost function s that provides a "value" to the power delivered by the battery in relation with SOC
- SOC: state of charge
- u = $\frac{El.\ Torque}{Requested\ Torque}$; split factor

Table 9-1 Summary of u state as function of Powertrain mode.

Mode	**Split factor**	**ICE**	**EM**
Elective drive	u=1	Off	On
Boosting	0<u<1	On	On
ICE only	u=0	On	Off
Batt. Recharge	$-u_{min}$<u<0	On	On

Through this system, the Hybrid Control Unit (HCU) can evaluate which is the optimal split factor between the ICE torque and the EM torque to obtain the minimal energy consumption from the overall system. The key feature is the definition of equivalent factor (s), which is a cost function that provide a weight value to the energy stored in the battery. This value will force the optimization module to choose a split factor to recharge the battery if the state of charge (SOC) is too low for example.

The aim of this vehicle is related both to fuel consumption and performance, in other words the use of the EM is important to extend the overall torque range during strong acceleration. In particular, the main goal was to perform a fast lap on Nürburgring track storing enough energy for the last acceleration, that is the most demanding one. For this reason, the cost function has been defined, and a charge sustaining strategy has been chosen using a SOC target sufficient to ensure the availability of electric torque for the last acceleration.

The cost function has been defined by the following function, described in [28]:

$$s = \left[1 - K_p * \left(\frac{SOC(t) * \frac{SOC_{max} - SOC_{min}}{2}}{\frac{SOC_{max} - SOC_{min}}{2}}\right)^3\right] * \left[(SOC_{target} - SOC(t)) * K_a + \frac{(s_{t-1} + s_{t-2})}{2}\right] \quad (14)$$

In this implementation, the integral term $\frac{(s_{t-1}+s_{t-2})}{2}$ has been limited by a saturation. To calibrate K_p, the response of s in relation with SOC value has been investigated.

Calling:

$\left[1 - K_p * \left(\frac{SOC(t) * \frac{SOC_{max} - SOC_{min}}{2}}{\frac{SOC_{max} - SOC_{min}}{2}}\right)^3\right]$ penalty function

$(SOC_{target} - SOC(t)) * K_a$ adaptive term

Studying the product of these two terms (basically s factor without integral term), it has been selected a K_p value of 0.002 resulting in the response shown in Figure 9.7 .

Boundary condition:

- SOCmin=20%; SOCmax=90%; SOCtarget=50%.
- Ka=0.1

In this case s-factor features a positive response in case of SOC<SOCtarget and negative in case of SOC>SOCtarget. Higher values of K_p could lead to a wrong response.

The ECMS has been tested at first in a configuration able to manage the torque split of ICE and both electric motors. At the end this configuration has been simplified to manage only the propulsion at the rear axle. In this way, the requested torque by the driver is split between front and rear axis by a 'drive assistance' controller and then the torque to the rear is split between EM and ICE by the ECMS. In Figure 9.8 it is shown the results of a proper calibration of *s.* In this case the SOC target is set to 70% and the initial SOC is equal to SOCmax (90%), and the vehicle speed target represents a Nurburgring lap.

The simulation displays a first decrement of SOC below the target, close to 60% (sec. 90). After this time, the ECMS forces the battery recharge up to 70%. The recharging speed is limited by the boundary on battery plant in which the discharge can be 10 times faster than the charge. At the end of the lap, there is the most demanding phase in terms of power requested. Therefore, the SOC is affected by a new faster decrement. Since at the end of the lap the SOC is still close to 60%, this calibration is able also to manage more than one lap with this boundary condition.

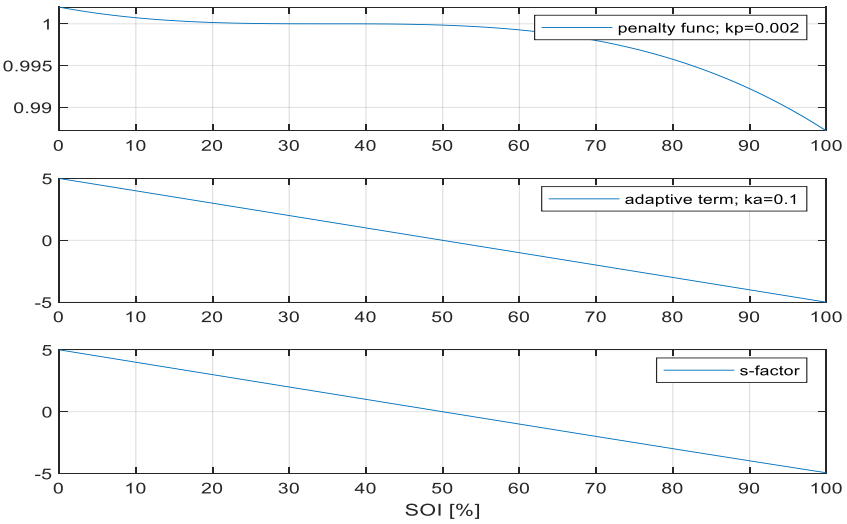

Figure 9.7

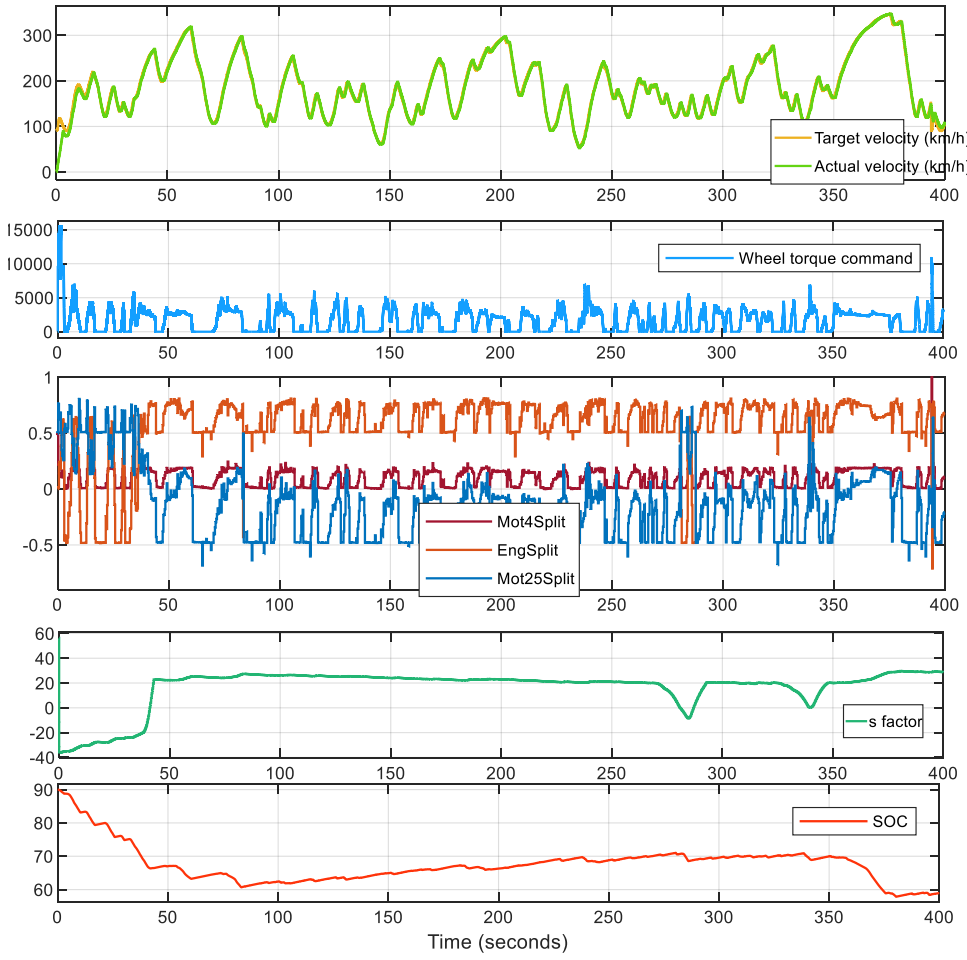

Figure 9.8 Nürburgring lap. Mot4Split, EngSplit and Mot25Split represent respectively the splitting power factor of EM P4, ICE, EM P2.5 in relation to the overall power flow.

10 Conclusions

The investigation campaign on TSI prototypal setup confirmed the knock mitigation effect of water injection considering all the operative conditions, especially load, speed and combustion phase angle. On the other hand, the increment of the water-fuel ratio (*r*) leads to a proportional delay on the combustion phase angle, and the reason is mainly focused on the angular elongation of the first phase of the combustion process (0-10 °CA of MFB angle). For each value of water-fuel ratio the correlation between SA and MFB50 angle can be easily fitted by a parabolic function, and this suggested a control strategy based on a MFB50 target developed during the project. The study of the effect of Start of Injection does not provide relevant findings mainly due to the not optimal layout of the intake geometry.

As said before, the combustion phase angle and the water-fuel ratio are strictly related. To obtain an efficient way to control the WI system, a model-based approach has been investigated. Two versions of combustion models have been presented, both based on the parabolic function that can correlate SA and MFB50 and at same time modelling the relation between each parabolic parameter and speed, load and *r*. In this way, the model can compute the proper SA needed to obtain a target MFB50 angle taking into account the effects of *r*. The error on MFB50 angle has been shown during the validation tests on TSI setup and it is less than 2 CA with respect to the target. Furthermore, during a validation on a second setup, thanks to a wider model calibration effort, the error on SA has been quantified below 1 CA.

A complete model-based controller has been developed for the WI system management. Three versions of the control system have been presented, and the most complete involved a closed loop branch based on knock index, and one based on MFB50 angle, both obtained by indicating system. Through Software-in-the Loop and Rapid control Prototyping method, the performance and the functioning of the controller has been shown. The feasibility of knock mitigation by adding water without sensible variation in MFB50 (if WI is not saturated) has been demonstrated. In fact, the presence of variations of *r* does not affect significantly the combustion phase due to the model compensation, and the knock level can be stabilized to the established threshold. The addition of a closed-loop correction on MFB50 by in-cylinder pressure signal allows a better implementation of the controller, keeping the combustion phase on the target as long as *r* value is not saturated.

The MFB50 estimation by accelerometer signal is evaluated on a wide engine operating field using the second setup described. The proposed algorithm is capable of estimating MFB50 with a RMSE value below 1 CA with exception of a small area located at the highest speed.

The results on the MFB50 estimation activity demonstrate the feasibility to implement all the Water Injection Combustion Control in an on-board environment without the need of an indicating system. For this reason, the project will proceed with the implementation and validation of the whole controller in a development ECU in the new setup. Other further development will be adaptation of the WICC for the management of EGR. In fact, EGR produce a similar effect of WI on knock mitigation and combustion dilution. Finally, the development an integrated control system WI-EGR will be possible.

References

1. International Council on Clean Transportation, January 2019, “CO2 emission standards for passenger cars and light-commercial vehicles in the European Union”
2. Bozza, F., De Bellis, V., Teodosio, L., Tufano, D. et al., “Techniques for CO2 Emission Reduction over a WLTC. A Numerical Comparison of Increased Compression Ratio, Cooled EGR and Water Injection,” SAE Technical Paper 2018-37-0008, 2018, doi:10.4271/2018-37-0008.
3. Wirth, M. and Schulte, H., “Downsizing and Stratified Operation - An Attractive Combination Based on a Spray-Guided Combustion System,” International Conference on Automotive Technologies, Istanbul, 2006.
4. Police, G., Diana, S., Giglio, V., Iorio, B. et al., “Downsizing by SI-Engines by Turbo-Charging,” Proceedings of ESDA 2006, 8th Biennial ASME Conference on Engineering Systems Design and Analysis, July 4, 2006, Torino, Italy.
5. Luisi, S., Doria, V., Stroppiana, A., Millo, F. et al., “Experimental Investigation on Early and Late Intake Valve Closures for Knock Mitigation through Miller Cycle in a Downsized Turbocharged Engine,” SAE Technical Paper2015-01-0760, 2015, doi:10.4271/2015-01-0760.
6. Sellnau, M., Kunz, T., Sinnamon, J., and Burkhard, J., “2-Step Variable Valve Actuation: System Optimization and Integration on an SI Engine,” SAE Technical Paper 2006-01-0040, 2006, doi:10.4271/2006-01-0040.
7. Shelby, M.H., Leone, T.G., Byrd, K.D., and Wong, F.K., “Fuel Economy Potential of Variable Compression Ratio for Light Duty Vehicles,” SAE Technical Paper 2017-01-0639, 2017, doi:10.4271/2017-01-0639.
8. Francqueville, L. and Michel, J., “On the Effects of EGR on Spark-Ignited Gasoline Combustion at High Load,” SAE Int. J. Engines 7(4), 2014, doi:10.4271/2014-01-2628.
9. Szybist, J., Wagnon, S., Splitter, D., Pitz, W. et al., “The Reduced Effectiveness of EGR to Mitigate Knock at High Loads in Boosted SI Engines,” SAE Int. J. Engines 10(5):2305-2318, 2017, doi:10.4271/2017-24-0061.
10. Hoppe, F., Thewes, M., Baumgarten, H., and Dohmen, J., “Water Injection for Gasoline Engines: Potentials, Challenges, and Solutions,” International Journal of Engine Research 17(1):86-96, 2016, doi:10.1177/1468087415599867.
11. Soyelmez, M.S. and Ozcan, H., “Water Injection Effects on the Performance of Four-Cylinder, LPG Fuelled SI Engine,” Open Access Scientific Reports 2(1), 2013, doi:10.4172/scientificreports.591.
12. Busuttil, D. and Farrugia, M., “Experimental Investigation on the Effect of Injecting Water to the Air to Fuel Mixture in a Spark Ignition Engine,” MM (Modern Machinery) Science Journal 1:585-590, 2015.
13. D'Adamo, A., Berni, F., Breda, S., Lugli, M. et al., “Numerical Investigation on the Potentials of Water Injection as a Fuel Efficiency Enhancer in Highly Downsized GDI Engines,” SAE Technical Paper 2015-01-0393, 2015, doi:10.4271/2015-01-0393.
14. Boretti, A., “Water Injection in Directly Injected Turbocharged Spark Ignition Engines,” Applied Thermal Engineering 52(1):62-68, 2013, doi:10.1016/j. applthermaleng.2012.11.016.
15. Hopkinson, B., “A New Method of Cooling Gas-Engines,” Proceedings of the Institution of Mechanical Engineers 85:679-715, 1913.
16. Harrington, J.A., “Water Addition to Gasoline-Effect on Combustion, Emissions, Performance, and Knock,” SAE Technical Paper 820314, 1982, doi:10.4271/820314.

17. Durst, B., Unterweger, G., Rubbert, S., Witt, A. et al., “Thermodynamic Effects of Water Injection on Otto Cycle Engines with Different Water Injection Systems,” The Working Process of the Internal Combustion Engine, Graz, 24/25 Sep 2015.
18. Lestz, S.S., Meyer, W.E., and Colony, C.M., “Emissions from a Direct-Cylinder Water-Injected Spark-Ignition Engine,” SAE Technical Paper 720113, 1972, doi:10.4271/720113.
19. Heinrich, C., Dörksen, H., Tölkes, E., and Esch, A., “Direkte Benzin-Wasser-Einspritzung: CO2-Potentiale und technische Anforderungen,” 10. Tagung Diesel- und Benzindirekteinspritzung 2016, Berlin, 2017.
20. Rottengruber, H., Wagner, T., Beyrau, F., Dragomirov, P.et al., “Sprayvermessung einer Benzin-Wasser-Emulsion,” 10. Tagung Diesel- und Benzindirekteinspritzung 2016, Berlin, 2017.
21. Cavina, N., Rojo, N., Businaro, A., Brusa, A. et al., "Investigation of Water Injection Effects on Combustion Characteristics of a GDI TC Engine," SAE Int. J. Engines 10(4):2017, doi:10.4271/2017-24-0052.
22. Shahlari, A. and Ghandhi, J., "A Comparison of Engine Knock Metrics," SAE Technical Paper 2012-32-0007, 2012, https://doi.org/10.4271/2012-32-0007.
23. Brunt, M., Rai, H., and Emtage, A., "The Calculation of Heat Release Energy from Engine Cylinder Pressure Data," SAE Technical Paper 981052, 1998, https://doi.org/10.4271/981052.
24. Ranuzzi, F., Cavina, N., Scocozza, G., Brusa, A. et al., “Experimental Validation of a Model-Based Water Injection Combustion Control System for On-Board Application,” SAE Technical Paper 2019-24-0015, 2019, doi:10.4271/2019-24-0015
25. Zembi, J., Battistoni, M., Cavina, N., Ranuzzi, F., De cesare, M., “CFD Analysis of PortWater Injection in a GDI Engine under Incipient Knock Conditions”, Energies 2019, 12, 3409; doi:10.3390/en12183409
26. Cooper J., Comparison between Mapping MBT versus 50% mass fraction burn MBT, Ford Motor Co. Report, November, 1997.
27. Ranuzzi, F., Cavina, N., Brusa, A., De Cesare, M. et al., “Development and Software in the Loop Validation of a Model-Based Water Injection Combustion Controller for a GDI TC Engine,” SAE Technical Paper 2019-01-0114, 2019, doi:10.4271/2019-01-1174
28. Cavina, N., Caramia, G., Patassa, S., and Caggiano, M., "Predictive Energy Management Strategies for Hybrid Electric Vehicles: Fuel Economy Improvement and Battery Capacity Sensitivity Analysis," SAE Technical Paper 2018-01-0998, 2018, https://doi.org/10.4271/2018-01-0998.
29. Businaro, A., Cavina, N., Corti, E., Mancini, G., Moro, D., Ponti, F., Ravaglioli, V., “Accelerometer Based Methodology for Combustion Parameters Estimation”, Energy Procedia, Volume 81, December 2015, Pages 950-959, https://doi.org/10.1016/j.egypro.2015.12.15

Abbreviations

CC Cycle-to-Cycle

CCV Cycle to-Cycle Variability

CL Closed Loop

drPID Correction provided by knock Close Loop of r value.

dSAPID Correction provided by r/SA management of SA value.

dSAPIDknock Correction provided by knock Closed Loop of SA value.

dSAPIDmfb Correction provided by MFB50 Closed Loop of SA value.

MAPO Maximum Amplitude of Pressure Oscillations

MAPO98 98th MAPO percentile

MAPO98 th 98th MAPO percentile threshold

MBT Maximum Brake Torque

MFB50 Angle corresponding to 50% of Mass Fraction Burned

MFB50TPC Total Percentage Correction that derives from MFB50 error

nKLSA near Knock Limited Spark Advance

NL Net Load

OL Open Loop

PI Proportional Integral Controller

r Water-Fuel Ratio

RMSE Root Mean Squared Error

RT Real Time

SA Spark Advance

SiL Software in the Loop

TPC Total Percentage Correction

WI Water Injection

WICC Water Injection based Combustion Control